# THERMAL RADIATION BETWEEN AND THROUGH NATURAL HYPERBOLIC MATERIALS

by

**Hakan Salihoglu**

**A Dissertation**

*Submitted to the Faculty of Purdue University*

*In Partial Fulfillment of the Requirements for the degree of*

**Doctor of Philosophy**


School of Mechanical Engineering

West Lafayette, Indiana

August 2021

# THE PURDUE UNIVERSITY GRADUATE SCHOOL
# STATEMENT OF COMMITTEE APPROVAL

**Dr. Xianfan Xu, Chair**

School of Mechanical Engineering

**Dr. Jong Hyun Choi**

School of Mechanical Engineering

**Dr. Zubin Jacob**

School of Electrical and Computer Engineering

**Dr. Amy Marconnet**

School of Mechanical Engineering

**Approved by:**

Dr. Nicole L. Key

*To my father, in loving memory*

# ACKNOWLEDGMENTS

I, first, would like to thank my advisor, Prof. Xianfan Xu, for his wonderful guidance and support. I am indebted to him. His expertise in theory and experimental techniques has enabled me to approach research problems with courage and equip me well for tackling with challenging experiments. Also, his insightful feedback has shed light on my hopeless times while conducting research. Provided by him, freedom on selecting research topics has given me space to recognize my enthusiasm and interest on specific research fields. Supervised by a person with great personality, I have considered myself very lucky. I express my gratitude to Prof. Jong Hyun Choi, Prof. Amy Marconnet, and Prof. Zubin Jacob for agreeing to serve on my committee. The courses I have taken from each one of them laid a good foundation for my research.

I have made wonderful friends and met with colleagues who were always supportive and helpful under any circumstance. To name a few of them, I would like to thank to Dr. Luis Traverso, Dr. Woongsik Nam, Dr. Anurup Datta, Shouyuan Huang, Paul Sommers, Dr. Vasudevan Iyer, Dr. Nan Zhou, Dr. Prabhu Kumar and Mauricio Segovia for great discussions and helps in and out of the lab. I also would like to thank Dr. Anurup Datta for teaching ISPI system and Dr. Prabhu Kumar for teaching NSOM system by giving their precious times for me.

My parents and lovely brother and sister are the ones who stood beside me at any step of my life. There is no word to express my gratitude. My beloved wife and precious daughter kept me sane and in touch with real world everyday by showing their love and occupying me out of research. We are also waiting for one more member to join our little family with great joy.

# TABLE OF CONTENTS

# LIST OF TABLES

# LIST OF FIGURES

# ABSTRACT

Understanding of thermal transport in small scales gains more importance with increasing demand in microelectronics and advancing fabrication technologies. In addition, scarce in energy sources adds more pressure with increasing expectations on research in energy conversion devices and renewable energies. In parallel to these, new phenomena observable only in small scales are discovered with the research, bringing more opportunities for engineers to solve real-world problems by applying the discoveries and more questions to answer. Thermal radiation as a thermal transport phenomenon is the epicenter of this research. Recent developments such as near-field radiative heat transfer exceeding blackbody radiation or control of radiative cooling via biasing grows the attraction on thermal radiation because these examples challenge our long-lasting understanding of nature. Exploring nature further in the small scale may help us meet the expectations mentioned above.

In this thesis work, first, we carry out analyses on radiative heat transfer of natural hyperbolic material, calcite, and compare to that of a polar material SiC. Our study reveals that the high-$\kappa$ modes within the hyperbolic bands are responsible for the substantial enhancement in near field radiation. Comparison of calcite with SiC illustrates the significance of the high-$\kappa$ modes in calcite vs. surface polariton modes in SiC in their contributions to near-field radiation enhancement, for temperature differences ranging from 1 K to 400 K. We also noticed that the contributions of high-$\kappa$ modes in calcite to near-field radiation is comparable to that of surface polaritons in SiC. The results of these analyses will be helpful in the search of hyperbolic materials that can enhance near field radiative transfer.

Second, we demonstrate an experimental technique to measure near-field radiative heat transfer between two parallel plates at gap distances ranging from a few nanometers to far-field. A differential measurement circuit based on resistive thermometry to measure the defined temperatures are explained. To predict the defined temperatures, a computational method is utilized. We also detail an alignment technique that consists of a coarse and fine alignment in the relevant gap regions. This technique presents a method with high precision for gap measurement, dynamic gap control, and reliable sensitivity for extreme near-field measurements. Finally, we

report experimental results that shows 18,000 times enhancement in radiative heat transfer between two parallel plates.

Third, we analyze near-field radiative transfer due to hyperbolic phonon polaritons, driven by temperature gradient inside the bulk materials. We develop a mesoscale many-body scattering approach to account for the role of hyperbolic phonon polaritons in radiative transfer in the bulk and across a vacuum gap. Our study points out the equivalency between the bulk-generated mode and the surface mode in the absence of a temperature gradient in the material, and hence provide a unified framework for near-field radiative transfer by hyperbolic phonon polaritons. The results also elucidate contributions of the bulk-generated mode and the bulk temperature profile in the enhanced near-field radiative transfer.

Forth, we study radiative heat transfer in hyperbolic material, hyperbolic boron nitride (hBN), and show a major contribution to energy transport arising from phonon polaritons supported in Reststrahlen bands. This contribution increases spectral radiative transfer by six orders of magnitude inside Reststrahlen bands compared to that outside Reststrahlen bands. The equivalent radiative thermal conductivity increases with temperature increase, and the radiative thermal conductivity can be of the same order of the phonon thermal conductivity. Experimental measurements are discussed. We showed the radiative contribution can account for as much as 27 % of the total thermal transport at 600 K. Hence, in hBN the radiative thermal transport can be comparable to thermal conduction by phonons. We also demonstrate contribution of polaritons to thermal transport in $MoO_3$. To calculate radiative heat transfer in three principal coordinates separately, we modify and apply the derived many-body model. Our analysis shows that radiative thermal conductivity in both in- and out-of-plane directions increases with temperature and contribution to energy transport by polaritons exceeds that by phonons.

Fifth, we build an experimental setup to examine near-field properties of materials using an external thermal source. The nanospectroscopy setup combines near-field microscopy technique, near-field scanning optical microscopy (NSOM), and Fourier-transform infrared (FTIR) spectroscopy. We further explain challenges in building a nanospectroscopy setup using a weak

thermal source and coupling two techniques. This method enables us to investigate spectral thermal radiation and local dielectric properties in nanoscale.

# 1. INTRODUCTION

Thermal radiation is one of the fundamental physical phenomena. Understanding of thermal radiation in macro scale has been well developed since the end of $19^{th}$ century. Theoretical studies in radiation field for the last half century and developments in manufacturing techniques for the last decades show that thermal radiation requires better understanding at micro and nano scale. Research in this direction gained tremendous momentum, and flourished with various applications such as thermal counterpart of logic gates [1], mid-IR thermal microscopy [2], [3], highly directional thermal antenna [4], and thermophotovoltaic [5]. Near-field radiative heat transfer is a further area finding its place in thermal radiation research. Bringing a hot object to proximity of cold object, or vice versa, drives heat transfer between objects via thermal radiation. Independent experimental studies in the last decade explored near-field heat transfer for separation distances ranging from micro to a few tens of nanometers between two flat plates. However, the separation distance from a few tens of nanometers to contact remains undiscovered due to extreme sensitivity to flatness and parallelism of flat plates as well as challenges in accurate dynamic manipulation of the gap in the corresponding range. Besides, material type plays a key role in radiative heat transfer. Surface phonon polaritons in polar dielectrics and hyperbolic phonon polaritons in hyperbolic materials give rise to near-field radiation, but roles of the polaritons in these materials have not been studied. Apart from radiative heat transfer across vacuum gap, current research efforts on radiative heat transfer in materials under temperature gradient are still in infancy. This thesis is constructed around explaining near-field radiative heat transfer between identical flat plates, made of polar dielectrics and hyperbolic materials, from contact point to micron size separation and investigating radiative heat conductance in hexagonal boron nitride (hBN) and $\alpha$-phase molybdenum trioxide ($\alpha$–$MoO_3$) with temperature gradient. In this section, basic concepts of thermal radiation are introduced, followed by explanation of key components of near-field thermal radiation between parallel plates. This chapter will be concluded with a brief review of hyperbolic phonon polariton in hBN and $\alpha$–$MoO_3$ as hyperbolic material.

## 1.1 Thermal Radiation

Any object with finite temperature emits radiation, the so-called thermal radiation, and the thermal radiation is in an electromagnetic (EM) energy form. The spectral EM energy density associated with electromagnetic wave in vacuum (free space) at position $\boldsymbol{r}$ is expressed by [6]

$$\langle U(\boldsymbol{r},\omega)\rangle = \frac{\varepsilon_o}{2}\langle |E(r,\omega)|^2\rangle + \frac{\mu_o}{2}\langle |H(r,\omega)|^2\rangle \tag{1.1}$$

where $\varepsilon_o$, $\mu_o$, $E$, $H$, and $\omega$ are dielectric permittivity and permeability of vacuum, electric and magnetic fields, and frequency, respectively. Eq. 1.1 is a general expression for any type of EM radiation, e.g., coherent laser illumination, incoherent thermal radiation. Instead, expressing the spectral EM energy density using the Planck radiation form is more insightful because the Planck form explicitly relates temperature with the radiation emitted by the object. As a side note we show in Section 1.2 the Planck form can be derived from Eq. 1.1 using fluctuation dissipation theorem (FDT). According to the Planck radiation, the spectral energy density of thermal radiation is obtained by multiplying the thermal energy of a quantum mode with the density of the modes in the frequency interval [6]

$$\langle U(\omega)\rangle = \rho(\omega)\hbar\omega\left(n(\omega,T) + \frac{1}{2}\right) \tag{1.2}$$

Here, $\rho$ denotes density of states, or modes, (DOS), and $n = \left(e^{\hbar\omega/k_BT} - 1\right)^{-1}$ is probability of finding a state occupied at temperature $T$, where $k_B$ is Boltzmann's constant. 1/2 arises from zero-point energy. The zero-point energy drops in energy transfer calculations [7]. Thus, we neglect it in our calculations. Historically, Eq. 1.2 was only used to define blackbody radiation (far-field radiation). It is also applicable to near-field radiation, which is discussed in Section 1.2. Here in this section, we only discuss far-field thermal radiation. In far-field, $\rho(\omega) = \frac{\omega^2}{\pi^2 c_o^3}$. Then, Eq. 1.2 casts into the form

$$\langle U(\omega)\rangle = \frac{\omega^2}{\pi^2 c_o^3}\frac{\hbar\omega}{e^{\left(\frac{\hbar\omega}{k_BT}\right)} - 1} \tag{1.3}$$

Both counting EM modes in k-space (modern quantum optics) and using fluctuation-dissipation theorem in Eq. 1.1 results in the exact same form in Eq. 1.3 [8]. This form describes the energy density of the blackbody emission.

We know that propagating EM energy in vacuum normal to an area (energy flux) can be found by multiplying energy density with speed of light per solid angle. In mathematical form,

spectral radiative heat flux [W/(m$^2$ rad/s)] emitted to far-field by a surface per solid angle is expressed as follows

$$q(\omega) = \frac{1}{2}\frac{1}{2\pi} c_o \langle U(\omega) \rangle \tag{1.4}$$

where 1/2 accounts for emission to upper or lower half space from the surface, $1/2\pi$ is for per solid angle, and speed of light is propagation speed of EM waves in vacuum. Eq. 1.4 expresses characteristic emission spectrum that contains thermal energy concentrated around a frequency, the so-called characteristic wavelength ($\lambda_c$), depending on T. Increasing temperature shifts $\lambda_c$ to short wavelength range, meaning that peak thermal radiation increases with temperature. $\lambda_c$ obeys Wien's displacement law [9]

$$\lambda_c T = b \tag{1.5}$$

where $b$ is Wien's displacement constant and equals to 2.897x10$^{-3}$ mK. We plot blackbody emission spectrum by inserting Eq. 1.3 into Eq. 1.4. Figure 1.1 illustrates thermal energy enhancing with and the characteristic wavelength shifting with temperature. Operating at 3000 K, Tungsten filament relies on thermal radiation spectrum as a broadband IR light source [10]. Far-field thermal emission spectroscopy makes use of emission spectrum to extract macroscopic dielectric properties of materials [11]. More examples based on this phenomenon can be counted.

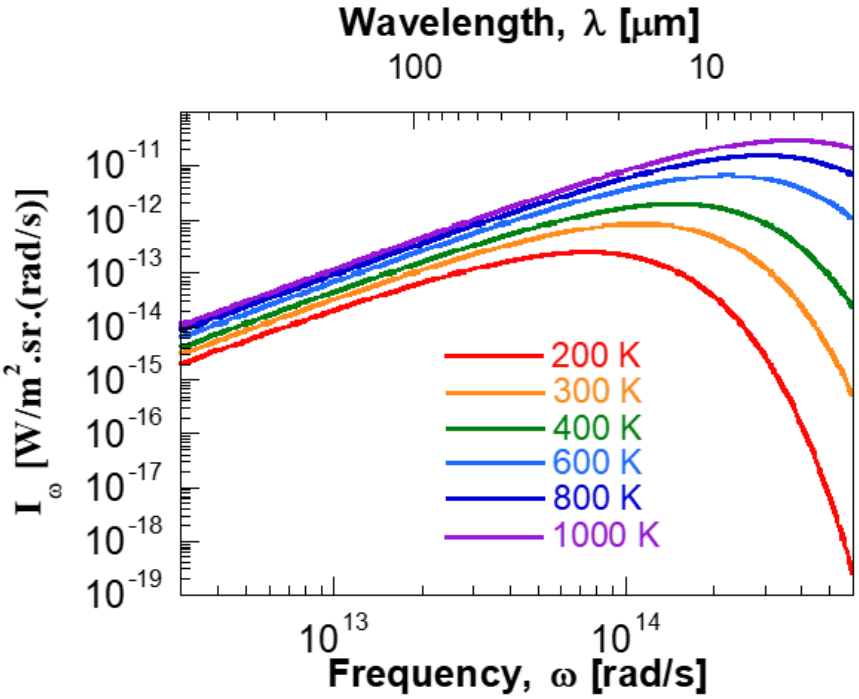


Figure 1.1. Blackbody emission spectrum with respect to temperature

The drawback of sensing and imaging in far-field is that information carried by radiation (light) is limited. Free-space wavevector of light is $k_o = {\omega}/{c_o}$. Any feature on thermal source with a dimension $x < \frac{1}{k_o}$ cannot be resolved using far-field sensing methods because radiation with a wavevector $k > k_o$ fades away in far-field. On the other hand, thermally emitting object contains enhanced energy concentrated in proximity to the object that is called near-field thermal radiation. In the next sections, we will distinguish far- and near-field effect and build the foundation necessary for understanding near-field radiative heat transfer.

## 1.2 Near-Field Thermal Radiation

Near-field is defined as a spatial region close to an emitting object with a distance smaller than characteristic length proportional to $\lambda_c$. An emitted wave with $\lambda < \lambda_c$, $k > k_o$, disappears in far-field. Physically, energy density in near-field increases due to the number of modes supported in the object (medium). In theory, the near-field effect is modeled by extending DOS, $\rho(\omega)$, definition to local density of state (LDOS), $\rho(\boldsymbol{r}, \omega)$ [6], [12]. In this case, Eq. 1.2 is modified, and EM energy density depends on distance from surface [13]. In the next paragraph, we will show deriving the modified Eq. 1.2 by starting from Eq. 1.1.

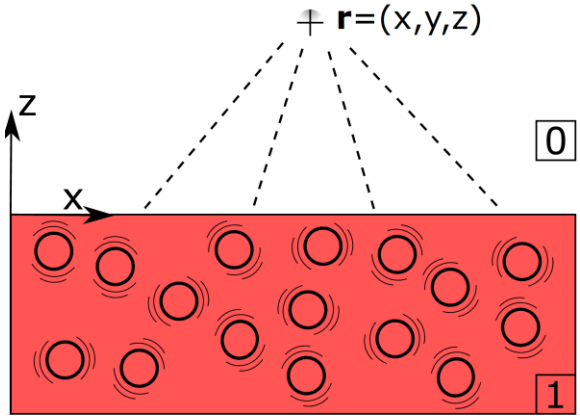


Figure 1.2. Semi-infinite medium (1) occupying a volume of *V* at finite temperature. Fluctuating particles in the medium induce EM field in vacuum (0).

Energy density due to near-field thermal radiation is briefly explained in the following. Consider an object filling lower half space, as shown in Figure 1.2. Thermal energy due to finite

temperature causes particles (electrons, ions, etc.) to fluctuate. These particle fluctuations are modeled as current density $\boldsymbol{j} = (j_x, j_y, j_z)$ in the object as a function of position, $\boldsymbol{r}' = (x', y', z')$, and frequency, $\omega$. Current fluctuations generate EM field, $\boldsymbol{E}$, in vacuum at location, $\boldsymbol{r} = (x, y, z)$ above the interface, $(x, y, 0)$, [6]

$$\boldsymbol{E}(\boldsymbol{r}, \omega) = i\mu_o \omega \int_V \overleftrightarrow{\boldsymbol{G}}(\boldsymbol{r}, \boldsymbol{r}', \omega) \cdot \boldsymbol{j}(\boldsymbol{r}', \omega') d^3\boldsymbol{r}' \tag{1.6}$$

Here, $\overleftrightarrow{\boldsymbol{G}}$ is dyadic Green's function that relates the source fields (current density), $\boldsymbol{j}$, with the generated field, $\boldsymbol{E}$. $\overleftrightarrow{\boldsymbol{G}}$ is governed by Maxwell's Equations [14], [15]. Green's function depends on both material properties and shape of the interface between the materials. To find energy density above the interface, we start the derivation from Eq. 1.1. Then, the similarity between the derived expression and Eq. 1.2 will be constructed. First, spectral correlation functions of the generated fields (both magnetic, $\langle |H(r, \omega)|^2 \rangle$, and electric, $\langle |E(r, \omega)|^2 \rangle$) in Eq. 1.1 need to be evaluated. As an example, the correlation function of electric fields is found by plugging Eq. 1.6 for the fields into the correlation expressions:

$$\begin{aligned} &\left\langle E_\alpha(\boldsymbol{r}, \omega).\, E_\beta^*(\boldsymbol{r}', \omega') \right\rangle \\ &= \mu_o^2 \omega^2 \sum_{m,n} \int d^3\boldsymbol{r}'' d^3\boldsymbol{r}''' \left\langle G_{\alpha m}(\boldsymbol{r}, \boldsymbol{r}'', \omega) G_{\beta n}^*(\boldsymbol{r}', \boldsymbol{r}''', \omega') j_m\,(\boldsymbol{r}'', \omega) j_n^*\,(\boldsymbol{r}''', \omega') \right\rangle \end{aligned} \tag{1.7}$$

Here, $\alpha$ and $\beta$ indicate the direction of the generated electric fields, and $\alpha, \beta$ =x,y,z. Also, *m* and *n* represent the direction of current density, and *m*, *n*=x,y,z. Note that Cartesian coordinate system is reference coordinate. Thus, x, y, and z refer to component of any variable in the corresponding axes, and **x**, **y** and **z** are unit vectors. Since the correlation functions of the electric fields at positions $\boldsymbol{r}$ and $\boldsymbol{r}'$ depends on the correlation of two independent current fluctuation densities at $\boldsymbol{r}''$ and $\boldsymbol{r}'''$, frequency of the correlating fields, $\omega$ and $\omega'$, should be considered separately. In addition, variables with asterisk (*) represent complex conjugate of the variables. Finding the correlation function of the generated fields, $\left\langle E_\alpha(\boldsymbol{r}, \omega).\, E_\beta^*(\boldsymbol{r}', \omega') \right\rangle$, requires the correlation function of the current densities. Derived in various references [16]–[19], fluctuation-dissipation theorem (FDT) expresses the spectral correlation of current densities in a homogeneous, stationary medium in equilibrium with local medium approximation

$$\left\langle j_\alpha(\boldsymbol{r}, \omega)\, j_\beta^*(\boldsymbol{r}', \omega') \right\rangle = 4\pi\omega\left(\hbar\omega n(\omega, T)\right)\varepsilon_o \varepsilon_{\alpha\beta}'' \delta(\boldsymbol{r} - \boldsymbol{r}')\delta(\omega - \omega') \tag{1.8}$$

Here, $\boldsymbol{r}$ and $\boldsymbol{r}'$ are position of the current fluctuations, and $\delta$ shows Dirac-delta function. $\varepsilon''_{\alpha\beta}$ represents imaginary component of $(\alpha,\beta)$ element of dielectric matrix (see Section 1.4). To evaluate Eq. 1.7, we need to express $\overleftrightarrow{\boldsymbol{G}}$, which is given for electric fields over a flat surface by [6]

$$\overleftrightarrow{\boldsymbol{G}}(\boldsymbol{r},\boldsymbol{r}',\omega)=\frac{i}{2}\int\frac{d\kappa}{2\pi}\frac{1}{\gamma_o}[\hat{s}t_s\hat{s}+\hat{p}_1t_p\hat{p}_0]e^{i\boldsymbol{\kappa}.((\boldsymbol{x}-\boldsymbol{x}')+(\boldsymbol{y}-\boldsymbol{y}'))}e^{i\gamma_0 z-i\gamma_1 z'} \tag{1.9}$$

where $\kappa$ and $\gamma_j$ are in-plane (x,y,∥) and out-of-plane (z,⊥) component of wavevector in materials $j$=0, 1, and related with $\gamma_o^2=k_o^2-\kappa^2$ in vacuum ($j$=0), and $\gamma_{p,1}(=\sqrt{\varepsilon_\parallel k_o^2-\varepsilon_\parallel/\varepsilon_\perp\kappa^2}\,)$ and $\gamma_{s,1}(=\sqrt{\varepsilon_\parallel k_o^2-\kappa^2})$ for p- and s- polarized waves inside the medium ($j$=1) with in-plane ($\varepsilon_\parallel$) and out-of-plane ($\varepsilon_\perp$) dielectric components. Planar geometry enables decomposition of wavevector into in- and out-of-plane directions. $\hat{s}$ and $\hat{p}_j$ are polarization vectors of s-, and p-polarized waves in the materials, and $\hat{s}=\boldsymbol{\kappa}\times\hat{\boldsymbol{z}}/|\kappa|$, $\hat{p}_j=-[\frac{\gamma_j\boldsymbol{\kappa}}{|\kappa|}\mp\kappa\hat{\boldsymbol{z}}]/(n_jk_o)$, where $n$ is refractive index. In addition, $t_s$ and $t_p$ represent transmission coefficient of s- and p-polarized waves through interface, and are given by $t_p=\frac{2\sqrt{\varepsilon_\parallel}\gamma_0}{\varepsilon_\parallel\gamma_0+\gamma_{p,1}}$ and $t_s=\frac{2\gamma_0}{\gamma_{s,1}+\gamma_0}$. Plugging Eq. 1.9 and Eq. 1.8 into 1.7 and integrating Eq. 1.7 over volume V enclosing $\boldsymbol{r}''$ and $\boldsymbol{r}''$ after mathematical manipulations yield spectral EM energy density [6], [12]

$$U(\boldsymbol{r},\omega)=\left[\frac{\omega^2}{2\pi^2c_o^3}\sum_{i=s,p}\left(\int_0^{k_o}\frac{\kappa}{k_o}\frac{d\kappa}{\gamma_o}\frac{\left(1-\left|r_{j,1}\right|^2\right)}{2}+\int_{k_o}^{\infty}\frac{4\kappa^3}{k_o^3}\frac{d\kappa}{\gamma_o}\frac{Im(r_{j,1})}{2}e^{-2Im\gamma_o d}\right)\right]\hbar\omega n(\omega,T) \tag{1.10}$$

Note that magnetic energy density equals electric energy density in vacuum, and Eq. 1.10 contains contribution of both fields. $r$ is the Fresnel reflection coefficient at the interface between the material of interest and vacuum, which can be expressed for s- and p-polarized waves as [20]

$$r_{p,j}=\frac{\varepsilon_{\parallel,j}\gamma_o-\gamma_{p,j}}{\varepsilon_{\parallel,j}\gamma_o+\gamma_{p,j}} \tag{1.11}$$

$$r_{s.j}=\frac{\gamma_o-\gamma_{s,j}}{\gamma_o+\gamma_{s,j}} \tag{1.12}$$

Integration over $\kappa$ in Eq. 1.9 is divided into two integrals in Eq. 1.10. Integration from 0 to $k_o$ accounts for propagating waves. The second integral is for evanescent waves whose $\gamma_o$ is purely imaginary. Thus, the near-field contribution fades away exponentially, which is governed by the

$e^{-2Im\gamma_o d}$ term. Thus, if Eq. 1.10 is evaluated for blackbody emission, it simplifies to Eq. 1.3 due to propagating modes in the first integral, yielding 8π. Note that we used $2\pi\kappa\, d\kappa = k_o^2 \cos(\theta)\, d\Omega$, where θ is the angle between the emission direction and the normal of the surface, and performed the integral over a half-space. We draw attention to a similarity between Eq. 1.2 and 1.10. In Eq. 1.10, the terms outside the square bracket on the right-hand side are same with the terms representing mean energy of an oscillator ω, $\hbar\omega n(\omega, T)$, in Eq. 1.2 (we neglect zero-point energy). The expression in the square bracket of Eq. 1.10 corresponds to DOS in Eq. 1.2, and defined as LDOS, $\rho(\boldsymbol{r}, \omega)$, for the near-field regime above the interface. From this similarity, we deduce that LDOS is

$$\rho(\boldsymbol{r}, \omega) = \rho_o(\omega) \sum_{i=s,p} \left( \int_0^{k_o} \frac{\kappa}{k_o} \frac{d\kappa}{\gamma_o} \frac{\left(1 - \left|r_{i,1}\right|^2\right)}{2} + \int_{k_o}^{\infty} \frac{4\kappa^3}{k_o^3} \frac{d\kappa}{\gamma_o} \frac{Im\left(r_{i,1}\right)}{2} e^{-2Im\gamma_o d} \right) \tag{1.13}$$

Here, the first integral in parenthesis shapes material-dependent far-field DOS, whereas the second integral accounts for near-field contribution. As seen, the near-field part contains imaginary component of reflection and exponential terms, both arising from decaying feature of surface-induced phenomena, such as evanescent waves in all material types, hyperbolic phonon-polaritons in hyperbolic materials, surface-phonon polaritons in dielectrics, and surface-plasmon polaritons in metals. This material dependency will be further discussed in next sections.

We will here focus on how we can exploit surface-induced phenomena. As stated above, enhanced density of states in near-field increases local energy density. If one probes near-field of an object using a scattering tip, remote sensing of the field attenuating in far-field is made possible by collecting the scattered radiation with a detector. The output signal contains spectral and spatial information regarding material properties. This is called near-field spectroscopy and microscopy, respectively. Another way to make use of near-field enhancement is near-field radiative heat transfer that happens when a second object is brought to proximity of the first object. In such case, in addition to propagating energy carrying modes, energy transfer between two objects by thermal radiation occurs with tunneling evanescent waves and resonant surface waves. The next section gives brief overview of near-field radiative heat transfer and further introduces fundamental parameters governing the problem.

## 1.3 Near-Field Radiative Heat Transfer

Blackbody radiation has been set as theoretical limit for thermal radiation. However, this is counterproved by recent advancements in measurement techniques that enable to experiment near-field thermal radiation exceeding blackbody radiation by several orders[21]–[27]. This discovery triggers a lot of discussions and research in micro/nanoscale thermal management. Below, we follow the derivation given in literature for general near-field radiative heat transfer expression using FDT and macroscopic Maxwell's equations [6], [12], [28]–[30].

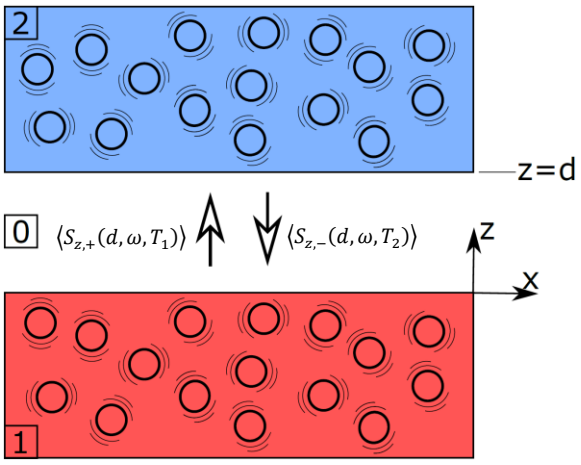


Figure 1.3. Schematic of two media separated by vacuum of thickness $d$. The media are held at constant temperature $T_1$ for medium 1 and $T_2$ for medium 2. Energy flux emanating from medium 1 (2) and flowing in + (-) direction tunnels into medium 2 (1). Net radiative heat transfer, $q_{Net}$, is difference of the energy fluxes.

Consider a thermally active medium occupying lower space at temperature $T_1$, as shown in Figure 1.3. The medium is separated from vacuum by an interface. Thermally induced EM energy fading away from the interface can be transferred to another medium if the second medium is brought in near-field of the first medium. In this case, radiative heat exchange is calculated by difference of energy fluxes emitted separately from two objects. That is,

$$q_{Net}(\omega) = \langle S_{z,Net}(d,\omega,T)\rangle = \langle S_{z,+}(d,\omega,T_1)\rangle - \langle S_{z,-}(d,\omega,T_2)\rangle \quad (1.14)$$

Here, $\langle S_{z,Net}(d,\omega)\rangle$ is ensemble average of net Poynting vector (energy flux) in z-direction. It depends on separation gap, $d$, between two objects. $S_{z,+}$ and $S_{z,-}$ represent energy flux carrying heat upward (+) from medium 1 and downward (-) from medium 2. Poynting vector in vacuum is given by:

$$\langle S_z(d,\omega)\rangle = Re\left[\left\langle E_x(d,t).\ H_y^*(d,t)\right\rangle - \left\langle E_y(d,t).\ H_x^*(d,t)\right\rangle\right] \tag{1.15}$$

Derivation of general form of radiative heat transfer between two flat plates is similar to derivation of the near-field EM energy density given in Eq. 1.10, and follows these steps: Integral form of Maxwell's equations for electric field in Eq. 1.6 and magnetic field, given in [6], are inserted into the cross correlation of EM fields in Eq. 1.15. The resultant equation consists of the correlation function of the current fluctuations and dyadic Green's functions. The current correlations and the Green's functions are already given in Eq. 1.8 and 1.9 in the derivation of the energy density in Section 1.2. Evaluation of all intermittent steps leads us to the general form of radiative heat transfer [31]–[33]:

$$\begin{aligned} q_{Tot}(d) = \int_0^\infty \frac{d\omega}{2\pi}\hbar\omega[n(\omega,T_2)-n(\omega,T_1)] \\ \times \sum_{i=s,p}\left[\int_0^{k_o}\frac{d\kappa}{2\pi}\kappa \times \mathcal{T}_i^{prop}(\omega,d,T_1,T_2)\right. \\ \left. + \int_{k_o}^\infty \frac{d\kappa}{2\pi}\kappa \times \mathcal{T}_i^{evan}(\omega,d,T_1,T_2)\right] \end{aligned} \tag{1.16}$$

This Landauer-type formalism is derived based on surface treatment discussed above, and includes transmission functions of propagating, $\mathcal{T}_i^{prop}$, and evanescent, $\mathcal{T}_i^{evan}$, waves between two surfaces, respectively. Transmission functions account for transferred fraction of total energy emitted by a mode from source medium, and are given as:

$$\mathcal{T}_i^{prop}(\omega,d,T_1,T_2) = \frac{\left(1-\left|r_{i,1}(T_1)\right|^2\right)\left(1-\left|r_{i,2}(T_2)\right|^2\right)}{\left|1-r_{i,1}(T_1)r_{i,2}(T_2)e^{2i\gamma_o d}\right|^2} \tag{1.17}$$

$$\mathcal{T}_i^{evan}(\omega,d,T_1,T_2) = \frac{4Im\left(r_{i,1}(T_1)\right)Im\left(r_{i,2}(T_2)\right)e^{-2Im(\gamma_o)d}}{\left|1-r_{i,1}(T_1)r_{i,2}(T_2)e^{-2Im(\gamma_o)d}\right|^2} \tag{1.18}$$

The numerator of Eq. 1.17 accounts for the portion of transmitted radiative energy by propagating waves through the material interface, and the denominator represents multiple reflections between material interfaces across vacuum gap. In Eq. 1.18, $Im(r_i)$ in the numerator can be interpreted as near-field emission [30] or a quantity proportional to local density of states (LDOS) [29]. Eq. 1.16 considers contribution of all modes, $\kappa$, carrying energy of $\hbar\omega$. Implicit in transmission functions, dielectric properties are used to define the condition of contributing waves such as propagating, evanescent, SPhP, SPP or hyperbolic phonon-polaritons. Detailed information regarding dielectric properties is insightful to grasp the main mechanisms enhancing thermal radiation from materials in near-field. In what follows, we explain how to classify

materials based on their dielectric properties. Furthermore, the conditions of phenomena giving rise to near-field radiation in polar dielectrics and hyperbolic materials will be detailed.

## 1.4 Role of Material Type in Near-Field Radiation

### 1.4.1 Classification of materials based on dielectric properties

Dielectric permittivity is simply the response of material to external EM field. It depends on crystal structure of the material and is described by a 3 × 3 matrix:

$$\bar{\bar{\varepsilon}} = \begin{bmatrix} \varepsilon_{xx} & \varepsilon_{xy} & \varepsilon_{xz} \\ \varepsilon_{yx} & \varepsilon_{yy} & \varepsilon_{yz} \\ \varepsilon_{zx} & \varepsilon_{zy} & \varepsilon_{zz} \end{bmatrix} \tag{1.19}$$

Subscripts represent direction of dielectric response. If crystal structure of the material is symmetric, dielectric matrix can be expressed in diagonal form (off-diagonal terms are zero) based on orientation of coordinate axes. The coordinate axes leading to a diagonal permittivity are called principal axes. When $\varepsilon_{xx} \neq \varepsilon_{yy} \neq \varepsilon_{zz}$, the material is called biaxial. In case $\varepsilon_{xx} = \varepsilon_{yy} \neq \varepsilon_{zz}$, we deal with uniaxial material. Lastly, $\varepsilon_{xx} = \varepsilon_{yy} = \varepsilon_{zz}$ represents isotropic material. These materials are subject of this thesis. We will simplify notation of dielectric permittivity terms as $\varepsilon_{xx} = \varepsilon_{yy} = \varepsilon_{\parallel}$ (in-plane) due to symmetry in x- and y- axes, and $\varepsilon_{zz} = \varepsilon_{\perp}$ (out-of-plane) for uniaxial material. Dielectric permittivity of isotropic material is $\varepsilon_{xx} = \varepsilon_{yy} = \varepsilon_{zz} = \varepsilon$. In this thesis, we only consider materials with principal axes lying along reference coordinates (cartesian coordinate). All variables derived using dielectric properties are defined with respect to the reference system.

### 1.4.2 Polar dielectrics and hyperbolic materials

Dielectric properties of materials are intrinsic properties and have direct impact on thermal radiation. First, they define conditions of wave propagations in the material. Supported under certain conditions, propagating waves in hyperbolic materials enhance EM interactions inside the material. Second, excitation of resonant waves at interfaces is only possible for certain materials with specific dielectric properties. Conventionally accepted theory states, for SPP, ε should be <= −1, and for SPhP, ε should be ~ −1. In addition, dielectric properties depend on temperature. As two objects at low temperatures exchange radiative heat with near-field enhancement, the ratio of near-field enhancement to far-field at higher temperatures may be lower due to

detrimental effect of temperature on dielectric properties. All these examples indicate that the choice of material type greatly influences thermal radiation. Thus, the next section is devoted to discussion of polar dielectrics and hyperbolic materials, and their significance in thermal radiation applications.

One class of (natural) material that has been investigated extensively for near-field radiative transfer is polar dielectric materials, where the governing mechanism is the coupling of surface phonon polaritons (SPhP) excited by photons [34]–[37]. Being a surface phenomenon, these polaritons propagate along interface. In contrast to hyperbolic materials with directional dependency, these polar materials are usually isotropic ($\varepsilon_{xx} = \varepsilon_{yy} = \varepsilon_{zz} = \varepsilon$). Along the polar dielectric surface, surface waves originate from negative dielectric permittivity in the Reststrahlen band where $\varepsilon \leq 0$, but fades away in the direction perpendicular to the interface, and hence needs to be coupled to another nearby surface for heat extraction [38]. SPhP resonance also leads to quasi-monochromatic thermal emission by means of structured surfaces [39]. Furthermore, studies showed that grating structures on the interface with spatial coherence enable directional thermal radiation [34]. Due to SPhP and low losses compared to metals, polar dielectrics are also preferred in building hybrid hyperbolic materials [40].

In this thesis, SiC and $SiO_2$ are studied as polar dielectric materials in near-field thermal radiation. Excitation frequency of SPhP at SiC ($SiO_2$) -vacuum interface corresponds to ~$1.78 \times 10^{14}$ (~$2.18 \times 10^{14}$ and ~$9.27 \times 10^{13}$) rad/s within the Reststrahlen band(s) of SiC ($SiO_2$). SPhPs are transverse surface waves propagating along the interface with large wavevectors that contribute to the enhancement of near-field radiation by increasing the number of coupled resonant modes. Due to transverse optical phonon oscillations in the direction normal to the interface, only p-polarized waves can excite SPhPs.

No model exists to approximate dielectric properties of $SiO_2$ in infrared range at room temperature. Thus, the properties of $SiO_2$ in this thesis are reproduced from Ref. [41] and plotted in Figure 1.4a.

In this thesis, we investigate SiC over a relatively large temperature range, temperature dependent optical properties of SiC are used, and expressed by means of Lorentz oscillator model with fitting parameters given in Table 1.1 [42]:

$$(\omega) = \varepsilon_{\infty}\left(1 + \frac{\omega_{L,i}^2 - \omega_{T,i}^2}{\omega_{T,i}^2 - \omega^2 - i\Gamma\omega}\right) \tag{1.20}$$

Here, $\omega_T(\omega_L)$ is the transverse (longitudinal) phonon frequency and $\Gamma$ accounts for losses. For SiC, one oscillator models dielectric function with good approximation. Considering the fact that variation in $\omega_T$ and $\omega_L$ of SiC is <2% and the change in $\Gamma$ is linear with respect to temperature [42], linear interpolation in resonant frequencies is used in calculations within the temperature range of interest (between 300 K and 700 K). Figures 1.4b and c show temperature-dependent real and imaginary dielectric permittivity of SiC, respectively.

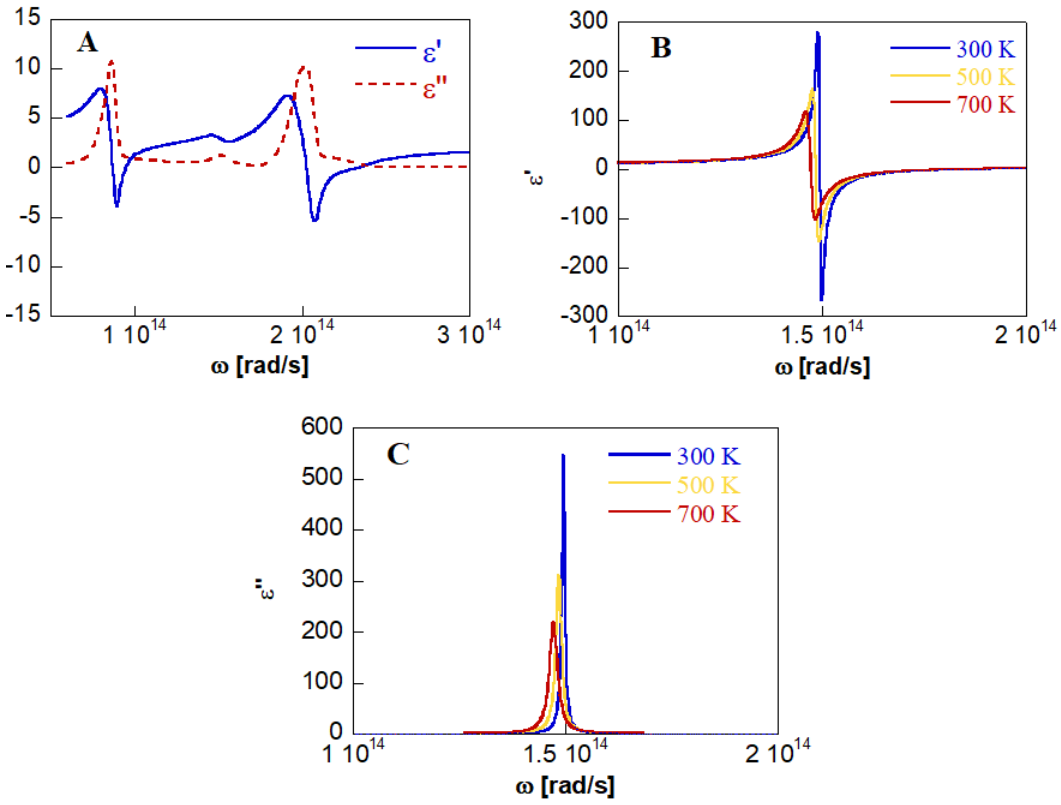


Figure 1.4. Real and imaginary components of dielectric properties for $SiO_2$ at room temperature (a). Real (b) and imaginary (c) component of dielectric properties for SiC at 300 K, 500 K, and 700 K.

Table 1.1. Fitting parameters of SiC at various temperatures

| T [K] | $\omega_T$ [1/cm] | $\omega_L$ [1/cm] | Γ | $\varepsilon_\infty$ |
|---|---|---|---|---|
| 300 | 793 | 969 | 4.76 | |
| 500 | 787.5 | 965 | 8.5 | 6.7 |
| 700 | 781 | 960.5 | 12.2 | |

Another class of the most recent materials studied for near-field heat transfer enhancement is hyperbolic material [43]–[49], where the governing mechanism enabling near-field enhancement is the hyperbolic modes (high-κ modes or hyperbolic phonon polaritons(HPhPs)). Hyperbolic materials are so named because of their topology of isofrequency surface [50], and wavevector range supported inside the hyperbolic materials extends to infinity within hyperbolic bands, hence called high-κ modes. Due to variations in intramolecular or intermolecular bond strengths, the dielectric response of hyperbolic materials is relatively independent with respect to principal axes, and electromagnetic radiation propagating through hyperbolic material is subject to negative and positive dielectric responses simultaneously. The Reststrahlen dispersion relation in one of the principal components of permittivity tensor modifies the isofrequency surface, producing a hyperboloid that supports high-κ modes inside the material within certain frequency bands (Reststrahlen bands). These modes are the main source of near-field enhancement at the interfaces between the hyperbolic material/vacuum/hyperbolic material. Hyperbolic materials were first constructed using hybrid layered structures [51]–[53] or 3D structures [54], [55]. However, natural hyperbolic materials also exist including hBN, calcite, α-$MoO_3$ and $Bi_2Se_3$ [56]. Compared to the fabrication challenges of layered and 3D hybrid material structures, natural hyperbolic materials, especially van der Waals materials, are easier to implement for applications due to advanced fabrication techniques[57]–[59]. Field confinement enables the use of natural hyperbolic materials in sub-diffraction imaging and super-resolution focusing [60]. For radiative heat transfer, hBN [61], α-$MoO_3$ and calcite are promising due to their low losses (ε"~0.1) and thus suitable for long-distance transfer of radiative heat flux [44] within certain frequency bands that support the hyperbolic modes.

In this thesis, calcite, α-$MoO_3$ and hBN are studied as natural hyperbolic materials for thermal radiation. As calcite and hBN are uniaxial, α-$MoO_3$ is of biaxial dielectric properties. They have separate Reststrahlen bands in mid-IR. In these bands, materials possess negative dielectric permittivity in one of principal components.

The uniaxial materials, calcite and hBN, have two Reststrahlen bands, and they are called lower and upper bands. The lower band spans a frequency range $1.64 \times 10^{14} < \omega < 1.69 \times 10^{14}$ ($1.47 \times 10^{14} < \omega < 1.56 \times 10^{14}$) rad/s, and has a Type-I hyperbolic dispersion for calcite (hBN), i.e., a positive in-plane component, $\varepsilon_{\parallel} > 0$, and a negative out-of-plane component, $\varepsilon_{\perp}$<0 (see Figures 1.5 and 1.6). The upper band, $2.64 \times 10^{14} < \omega < 3.08 \times 10^{14}$ ($2.58 \times 10^{14} < \omega < 3.03 \times 10^{14}$) rad/s has a Type-II hyperbolic dispersion with a negative in-plane component and a positive out-of-plane component. Also, calcite has a weak in-plane dielectric response due to molecular vibrations around $\omega \sim 1.33 \times 10^{14}$ rad/s. These dielectric components shape the spectral radiation via allowable/forbidden propagating waves inside the hyperbolic material. From the wavevector expressions $\gamma_p$ $(= \sqrt{\varepsilon_{\parallel}\omega^2/c_o^2 - \varepsilon_{\parallel}/\varepsilon_{\perp}\kappa^2})$ and $\gamma_s (= \sqrt{\varepsilon_{\parallel}\omega^2/c_o^2 - \kappa^2})$, we can see that in the lower Type I band, propagation of s-polarized (also called ordinary) modes with $\kappa < \sqrt{\varepsilon_{\parallel}}\omega/c_o$ and all p-polarized (extraordinary) modes are allowed, while in the upper Type-II band propagation is forbidden for all s-polarized mode, and is allowable only for waves with $\kappa > \sqrt{\varepsilon_{\perp}}\omega/c_o$ for p-polarized modes. These evanescent modes can tunnel through vacuum to a material nearby, which give rise to enhanced near-field radiative transfer between two materials. Accordingly, in the Type I band, near-field enhancement occurs for $\kappa \in [\omega/c_o, \sqrt{\varepsilon_{\parallel}}\omega/c_o]$ for s-polarized waves, and for $\kappa \in [\omega/c_o, \infty]$ for p-polarized waves; and in the Type II band, near-field enhancement occurs for $\kappa \in [\sqrt{\varepsilon_{\parallel}}\omega/c_o, \infty]$ for p-polarized waves only. Since radiation enhancement occurs only in a narrow wavelength band for s-polarized wave, contributions to radiation enhancement are mainly from p-polarized waves.

α-$MoO_3$ has three separate Reststrahlen bands and possesses one negative dielectric component in each band. These bands range over the following frequency regions: RS1 over 545 – 850 $cm^{-1}$ where $\varepsilon_y$<0; RS2 over 822 – 962 $cm^{-1}$ where $\varepsilon_x$<0; RS3 over 957 – 1010 $cm^{-1}$ where

$\varepsilon_z$<0. Dispersion of polaritons in these bands is of more complex form (biquadratic equation) compared to that in uniaxial materials [62]–[64]:

$$k_z^4 + Ak_z^2 + B = 0 \tag{1.21}$$

where coefficients A and B are defined as:

$$A = \frac{1}{\varepsilon_z}\left(\varepsilon_x k_x^2 + \varepsilon_y k_y^2\right) + k_x^2 + k_y^2 - \left(\varepsilon_x + \varepsilon_y\right)k_o^2 \tag{1.22}$$

$$B = \frac{1}{\varepsilon_z}\left(k_x^2 + k_y^2 - \varepsilon_z k_o^2\right)\left[\varepsilon_x k_x^2 + \varepsilon_y k_y^2 - \varepsilon_x \varepsilon_y k_o^2\right] \tag{1.23}$$

Eq. 1.21 has 4 roots and are expressed by:

$$k_z = \pm\sqrt{-\frac{A}{2} \pm \frac{\sqrt{\Delta}}{2}} \tag{1.24}$$

Here, $\Delta(= A^2 - 4B)$ is discriminant. 4 roots ($k_{z,1}$, $k_{z,2}$, $k_{z,3}$, $k_{z,4}$) define 2 up-going (one pair) and 2 down-going (another pair) waves in the system based on the reference system. We will discuss selection of proper solutions in Chapter 5 under Section 5.2.

Dielectric properties of both calcite and hBN can be expressed by Lorentz model with two oscillators in out-of-plane and one oscillator in in-plane directions for calcite using Eq. 1.25 and one oscillator in both in- and out-of-plane directions for hBN using Eq. 1.26:

$$\varepsilon(\omega) = \varepsilon_\infty + \sum_i \frac{A_i}{\omega_i^2 - \omega^2 - i\Gamma_i\omega} \tag{1.25}$$

$$\varepsilon(\omega) = \varepsilon_\infty\left(1 + \frac{\omega_L^2 - \omega_T^2}{\omega_T^2 - \omega^2 - i\Gamma\omega}\right) \tag{1.26}$$

Here, $\omega_i$ is the frequency of the *i*th Lorentz oscillator and $A_i$ is a fitting parameter for calcite. $\omega_T(\omega_L)$ is the transverse (longitudinal) phonon frequency of Lorentz oscillator and Γ accounts for losses. Eq. 1.25 and 1.26 are applicable for both in- and out-of-plane dielectric properties. Also, $\varepsilon_\infty$ is dielectric constant for $\omega \to \infty$. For calcite, fitting parameters for the corresponding directions are given in Table 1.2 at various temperatures. The fitting-parameters at room temperature were obtained from ellipsometry data [65], and those for higher temperatures are derived from dielectric properties reported in Ref [66]. Real and imaginary components of dielectric function at 300 K, 500 K and 700 K are plotted in Figure 1.5. The fitting parameters of

hBN in both directions are given in Table 1.3 and are obtained using Fourier Transform Infrared (FTIR) spectroscopy. Details are given in Chapter 4.

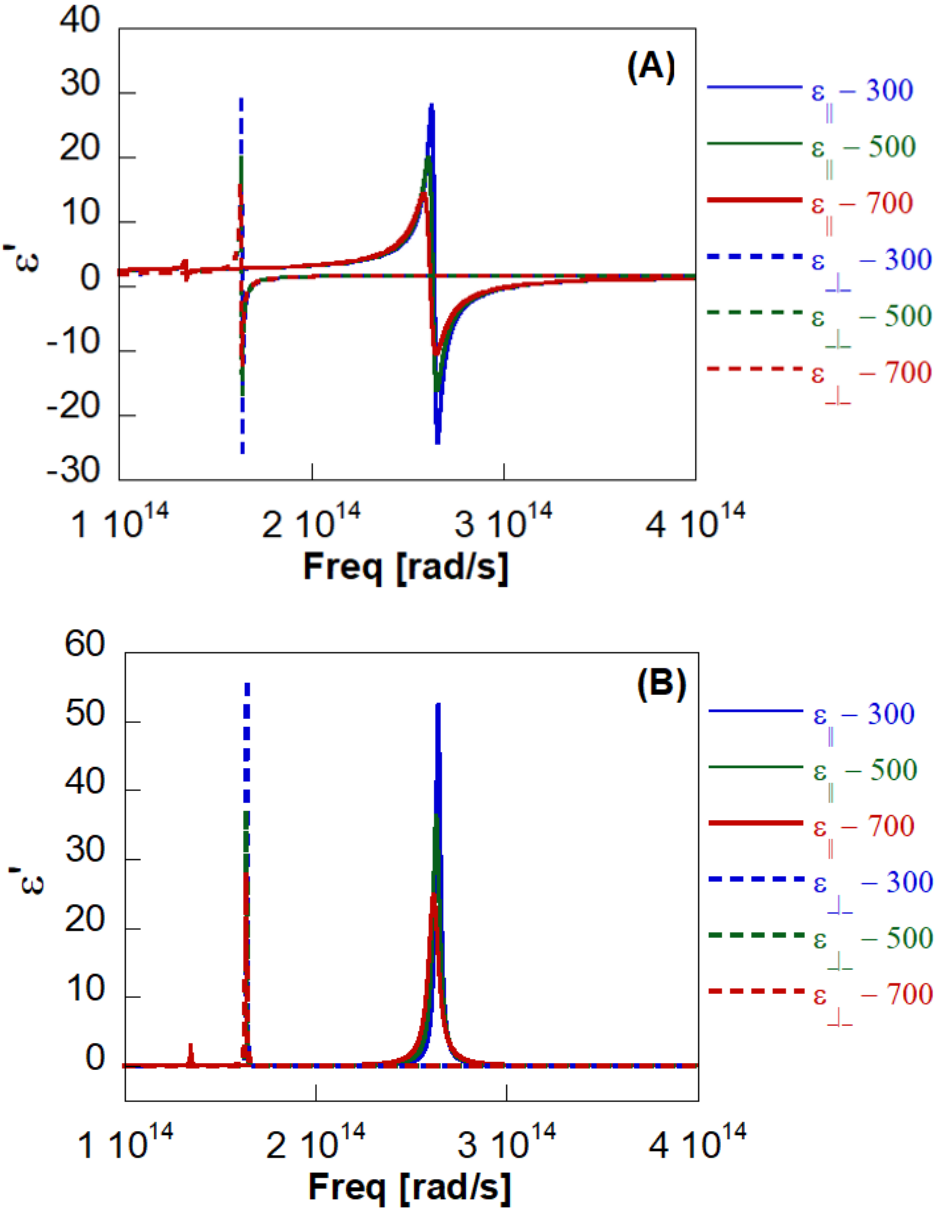


Figure 1.5. a) Real and b) imaginary components of dielectric properties of calcite at 300 K, 500 K and 700 K.

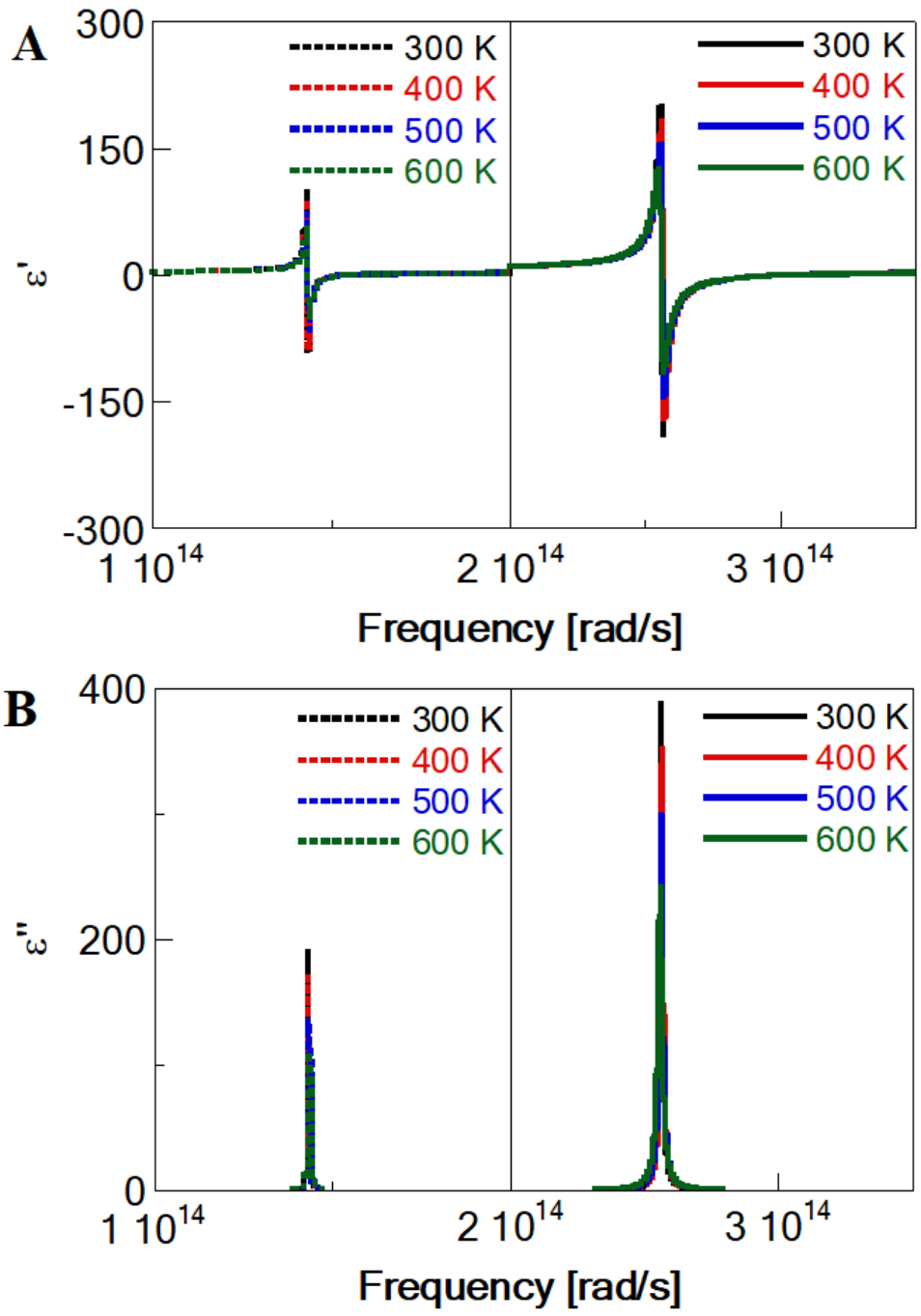


Figure 1.6. A) Real and B) imaginary components of dielectric properties for hBN at 300 K, 400 K, 500 K and 600 K.

Table 1.2. Fitting Parameters of calcite for Lorentz oscillator model.

| | T [K] | $A_i$ [meV]$^2$ | $\boldsymbol{\omega}_i$ [meV] | $\Gamma_i$ | $\varepsilon_\infty$ |
|---|---|---|---|---|---|
| Calcite/ asymmetric | 300 | 18.4 | 173.9 | 2.02 | 1.698 |
| | 500 | | 178.7 | 2.93 | |
| | 700 | | 172.3 | 4.31 | |
| Calcite/ in-plane | 300 | 0.110 | 88.7 | 0.423 | 1.698 |
| | 500 | | | | |
| | 700 | | | | |
| Calcite/ out-of-plane | 300 | 1.272 | 108.0 | 0.207 | 1.647 |
| | 500 | | 107.9 | 0.317 | |
| | 700 | | 107.7 | 0.420 | |

Table 1.3. Fitting Parameters of hBN for Lorentz oscillator model.

| **Principal Coordinates** | T [K] | $\omega_T$ $[m^{-1}] \times 10^{-4}$ | $\omega_L$ $[m^{-1}] \times 10^{-4}$ | $\Gamma$ $[m^{-1}]$ | $\varepsilon_\infty$ |
|---|---|---|---|---|---|
| In-plane, ∥ (x,y) | 300 | 13.64 | 16.14 | 700 | 4.90 |
| | 400 | 13.62 | 16.14 | 763 | |
| | 500 | 13.61 | 16.15 | 910 | |
| | 600 | 13.58 | 16.17 | 1153 | |
| Out-of-plane, ⊥ (z) | 300 | 7.60 | 8.25 | 200 | 2.95 |
| | 400 | 7.605 | 8.247 | 220 | |
| | 500 | 7.61 | 8.245 | 280 | |
| | 600 | 7.61 | 8.233 | 340 | |

For dielectric properties of α-$MoO_3$, a different form of Lorentz model given in Eq. 1.25 is exploited.

$$\varepsilon_\alpha(\omega) = \varepsilon_{\infty,j}\left(\prod_i \frac{\omega_{L,i,j}^2 - \omega^2 - i\Gamma_{i,j}\omega}{\omega_{T,i,j}^2 - \omega^2 - i\Gamma_{i,j}\omega}\right) \tag{1.27}$$

Here, $j(= x, y, z)$ represents principal component of the dielectric property and $i$ stands for $i$th Lorentz oscillator. Π is product notation. In this case, 3 oscillators in x-direction and 1 oscillator in y- and z-directions are sufficient. Fitting parameters for dielectric properties of α-$MoO_3$ is listed in Table 1.4[67]. Figure 1.7a-b shows the properties over the frequency region of interest.

Table 1.4. Fitting Parameters of $MoO_3$ for Lorentz oscillator model at room temperature.

| Axis $j$ | Oscillator Index $i$ | $\omega_{T,i,j}$ [$cm^{-1}$] | $\omega_{L,i,j}$ [$cm^{-1}$] | $\Gamma_{i,j}$ [$cm^{-1}$] | $\varepsilon_{\infty,j}$ |
|---|---|---|---|---|---|
| | 1 | 506.7 | 534.3 | 49.1 | |
| x | 2 | 821.4 | 963.0 | 6 | 5.78 |
| | 3 | 998.7 | 999.2 | 0.35 | |
| y | 1 | 544.6 | 850.1 | 9.5 | 6.07 |
| z | 1 | 956.7 | 1006.9 | 1.5 | 4.47 |

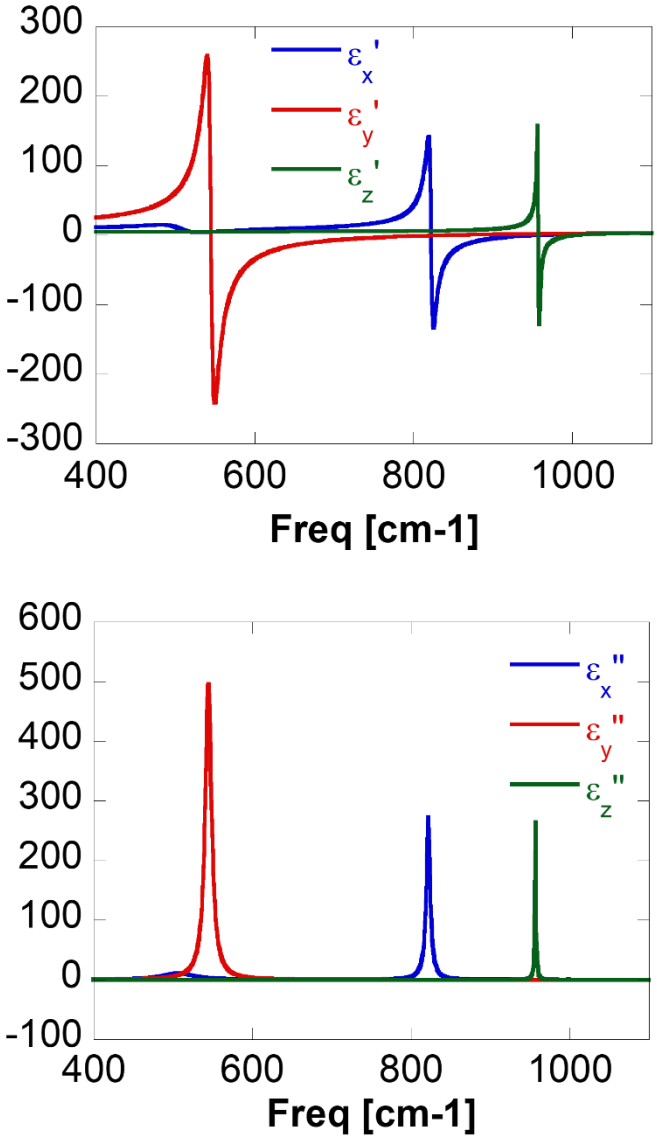


Figure 1.7. A) Real and B) imaginary components of dielectric properties for hBN at 300 K, 400 K, 500 K and 600 K.

## 1.5 Outline

The aim of this study is to investigate heat transfer process due to thermal radiation both between two plates at uniform and nonuniform temperatures and through materials. This chapter briefly touched upon basics on near-field radiative heat transfer and discussed the existence conditions of phenomena enhancing thermal radiation inside and outside the emitting object.

Chapter 2 includes comparison of polar dielectrics and hyperbolic materials in the basis of parameters inducing near-field enhancement.

Chapter 3 describes an experimental technique to measure near-field radiative heat transfer between parallel plates. Applying the technique, we develop temperature and gap measurement systems. Also, performance analysis of the systems will be described. Lastly, our experimental results will be presented.

Chapter 4 contains derivation of theoretical model to account for radiative heat transfer between hyperbolic materials under temperature gradient. Exploiting fluctuation-dissipation theorem and Green's function, a many-body approach is derived to describe contribution of hyperbolic polaritons generated inside the material to energy transport across vacuum separation. We also analyze surface treatment and many-body approach in near-field radiative heat transfer.

Chapter 5 investigates energy transport in hyperbolic materials with thermal radiation. Theoretical calculations of radiative thermal conductivity will be presented, and experimental total thermal conductivity of hBN will be discussed. The unusual thermal conductivity trend in out-of-plane direction over a temperature range from 300 K to 600 K will be answered. This chapter is also expanded for analysis of radiative thermal conductivity in all three principal directions for $\alpha$-$MoO_3$.

Chapter 6 outlines future work and some preliminary results on thermal near-field imaging and spectroscopic method, which exploits near-field scanning optical microscopy (NSOM), and Fourier-Transform Infrared (FTIR) Spectroscopy. Challenges associated with collecting

scattered light from a cantilever using an external thermal source will be discussed and a guideline for future work will be presented.

# 2. NEAR-FIELD RADIATIVE HEAT TRANSFER

This chapter has been partially reproduced from a previous publication*: Salihoglu, H.; Xu, X. Near-field radiative heat transfer enhancement using natural hyperbolic material*. *J. Quant. Spectrosc. Radiat. Transf.* ***2019****, 222-223.*

Theoretical studies of near-field radiation began in the 1950s. Rytov's seminal work employed the fluctuation dissipation theorem (FDT) to link thermal fluctuations in a material with the generated electromagnetic energy, which enables prediction of radiative emission from the material in equilibrium [8]. Bringing a semi-infinite object to the proximity of emitting semi-infinite material was the subject of the study by Polder and Hove [28]. Considering two dispersive and absorptive materials with local temperature approximation, Polder's study was extended by Agarwal for various geometries and concepts , such as local density of states, correlation functions, dispersive and nondispersive dielectric materials in a series of publications [18], [68]–[72]. In 1984, Eckhardt discussed and derived general expressions for a two-body system in global equilibrium ($1^{st}$ kind) and non-equilibrium ($2^{nd}$ kind) conditions using $1^{st}$ and $2^{nd}$ kind FDTs [73]. Given in a cluttered form in the previous studies, near-field radiative heat transfer expression for two-body systems was expressed in a compact form by Pendry [29]. In addition, the limiting heat flux that a single radiation mode can sustain was also investigated. On top of it, Volokitin and Persson investigated various geometrical configurations, e.g. plate-sphere, plate-plate, sphere-sphere, for limiting conditions of local dielectric approximation and retardation effects [74]. In addition to evanescent (tunneling) and propagating wave contribution, resonant surface waves enhances near-field radiation. Dramatic contribution of resonance waves to near-field radiation between two plates was discussed for the first time by Mulet *et. al.* [30]. In another study, Biehs *et. al.* revisited conventional form of near-field expression, and compared with the formalism of transport in mesoscopic physics [31].Over the last decade, the range of theoretical studies on near-field thermal radiation spanned from consideration of spatial coherence of thermal near-fields [75] and phonon polariton in thin films [76]–[78] to heat transfer between spatially dispersive media [79], [80]. More recently, theoretical studies on transition region from radiation to conduction in near-field is of great interest [81]–[87].

In this chapter, we will analyze the origin of near-field enhancement and temperature effect in radiative heat transfer between polar dielectrics, SiC, and hyperbolic material, calcite.

## 2.1 Near-Field Radiative Heat Transfer between Calcite Plates

We investigate the near-field enhancement in radiative heat transfer between hyperbolic materials using calcite. Figure 1.3 depicts the geometry, and dielectric properties of calcite are shown in Figure 1.4b. The enhancement arises from hyperbolic modes that exist over broadband and exhibit nonresonant characteristic. In polar dielectrics, thermal radiation enhances due to resonant surface phonon polaritons, and has been studied extensively. We use polar dielectrics for comparison in our study. To compute radiative heat transfer for both hyperbolic and polar dielectric materials, Eq. 1.16 is used. However, dispersion relation of hyperbolic phonon modes and surface phonon polaritons differs due to different dielectric properties in different directions and this is taken into account in Eq. 1.16 with z component of wavevector as discussed in Section 1.4.2 The comparison will be extended for higher temperature differences between plates in the basis of spectral and total radiative heat transfer characteristics.

### 2.1.1 Transmission coefficients for calcite and comparison with SiC

The transmission function, Eq. 1.18, plays a significant role in near-field radiative transfer, and also conveys insightful information. Here we first discuss parameters determining this transmission function. Figure 2.1 shows the frequency and wavevector dependency of the transmission function, for calcite (a) and SiC (b), for p-polarized waves. Due to the negligible contribution of s-polarized waves to total heat transfer in hyperbolic bands (~1% in Type-I), only p-polarization is shown. X-axis is plotted over $\kappa d$ to demonstrate the evanescent wave tunneling (contribution) of each mode, $\kappa$, governed by $\sim e^{-2\kappa d}$ in Eq. 1.18. As can be seen, calcite has two regimes with large $\kappa d$ in which the transmission function has non-zero values. These high-$\kappa$ modes propagate inside calcite within these regimes, and hyperbolic evanescent waves tunnel through vacuum. It is also seen that these regimes are bound by certain $\kappa d$ values, which is related with penetration depth, proportional to $\sim\kappa^{-1}$. Transmission of evanescent modes with small $\kappa$ values occurs nearly without loss because the penetration depth of these modes is greater

than the separation distance, $d$. Across the same gap, the modes with higher $\kappa$ values decay faster according to $e^{-2Im(\gamma_o)d}$ in the transmission expression.

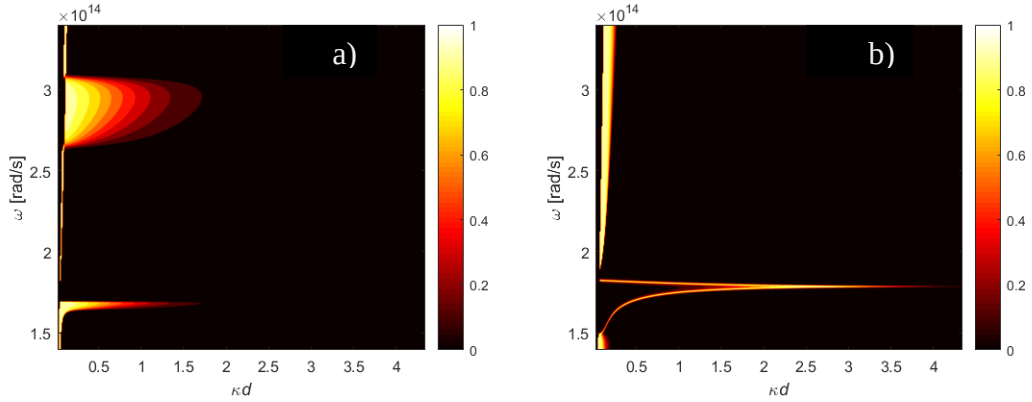


Figure 2.1. Transmission function of p-polarized waves between materials of calcite (a) and SiC (b) with a separation of 100 nm at 300 K. These plots show the contribution of non-propagating modes in vacuum.

Figure 2.1b shows for SPhP there are also high-$\kappa$ modes contributing to the transmission function. Comparison of Figures 2.1a and b indicates there are larger $\kappa$ values for SPhP that contribute to transmission. This difference of the two materials is shown in Figure 2.2, which illustrates the imaginary component of Fresnel reflection coefficients for nonradiative p-polarized waves in Eq. 1.11. Figure 2.2, as a result of Eq. 1.11 and dielectric properties of hyperbolic material and polar material, indicates that $Im\, r_p$ in hyperbolic bands cannot exceed 1 for calcite whereas that of SiC has a value over 20 around the resonance frequency. With smaller $Im\, r_p$ in Eq. 1.18, $\mathcal{T}_p^{evan}$ approaches 0 at relatively smaller $\kappa$ value for calcite compared to SiC. The largest wavevectors that enhance energy transfer in calcite is about ~3 times smaller than that in SiC.

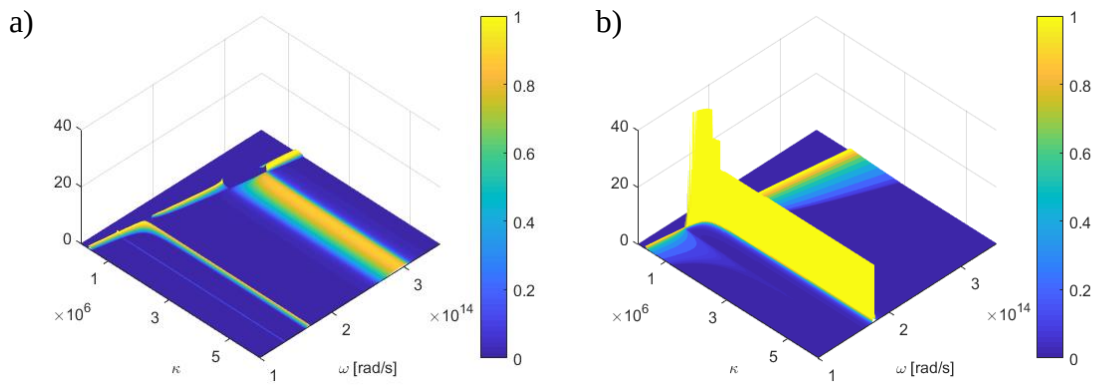


Figure 2.2. Imaginary reflection coefficients of nonradiative p-polarized waves for calcite (a) and SiC (b) in Reststrahlen bands. Color bar is from 0 to 1 (for (b), color bar is saturated at 1).

Figure 2.2 also reveals that for larger $\kappa$ ($\gg \omega/c$, electrostatic limit), the magnitude of $Im\, r_p$ within the Reststrahlen bands is a constant of ~0.9 for calcite and ~10 for SiC. Modes with $\kappa \gg \omega/c$ can transfer energy at the near-field, $d < 100$ nm. This implies that at the near-field, enhancement in near-field radiation at shorter distance is not due to the number of modes. Rather, the contribution for the enhancement solely arises from "accessible" larger $\kappa$ values than that at longer separation as seen in the integral for near-field contribution in Eq. 1.16 along with constant $Im\, r_p$ in Eq. 1.18. Thus, near-field enhancement at extreme near-field is dominated by the contribution of the modes with accessible $\kappa$ values.

### 2.1.2 Evaluation of total radiative heat transfer

To analyze the contribution of high-$\kappa$ modes on radiative transfer in hyperbolic materials, we consider two semi-infinite plates at different temperatures separated by a gap. The temperature of one plate is fixed to 300 K, and the temperature difference (ΔT) between two plates is 1 K, 200 K, and 400 K. We validated the code for SiC by comparing our results to the results in [31] and [30]. Figure 2.3a illustrates the total radiative heat flux ($q_{Tot}$) as a function of the separation distance between the plates at all temperature differences. At large separation distances (close to 10 μm) when propagating waves in vacuum is the main contribution to radiative heat transfer, calcite transfers slightly more energy. This is a consequence of the term $1 - |r_1|^2$ in Eq. 1.17, which represents emissivity of the material. Compared to SiC, calcite has a

real component of dielectric function closer to that of air and a lower dielectric loss, which lead to smaller reflectance and in turn, higher emitted radiation.

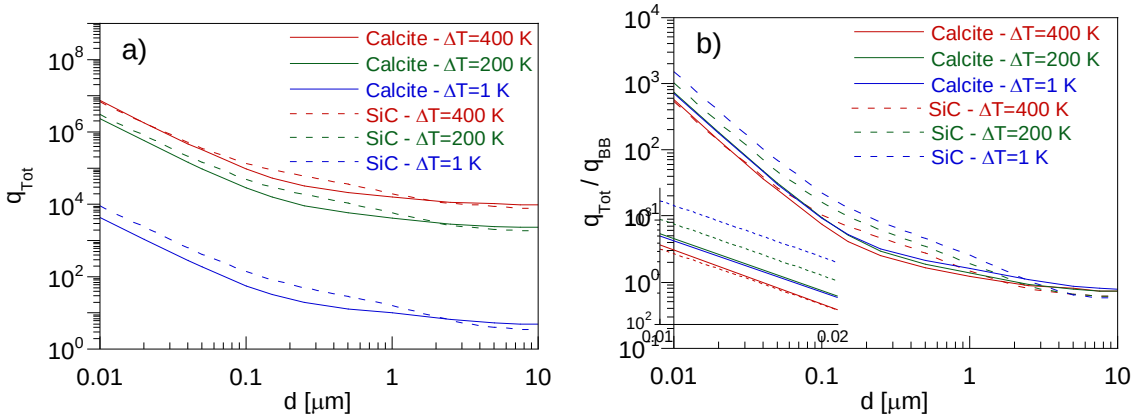


Figure 2.3. a) Total heat flux between two materials, b) Normalized heat transfer to the corresponding blackbody radiation. The inset zooms in extreme near field range for all cases and is also in log-scale.

In the near field regime, $q_{Tot,Calcite}$ increases with the decreasing separation distance due to the tunneling of larger $\kappa$-modes supported in the Type-I and -II bands. As discussed above, $e^{-2\kappa d}$ in Eq. 1.18, which governs the transmission function, decays and approaches 0 when $\kappa d \gg 1$. A shorter separation distance allows larger $\kappa$ to contribute to near-field radiation enhancement. The same reason explains the contribution of SPhP in SiC at shorter distance.

Figure 2.3a demonstrates radiative heat transfer as a function of separation distance at various temperature differences. In general, $q_{Tot,SiC} > q_{Tot,calcite}$ owing to the contribution of the modes with larger $\kappa$ values (Figure 2.1) and larger number of modes than that in calcite at all temperature differences. Figure 2.3b shows radiation normalized to blackbody radiation at the corresponding temperature difference. At 1 K and 200 K temperature differences, the magnitude of normalized radiative heat transfers for calcite ($q_{Nor,Calcite}$), is nearly equal (see inset in Figure 2.3b). This is because on one hand, increasing temperature shifts characteristic wavelength $\lambda_c$ towards the Type-II band. Consequently, more populated states, or high-$\kappa$ modes within the Type-II band enhance near-field radiation. On the other hand, increasing temperature results in broadened Type-II band and weaker dielectric response. This results in smaller $Im\, r_p$, and hence,

smaller contribution of hyperbolic evanescent modes to near-field radiation. Increasing ΔT to 400 K decreases the normalized near-field radiation due to even weaker dielectric response as well as $\lambda_c$ moving out of the Type-II band. For SiC, at 1 K difference, the maximum thermal energy excites states around the resonance frequency, $1.78 \times 10^{14}$ rad/s (10.5 μm), and moves out of this frequency when temperature increases. Thus, the normalized $q_{Nor,SiC}$ reduces as temperature increases. Similar to calcite, the temperature dependent dielectric properties of SiC also contributes to the decrease of $q_{Nor,SiC}$ at larger temperature differences.

Figures 2.3a and 2.3b also show that the increases of both $q_{Tot,SiC}$ and $q_{Tot,Calcite}$ from ΔT = 200 K to ΔT = 400 K are not as high as the increases from 1 K to 200 K and $q_{Tot,Calcite}$ and $q_{Tot,SiC}$ are almost the same at the extreme near field (less than ~ 20 nm). Inspection of $\mathcal{T}_p^{evan}$ for SiC reveals that at this temperature difference, the frequency of maximum $\mathcal{T}_p^{evan}$ is shifted towards a range where SPhPs have $\kappa$ values smaller than maximum $\kappa$ values in dispersion relation of supported polariton modes, which arises from the difference between the resonance frequencies at high temperature. Also, at the resonance frequency for 700 K, wavevectors of polariton modes are nearly half the $\kappa$ values at the resonance frequency for 300 K due to temperature dependent dielectric properties. Therefore, only the polariton modes with about half the $\kappa$ values can strongly couple between two surfaces. In contrast, the high-$\kappa$ modes in calcite within Type-I and -II bands can tunnel through vacuum because each band of the two interfaces for these temperatures still overlaps and supports all the high-$\kappa$ modes. Thus, calcite has about the same near-field radiation enhancement as SiC at the extreme near-field for ΔT = 400 K.

### 2.1.3 Spectral radiative heat transfer

We now further examine the spectral near-field radiative transfer across calcite ($q_{\omega,Calcite}$) and SiC ($q_{\omega,SiC}$) surfaces. Figure 2.4 shows spectral near-field radiative transfer (for all wavevectors) along with near-field contribution of s-polarized evanescent wave ($q_{\omega,s}$) and p-polarized evanescent wave ($q_{\omega,p}$) at a separation distance of 100 nm. A temperature difference ΔT = 1 K is used here. Calcite exhibits three characteristic peaks due to p-polarized waves, and the two of them with higher frequencies are related to the Type-I and Type-II bands. The peak at lower frequencies around $\omega = 1.35 \times 10^{14}$ rad/s is due to a larger value of $Im\, r_p$ (Figure 2.2a),

which originates from a larger imaginary part of the dielectric constant ($\varepsilon_{\parallel}^{"}$~3). The peak of spectral heat transfer in the Type-I band is higher than that in the Type-II because of $\lambda_c$ falling onto the Type-I band at 300K. It is also seen that $q_{\omega,p}$ dips near frequencies right to the Type-I band, because $\varepsilon_{\perp}$~1 at those frequencies, leading to small $\gamma_p (= \sqrt{\varepsilon_{\parallel}\omega^2/c_o^2 - \varepsilon_{\parallel}/\varepsilon_{\perp}\kappa^2})$. Another observation is that $q_{\omega,calcite}$ outside hyperbolic bands (and the peak around $\omega = 1.35 \times 10^{14}$) is higher than the spectral blackbody radiation. Each component of the evanescent waves, $q_{\omega,s}$ and $q_{\omega,p}$, mostly remain below blackbody radiation. However, contributions of radiation due to propagating waves (not shown here) are very close to the spectral blackbody radiation. Therefore, $q_{\omega,calcite}$, is higher than $q_{\omega,BB}$.

Contributions of s-polarized modes to $q_{\omega,calcite}$ are minimal in the Type-I and Type-II regions, as discussed previously. (The peak to the left of the Type II band is due to bulk resonance. [88]) For frequencies beyond the Type-II band, there is a drastic reduction of the contribution of s-polarization evanescent waves since $0 < \varepsilon_{\parallel} < 1$ (see Figure 1.5), meaning that the s-polarized evanescent waves cannot be excited inside the material.

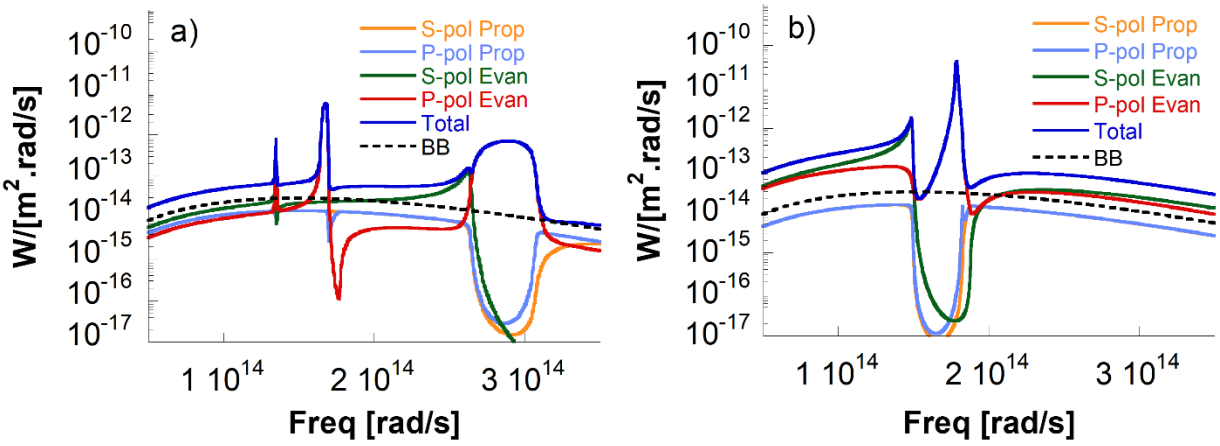


Figure 2.4. Spectral heat transfer between calcites (a) and SiC (b) separated by 100 nm for ΔT = 1 K. For completeness, contribution of s- and p-polarized propagating waves are included. BB: blackbody.

For SiC, only p-polarized waves excite surface polaritons. From Figure 2.4b, it is seen within the Reststrahlen band of SiC, the contribution of s-polarized mode is also minimal. We

noticed that $q_{\omega,s}$ and $q_{\omega,p}$ for SiC exceeds the spectral blackbody radiation outside of the Reststrahlen band. This is due to high $\varepsilon_{SiC}$ outside of the Reststrahlen band, hence SiC supports large evanescent waves, $\omega/c_o < \kappa < \sqrt{\varepsilon}\omega/c_o$, contributing to near-field radiation for both polarizations. Figure 2.4b also shows that $q_{\omega,SiC}$ at resonance frequency is higher than that due to the hyperbolic modes in calcite, because, as discussed above, modes with relatively larger $\kappa$ values in SiC can contribute near-field radiation.

## 2.2 Summary

We carried out analyses on radiative heat transfer of natural hyperbolic material, calcite, and compare to that of a polar material SiC. Our study reveals that, the high- $\kappa$ modes within the hyperbolic bands are responsible for the largely enhanced near field radiation. Comparison of calcite with SiC illustrates the significance of the high-$\kappa$ modes in calcite vs. surface polariton modes in SiC in their contributions to near-field radiation enhancement, for temperature differences ranging from 1 K to 400 K. We also noticed that the contributions of high- $\kappa$ modes in calcite to near-field radiation is comparable to that of surface polaritons in SiC. However, in general, the contribution of high- $\kappa$ modes over the entire spectrum is not as high as the polariton modes in SiC due to contributions of wavevectors with a smaller range. On the other hand, at very near field, the enhancement from calcite is about the same as that from SiC at a large temperature difference of 400 K. This is because the resonance frequencies of SPhPs in SiC for these temperatures shift and polariton couplings take place only at smaller $\kappa$ values. In contrast , despite of the shift with temperature in Type-I and -II bands in calcite, each band at these temperatures still mainly overlaps. The results of these analyses will be helpful in the search of hyperbolic materials that can enhance near field radiative transfer.

# 3. NEAR-FIELD RADIATIVE HEAT TRANSFER EXPERIMENT

This chapter has been partially reproduced from a previous publication*: Salihoglu, H.; Nam., W.; Traverso, L.; Segovia, M.; Venuthurumilli, P.; Liu, W.; Wei, Y.; Li, W.; Xu, X. Near-Field Thermal Radiation between Two Plates with Sub-10 nm Vacuum Separation. Nano Lett.* ***2020****, 20 (8), 6091-6096.*

The first observation of near-field radiation was made at room temperature between two metal plates separated with microscopic distances [21]. At cryogenic temperatures with longer characteristic wavelengths, observation of the near-field enhancement in radiative heat transfer was achieved even for larger separations [89]. Smaller separation gaps waited about more than 3 decades for experimentation due to inability of carrying out sensitive experimental techniques. Conducted between tip-sample, a study [22] measured the near-field thermal radiation between a GaN substrate and a Pt covered tip at distances below 10 nm using Scanning Thermal Microscope(STM). Compared to sphere-plate case, plate-plate configuration was more challenging. The first study in the 2000s observed the near-field radiative heat transfer with a fixed separation between two glass plates using nanoparticles of 1 μm as a separator [23]. In 2009, two independent studies made use of Derjaguin approximation to anticipate near-field radiation at submicron separation distance of two plates with $SiO_2$ [38], and SiC [90]. First plate-plate measurement with dynamic gap control was described in [91]. However, requirement of sensitive gap measurement and flat surfaces constrained this study to separation gaps longer than 2 μm. The near-field enhancement with similar configuration, but at cryogenic temperatures, is repeated by another group in the same year [24]. The near-field enhancement for separations below 1 μm was demonstrated using bulk materials with micron size separation by means of micro structures [25]. Recent experiments were able to detect near-field enhancement for two bulk plates separated below 1 μm down to 150 nm [92]–[94]. Subwavelength measurements were carried out with micro structures [26], [95]. Even though near-field enhancement of sphere-plate configuration is achieved at extreme near field, defined as the distance below 10 nm [96], [97], the current measurements for the plate-plate case is limited to 30 nm due to contamination and experimental technique[27]. Separation below 30 nm for plate-plate configuration requires

new experimental technique with high accuracy of gap reading, dynamic gap control, and smooth and contamination-free surfaces.

This chapter starts with explanation of an experimental technique used to measure radiative heat transfer between parallel plates from contact to far-field. The successive part is devoted to measurement of experiment limits, such as noise equivalent temperature, vibration in gap measurement. Finally, our experimental results for near-field radiative heat transfer are presented.

## 3.1 Experimental Technique to Measure Near-Field Radiative Heat Transfer

To measure near-field radiative heat transfer between two flat plates, we propose an experiment technique explained in this section along with a computational model.

### 3.1.1 Geometrical design of two plates

Two objects (plates), a mask and a substrate, are bulk (macroscopic) and facing each other with flat surfaces. Figure 3.1 shows a schematic of the mask and the substrate. The entire surface of the mask is of a special design with a step-like microscopic island (protrusion). As a result of the design, two essential regions form between the mask and the substrate when the objects are brought in proximity. As the island and its counterpart on the substrate (near-field region) undergo near-field radiation, the rest of the mask and the substrate surfaces (far-field region) remains in far-field. Accordingly, surfaces exposed to near-field are called near-field surfaces (red shaded area), whereas those in far-field region are far-field surfaces (green shaded area). We will refer these surfaces as active surface.

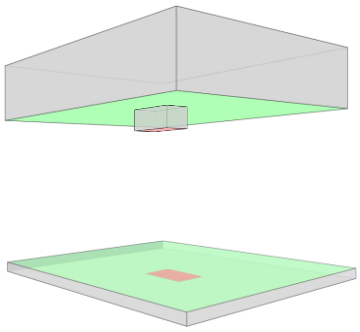

Figure 3.1. Geometry of the mask (top) and the substrate (bottom). The near-field surfaces on the island and the substrate are red colored. The far-field surfaces on both objects are in green.

The second reason of the design is to have a flat surface with minimum height deviation that may not constrain our experimental capability. Any flatness issue leads to misleading near-field thermal radiation measurements.

The third reason of fabricating smaller area is high chance of contamination on large area that disturbs gap measurement, parallelism and pure contact. Smaller area minimizes the chance and avoids stray heat conductance across the near-field surfaces that outweighs radiative heat transfer.

### 3.1.2 Temperature measurement

In our technique, we measure near-field enhancement based on change in temperature at the near-field surface of the substrate with respect to distance between the island and the substrate. The following sections explain details of temperature measurement method and computational temperature estimation.

***Heating objects and temperature difference***

We employ a heater to form a temperature difference between the mask and the substrate. Heater is placed underneath the substrate and heats up the substrate through a copper spreader. Supplied heat drives heat transfer between two objects. Since the experiment is conducted under vacuum, primary heat transfer between the physically separate samples is radiation. Initially, the mask and the substrate are located at far-field. At steady condition, as temperature of the substrate, $T_{H,base}$, is above room temperature, that of the mask, $T_{C,base}$, remains at room temperature. If the samples are brought close that the near-field surfaces are exposed to near-field radiation, temperature of these surfaces alters as a function of separation, $d$, between the near-field surfaces. So, measuring temperature variation at the near-field surface on the mask or the substrate will allow us to observe direct near-field radiation effect in heat transfer form.

Our method considers two locations, matching and sensing areas, on the substrate for temperature measurement. Figure 3.2 illustrates the position of the matching (green) and sensing areas (red). As the matching area occupies a location in far-field region, the sensing area is

exposed to near-field radiation. $T_m$ and $T_s$ are assigned to the matching and sensing areas to represent temperature of the locations. Being at room temperature, both $T_s$ and $T_m$ reaches $T_{H,base}$ with initial heating. When the island on the mask is brought to near-field of the sensing area, $T_s$ drops due to enhanced radiative heat transfer with near-field effect. Meanwhile, $T_m$ does not change. Thus, $\Delta T_m(d) = T_m(d) - T_{H,base} = 0$, whereas $\Delta T_s(d) = T_s(d) - T_{H,base} \neq 0$. We define a relative difference between temperatures of the matching and the sensing areas as a function of gap, $\Delta T_{rel}(d) = T_s(d) - T_m(d)$. Any change in $\Delta T_{rel}$ reflects relative displacement of the mask and the substrate (gap change). If one positions temperature sensors to the sensing and matching areas, measured $\Delta T_{rel}$ directly shows near-field induced heat transfer. The measurement of $\Delta T_{rel}$ using differential temperature measurement scheme is detailed in the next subsection.

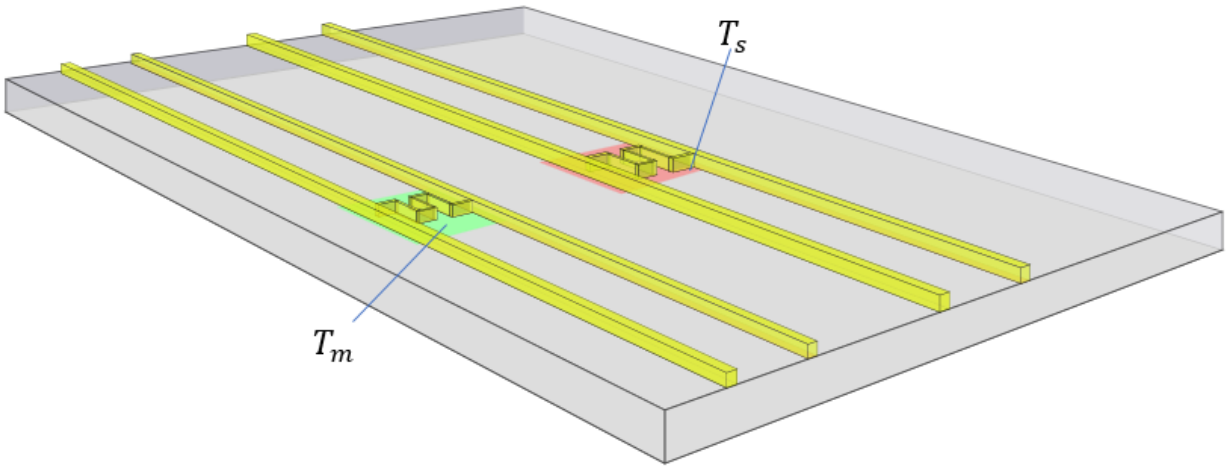


Figure 3.2. Relative position of the sensing (red) and matching (green) areas. The matching and sensing sensors measure temperatures, $T_m$ and $T_s$, of the corresponding areas.

***Temperature measurement circuit***

A differential measurement scheme [98] is implemented for our experiment. The method consists of two resistance-thermometry sensors, matching and sensing sensors. These sensors are positioned to the matching and sensing areas, as shown in Figure 3.2. In principle, resistance of the sensors depends on the temperature of locations the sensor rests. Two sensors are electrically connected in series, and a sensing current is applied to the end terminals of the series connection. Driving sensing current, $I_s$, induces voltage drops, $\nu_m$ and $\nu_s$, across the sensors. In ideal case, a two-level measurement circuit, as shown in Figure 3.3, outputs voltage difference, $\nu_o = G \times (\nu_s -$

$v_m$ ) = $G \times I_s \times (R_s - R_m)$, where $R_m$ and $R_s$ are resistance of the matching and sensing sensors, respectively. If $T_s(d) = T_m(d)$, i.e. the condition after the initial heating of the substrate, $v_o(d >> \lambda_c) = 0$ for the same sensors because $R_m = R_s$. In practice, $R_m \neq R_s$ due to imperfection in fabrication processes. Besides, after the initial heating, any temperature profile along the surface, in turn $T_s(d) \neq T_m(d)$, induces inequal voltage drops, $v_s \neq v_m$, even for the same sensors with $R_m = R_s$. So, $v_{offset}$we modify voltage output to more general expression:

$$v_o = G_1 \times (\Delta v_s(d) - \Delta v_m(d)) + v_{offset} \quad (3.1)$$

Here, $v_{offset}$ accounts for imbalance in voltage values due to the imperfections, and $v_{offset} = G \times (v_{s,base} - v_{m,base} + v_{noise})$, where $v_{s,base}$ and $v_{m,base}$ are voltage readings after the initial reading ($T_s \sim T_m = T_{H,base}$), and $v_{noise}$ is for the noise voltage in the circuit. This general expression also contains variations, $\Delta v_s$ and $\Delta v_m$, in the voltage drops, $v_s$ and $v_m$, arising from the near-field effect, and $\Delta v_s(d) = v_s(d) - v_{s,base}$ and $\Delta v_m(d) = v_m(d) - v_{m,base}$. As an example, Eq. 3.1 reduces to far-field voltage reading $v_{f\text{-}f} = v_o = G \times (v_{s,base} - v_{m,base})$ when $d >> \lambda_c$.

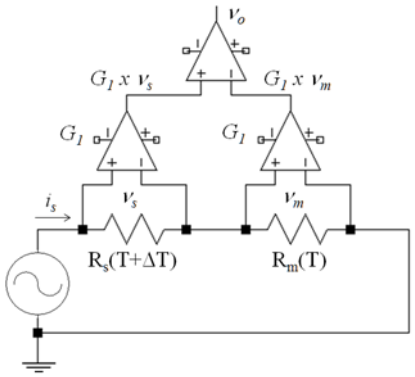


Figure 3.3. Schematic of differential measurement circuit.

The variation in the voltage drops due to the near-field effect is essential part of the temperature measurement. Resistance of the sensors depends on temperature, and its change in the sensing, $\Delta R_s$, and matching, $\Delta R_m$, sensors is given by;

$$\Delta R_s = \alpha_s R_s \Delta T_s \quad (3.2)$$

$$\Delta R_m = \alpha_m R_m \Delta T_m \quad (3.3)$$

where $\alpha_s$ and $\alpha_m$ are temperature coefficient of resistance [$K^{-1}$]. $R_s$ and $R_m$ are absolute resistance value, and, for our consideration, measured at $T_{H,base}$. Now, we can express the variations in Eq.

3.1 in terms of $\Delta R_s$ and $\Delta R_m$ when $I_s \neq 0$. Also, for identical sensors, $R_s \sim R_m = R_o$ and $\alpha_s \sim \alpha_m = \alpha$. Then, Eq. 3.1 becomes

$$v_o = G_1 \times I_s \times \alpha \times R_o \times (\Delta T_s - \Delta T_m) + v_{offset} \tag{3.4}$$

This expression requires TCR values of both sensors, and TCR is intrinsic material property. It is defined as

$$\alpha = \frac{1}{R}\frac{\Delta R}{\Delta T} \tag{3.5}$$

This characterization parameter will be evaluated in Section 3.2.2. Eq. 3.5 indicates that, for a sensor with higher R, resistance change induced by a temperature change is greater than that of the sensor with smaller R. That is, high R is necessity for better sensitivity. On the other hand, high resistance introduces higher Johnson noise proportionally. This aspect will be discussed in Section 3.2.3 as well.

Electrical noise in a temperature measurement may constrain the measurement. To gauge artificial temperature fluctuations arising from the noise in voltage measurements, noise equivalent temperature (NET) is defined as

$$NET = \Delta T_{res} = \frac{v_{noise}}{\alpha I_s R(T)} \tag{3.6}$$

Here, $\Delta T_{res}$ indicates noise equivalent temperature. To measure the near-field induced temperature changes, $\Delta T_{res}$ should be less than $\Delta T_{rel}(d)$. Then, signal-to-noise ratio (SNR) will have high. $v_{noise}$ is already defined in Eq. 3.1 and depends on instrumentation. Even if we can estimate some noise types, such as Johnson noise and shot noise, the practical method of noise determination is to measure it after building the experimental setup.

Next subsection describes computational model to estimate $\Delta T_{rel}$ changing with near-field radiative heat flux as a function of gap. Estimation of the temperature changes helps us determine voltage measurement ranges, signal-to-noise ratio, calculate sensor resistances, and relate temperature variation with near-field radiation, that is, the goal of the experiment. For technical aspect of the measurement technique, the reader is directed to the studies [98]–[100]. Details specific to our experiment, such as applied currents, reference current frequency, are provided in Section 3.2.3.

***Computational method for estimation of temperature variations***

Our computational method makes use of commercially available package program, COMSOL. Heat transfer module provided by the package program has the required features to model the experiment. An important question arises as to how to simulate near-field radiative heat transfer with a commercial program that only has limited capability of solving common radiation problems. To deal with this, radiative heat transfer coefficient, $h_r$, similar to convective heat transfer coefficient, $h_{conv}$, is defined. In general, radiative heat flux between the near-field surfaces, as shown in Figure 3.1, at temperatures $T_H$ and $T_C$ is expressed as follows

$$q'' = q_{NF} = \varepsilon\sigma(T_H^4 - T_C^4) = h_r(T_H - T_C) \tag{3.7}$$

where

$$h_r = \varepsilon\sigma(T_H^2 + T_C^2)(T_H + T_C) \tag{3.8}$$

Here, $\varepsilon$ and $\sigma$ are emissivity, and Stephan Boltzmann's constant, respectively. Conventional radiative heat transfer expression and the corresponding variables in Eq. 3.7 are defined for far-field radiation, in turn, independent of separation gap, $d$. For our purpose, we will expand definition of Eq. 3.7 to estimate near-field radiative heat transfer and, define radiative heat transfer coefficient as a function of separation gap, $h_r(d)$, and effective emissivity, $\varepsilon_{eff}$, in place of $h_r$ and $\varepsilon$, respectively, in Eq. 3.7.

Near-field radiation process removes heat, $q_H''(d)$, from the near-field surface on the substrate, and transfers heat, $q_C''(d)$, into the near-field surface on the mask based on our problem(hot substrate, cold mask) and $q_H''(d) = q_C''(d) = q'' = q_{NF}$.

We can calculate radiative heat transfer coefficient as a function of gap from far-field, $h_r(d>\lambda_c)$ , to near contact point, $h_r(d\rightarrow 0)$ using Eq. 1.16. In the software package, we employ convective heat transfer coefficient, $h_{conv}$, to model near-field radiative heat transfer using $h_r(d) = h_{conv}$. Then, $h_{conv}$ is also known as a function of gap. To find $T_H$ and $T_C$ for a particular distance, we assign an initial $h_{conv}$ to the near-field surfaces and iterate until the condition, $q_H''(d) = q_C''(d)$, is satisfied. Then, the final $h_{conv}$ yields $T_H$, $T_C$, and $q_{NF}$ for the given distance. Repeating this procedure for several separation distances between far-field to near contact allows to estimate

$T_H(d)$, $T_C(d)$ and $q''(d)$ as a function of separation gap. We can also easily extract $\varepsilon_{eff}(d)$ using Eq. 3.8 for the separation distances the model is run for.

We now establish the computational and experimental aspects of the near-field experiment technique. In our experiment, after initial heating, $T_H(d) = T_{H,base}$ and $T_C(d) = T_{C,base}$ at far-field. From far-field to near contact, $T_H(d)$ varies with $\Delta T_H + T_{H,base}$. Then,

$$\Delta T_H(d) = T_H(d) - T_{H,base} \tag{3.9}$$

We know that $T_s(d) = T_H(d)$ because the sensing sensor is located to the near-field surface on the substrate(hot object). From Section 3.1.1, $\Delta T_{rel}(d) = T_s(d) - T_m(d)$. So, $\Delta T_{rel}(d) = T_H(d) - T_m(d)$. We also know that $T_m$ is independent of $d$ due to far-field exposure, and $T_m = T_{H,base}$ with the initial heating. $\Delta T_{rel}(d)$ casts into the form with Eq. 3.9

$$\Delta T_{rel}(d) = T_s(d) - T_m = T_H(d) - T_{H,base} = \Delta T_H(d) \tag{3.10}$$

Eq. 3.10 relates computational near-field radiative heat transfer results to the temperature measurement using differential measurement method. If the initial absolute temperature, $T_{H,base}$, after the heating is known (or measured), one can measure temperature variation induced by manipulation of separation distance in near-field regime.

This leads us to discussion of gap measurement method.

### 3.1.3 Alignment and gap control

Alignment and gap control are crucial parts of our experiment. The mask and substrate are relatively positioned, and their active surfaces face each other. Figure 3.4 shows the active surfaces. Alignment defines adjustment of relative angle between the active surfaces, and bringing the objects in near-field distances. Any tilt between the active surfaces or inaccuracy in alignment skews result of the near-field radiation measurement. Gap control consists of measurement of the relative distance between the active surfaces and maintaining the target gap at which near-field radiation measurement is carried out. Since near-field radiation varies exponentially at nano level, precision should be in subnanometer, and accuracy of measurement system needs to be in the same range as well for extreme near-field measurements. To achieve gap control with such quality, two-step measurement approach is engaged. We call them coarse

alignment, interferometric method, and fine alignment and gap measurement using an Interferometric-Spatial-Phase-Imaging (ISPI) system.

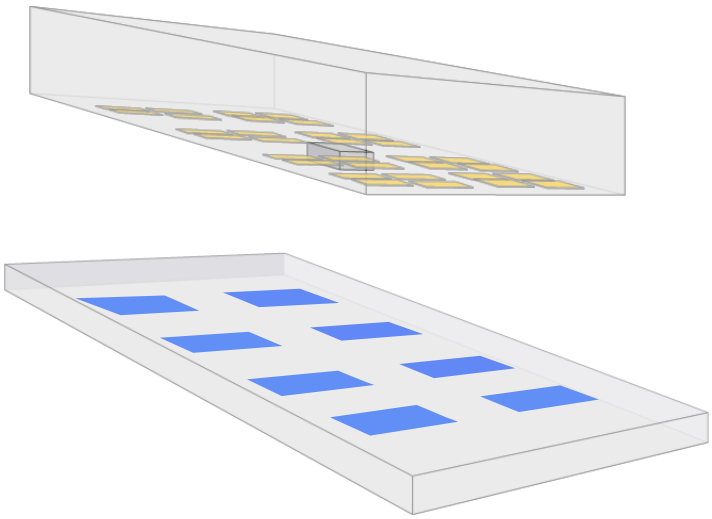

Figure 3.4. Active surfaces on the mask and substrate. As the mask surface contains specialized grating textures, the substrate surface is free of any physical feature special for the alignment. Blue shaded areas correspond to gap reading locations on the substrate.

In the coarse alignment (initial alignment), a He-Ne laser ($\lambda$ = 633 nm) beam shines on both the mask and substrate. If either the mask or the substrate is chosen transparent to $\lambda$, the light passes through it and reaches on a cavity remaining between the active surfaces. Reflected light from the active surfaces is back traced and collected using a CCD camera. Image shows fringes depending on the tilt between the active surfaces. The adjustment of the tilt is achieved by manual 3-point alignment that uses 3 screws with displacement of 100 μm per thread holding the mask stage with a high-precision piezoelectric tilt stage. Actively viewed on a screen, the fringes are adjusted using the screws such that the number of the tilt-induced fringes minimizes. This method achieves a planar alignment in the order of 1 mrad [101], which translates to ~10 μm over 1× 1 $cm^2$. Further tilt-adjustment with the piezo stage of 0.1 mrad resolution is accomplished by nulling the fringes. This ensures a planar parallelism of within 0.1 mrad, e.g. ~10 nm deviation from the complete parallel over 100 × 100 $\mu m^2$. The 3-point alignment also adjusts the relative gap between the active surfaces by lowering the stage hold by the screws. Without deviating much from the set position with the least number of the fringes, the lowering of the mask continues until the relative gap between the active surfaces of the mask and the

substrate is in the measurement range of ISPI system. This range corresponds to ~150 μm. By this, coarse alignment is accomplished.

In the fine alignment, computer controlled ISPI system is exploited. The working principle of the system can be found in literature [102]–[104]. Here, we highlight the points most relevant to our experiment. The system consists of a fiber laser, specialized texture on the mask and ISPI scope. Light beam from the fiber falls with oblique angle on one of the gratings on the mask. Positions of the gratings are seen in Figure 3.4. Period of the grating in one direction (X) is constant (1 μm), seen in Figure 3.5a. This allows back-diffraction of the incident light at a fixed angle, Littrow angle [104]. Rest of the beam diffracts and reflects from the substrate. However, the distance traversed by the diffracted-reflected beams varies due to varying period of the gratings in the transverse direction (Y). Consequently, the diffracted-reflected light beams interfere and form fringes after rediffracting from the mask with Littrow angle to the ISPI scope. Fringes lie along X axis, and the spatial frequency and position of fringes along Y axis depend on the gap. Displacing the mask or the substrate results in propagation of fringe positions in one direction along Y axis. Thus, the fringes from TCG with reverse chirping, as seen in Figure 3.5a, counterpropagate in the meantime. Relative phase of these fringe positions provides information to make use of. The spatial frequency of the fringes from two TCG is same for a gap distance and is not sensitive enough to gap change, causing ambiguity in gap reading. On the other hand, the relative phase within $2\pi$ range, which corresponds to 150 nm for our case due to fiber laser wavelength, allows precise gap measurement without ambiguity. The system can detect the phase changes around 1/1000 of one cycle. Consequently, the sensitivity of the gap reading is 0.15 nm.

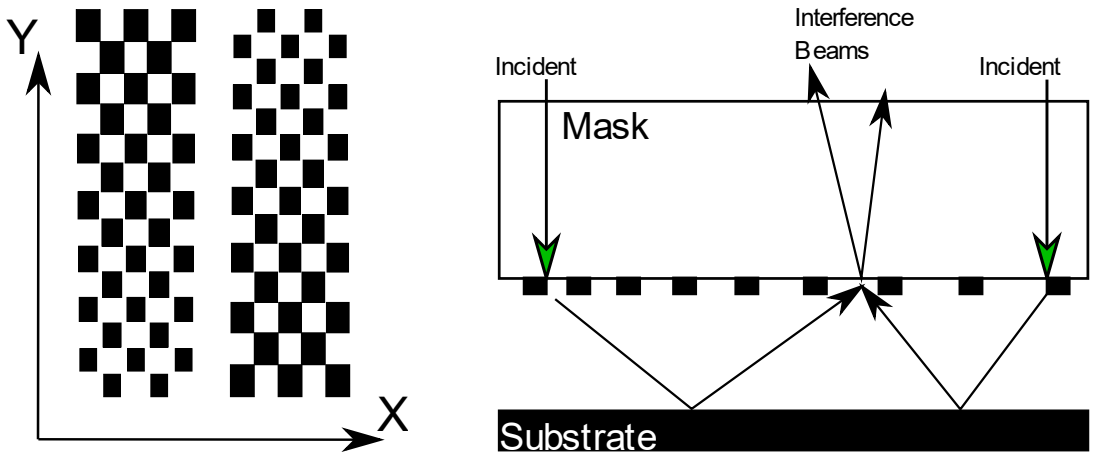


Figure 3.5. (a) Transverse chirped gratings (TCG) in reverse directions. (b) Interfering diffracted-reflected-diffracted beams.

The ISPI system rests on a stage with micro controllers in X-Y axes, and the stage is controlled over a Labview VI. Placed at 8 different locations, the gratings are searched by the Labview VI, and the absolute gap value from 8 different locations at a particular gap distance can be read. This allows us to control tilt of the plates with high precision.

Another important alignment parameter is the relative position of the island and the sensing sensor. Both should be positioned on the same axis vertically. To align both coarsely, a CCD camera with 12x zoom is located such that one can see the relative vertical position exploiting the camera view. Coarse alignment is realized after moving the substrate in X-Y directions in accordance with the view. The ISPI scope collects a reflection image of the island and the sensor. Those reflections can be seen with the Labview VI developed for the gap adjustment, as shown in Figure 3.6. Subsequently, two reflections are overlapped by adjusting X-Y positions of the sensor. In conclusion, one can ensure that the sensing sensor is directly under the tip and near-field radiation effect can be measured.

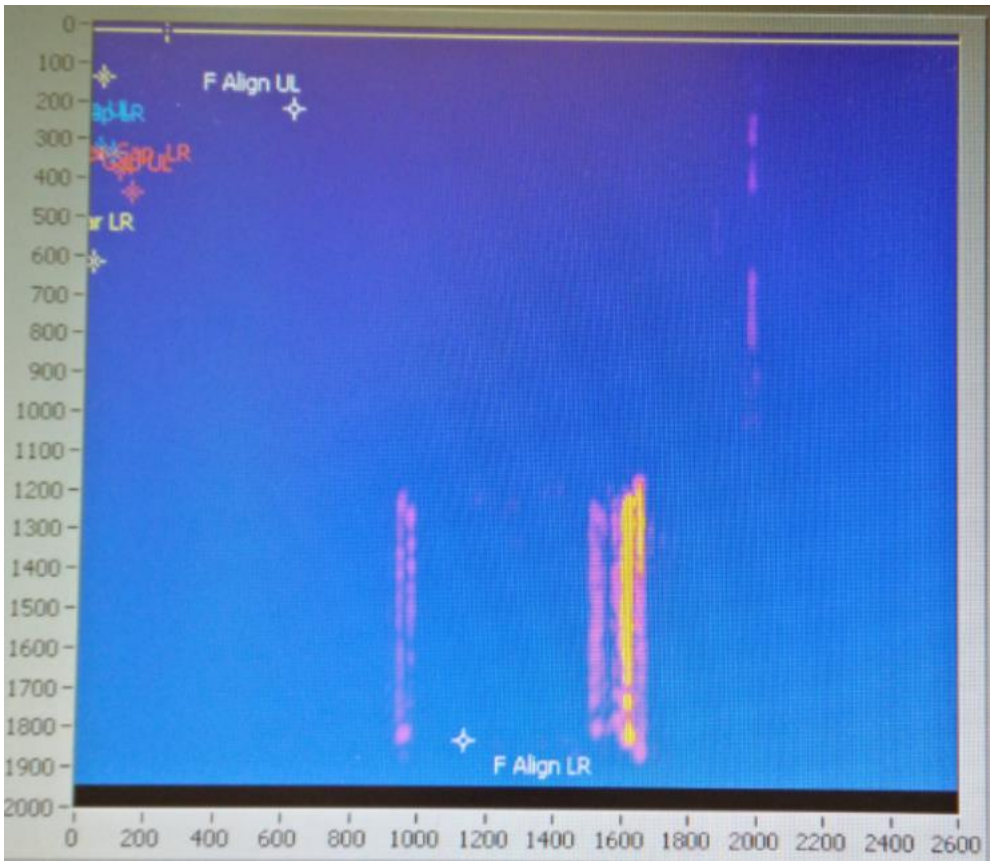


Figure 3.6. Illustration of the relative position of the island(square on the lower half of the image) and the sensing sensor (line on upper half of the image) on Labview VI's screen.

The ISPI system has been exploited for several studies [103]–[106], and we will employ this system to measure the gap distances in our near-field radiative heat transfer experiment.

## 3.2 Near-field Radiative Heat Transfer Experiment

This section is devoted to application of the method explained in Section 3.1 to the near-field radiative heat transfer experiment.

### 3.2.1 Employing computational model for the experimental system

To exploit the method explained in Section 3.1.2, we model our experiment setup consisting of 0.5" × 0.5" × 0.157" quartz and 1" × 1" × 1 mm quartz . The near-field surfaces are 100-μm-by-100-μm square, and the island on the mask is ~10−μm tall. First, we determine the heat flux from the heater that gives the experimental substrate temperature, $T_{H,base}$ (see the next

paragraph). For this simulation, a constant heat flux to the substrate is applied without the presence of the mask. All exposed surfaces of the substrate exchange radiation heat with ambient at $T_{Room}$. We iteratively vary the supplied heat flux until the experimental $T_{H,base}$ is reached. We then run the simulation for the case when the mask is positioned 20 μm away from the substrate surface. Again, the other surfaces facing ambient are in radiative heat exchange with ambient. The surfaces on the mask and the substrate facing each other also exchange heat via far-field radiation. For this far-field heat exchange, we assign a far-field total emissivity values ($\varepsilon = 0.65$) calculated by the ratio of the heat flux using Eq. 1.16 and the blackbody radiation at the corresponding temperatures. Then, we proceed to the second step of simulating near-field radiation at given separation distances. In the step, as a result of the near field radiation, the temperature of the hotter surface, $T_H$, on the substrate decreases and the temperature of the colder surface, $T_C$, on the island on the mask increases. As discussed in Section 3.1.2, additional boundary condition, $q_H = q_C$ where $q_H$ (and $q_C$) is near-field radiative heat flux from (to) the near-field interaction area on the substrate (the mask) is therefore needed which is satisfied through iterative calculations. This calculation then yields $\Delta T_{rel}$ (the sensor temperature difference) at a given separation. This step is repeated for various separations. $\Delta T_{rel}$ results are reported in Figure 3.14a-c for $\Delta T$ = 4.8 K, 7.1 K and 9.8 K, and heat flux values are given in Figure 3.15a.

In the model, thermal conductivity of plates has significant impact on estimated temperature values. Thus, thermal conductivity of the mask, $k_{mask}$, and the substrate, $k_{substrate}$, are measured using time-domain thermal reflectance (TDTR) technique by Mauricio Segovia. The measurements yield a thermal conductivity of 5.0 +0.75/−0.5 $Wm^{-1}K^{-1}$ for the mask, $k_{mask}$, and 1.5 +0.22/−0.15 $Wm^{-1}K^{-1}$ for the substrate, $k_{substrate}$.

It is noteworthy that we considered several $\Delta T$ because we need to anticipate the measurable temperature differences with the sensors designed in the next section. In finding out $\Delta T_{rel}$ and $q$" for the results in Figure 3.14a-c and 3.15a, respectively, our main assumption is that $h_{nfr}$ does not vary with $\Delta T$. This holds true only if $T_{H,base} \sim T_{C,base}$. Therefore, while supplying heat, we need to consider this parameter, and aim the temperature range, $T_{H,base} \sim T_{C,base}$, for the initial heating.

With computational analysis associated with theoretical predictions, we obtained the temperature profiles expected in the near-field radiation experiment. So, we are able to design the sensors in the differential measurement circuit, and determine parameters such as resistance and positions of the sensors, amplitude and frequency of driving current, according to the estimated temperature variations at sensor locations.

### 3.2.2 Temperature sensors

This subsection is devoted to technical consideration of the sensor designs, their locations and characterization to determine TCR of the sensors.

***Location and resistance of the sensors***

For our experiment, we plan to locate the sensing sensor on the near-field surface of the substrate, and it will be embedded in a grooved area that should be as small as possible to better measure the near-field effect with minimum distraction. We choose the grooved area of 30 μm by 40 μm that corresponds to 1/8 of the near-field surface (100 μm x 100 μm). Meanwhile, resistance of the sensing sensor should be necessarily high to obtain the highest resolution and sensitivity. By considering our fabrication constraints, it is decided to build a sensor with 30 nm thickness at least. Paths forming the sensor have 360 nm widths, and the entire sensor fits in the grooved area well. The identical matching sensor is positioned about 2-mm away from the sensing sensor because the computational results suggest that $T_m$ ($d$ = ~20 nm) ~ $T_{m,base}$ for 2-mm-away area. Consequently, the assumption that $T_m = T_{m,base}$ during the entire experiment duration holds true. The sensors are made of platinum due to linear temperature characteristics [107]. The sensors were fabricated by Woongsik Nam, one of our group members. Figure 3.7 shows one of the fabricated sensors under optical microscope. The sensing and matching sensors are designed/fabricated with the same dimensions because we want to obtain identical thermal and electrical characteristics from the sensors. Otherwise, TCRs and voltage drops under same temperature variation differ, meaning that the experimental results skew from ideal conditions. As a result, the measured resistances of the fabricated sensors, using 4-probe method, is $R_s$ = 22.7 kΩ for both sensors.

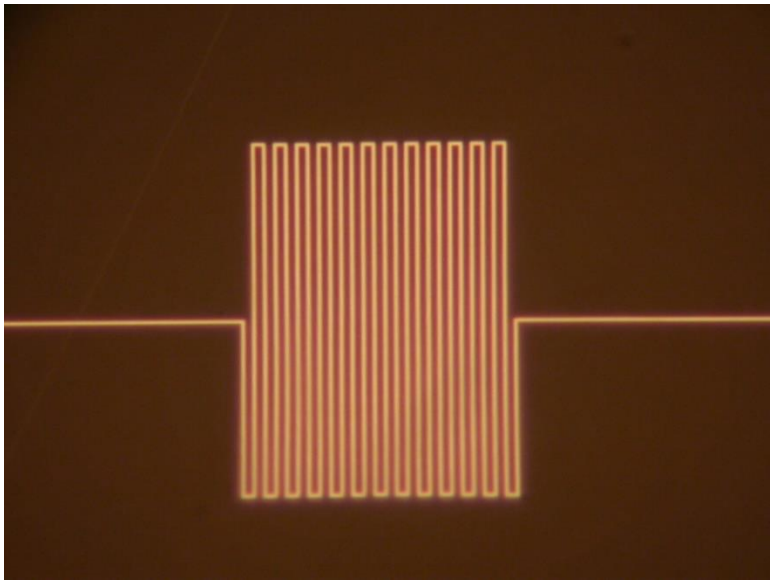

Figure 3.7. Microscope image of one of the sensors over the substrate. There are two sensors with the same size on the substrate. The sensing sensor is vertically aligned beneath the island on the mask to sense the temperature variation due to the near-field effect.

***Characterization of the sensors (TCR)***

Resistance of micro sensors, R, depends on sensor temperature, $T_s$. The measured voltage change across the sensor, $\Delta V$ (= $\alpha \times R_o \times \Delta T_{rel} \times I_s$, where $I_s$ is the current and $R_o$ is resistance at room temperature), can be converted into relative temperature variation, $\Delta T_{rel}$, using Eq. 3.4 and Eq. 3.10 if temperature coefficient of resistance in Eq. 3.6 is known. This temperature coefficient is found by calibrating the sensor. Figure 3.10 illustrates calibration measurements of $\Delta R$ with respect to $\Delta T_{sen}$ using a hot plate ramped from room temperature to 35 K above the room temperature. Since $R_o \sim 22.7$ kΩ, the measured $\alpha$ is $1.94 \times 10^{-3}$ $K^{-1}$.

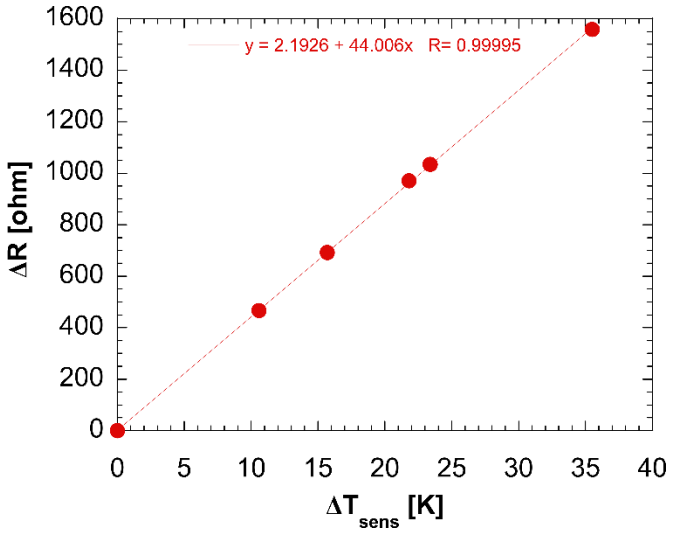


Figure 3.8. Sensor calibration. Resistance of platinum micro sensors depends linearly on temperature around room temperature.[107]

### 3.2.3 Sensing Current, Noise Equivalent Temperature, and Heating Up Substrate

To minimize adverse effects of the nature on the measurements, the following parameters should be optimized: amplitude and frequency of the sensing current, resistance of the sensors, settings of measuring instruments. In this section, we determine the variables in the differential measurement scheme to measure temperature variation due to the near-field radiative heat transfer.

***Amplitude and frequency of the sensing current***

Amplitude and frequency of the sensing current, $I_s$, has impact on the differential measurement method. High amplitude may cause self-heating where the temperature is measured, whereas low amplitude may bury the signal into noise. Determining frequency, as well, has a trade-off. Frequency range close to DC appears as significant noise in voltage reading due to 1/f noise. Increasing reference frequency makes the circuit susceptible to capacitive and inductive coupling. Following the studies carried out in Ref [98], [107]–[109] and running a couple test measurements in the light of the descriptions above, we chose 1-μA AC sensing current with frequency of 375 Hz through the differential circuit. The tests conducted and their results are given in my master thesis [33]. To drive the circuit with the sensing current, we use Keithley 6221 as an AC current source. In addition to driving the current with a right amplitude and at

correct frequency, signal conditioning should be given great care. Regarding this point, lock-in amplifier, the subject of next subsection, needs to be set properly.

***Lock-in amplifier settings***

Voltage output, $v_o$, is measured using the lock-in amplifier, SR7265. Its settings are determined as follows: time constant is set to 5s to filter out the signal outside the pass band (bandwidth) depending on the time constant; filter slop is 18 dB/octave. Response time of the instrument is considered in determination of the time constant and the filter slope. Gain is adjusted automatically by the instrument, and so, input limit; full-scale sensitivity is set to the most suitable value that the least significant digit is below $v_{noise}$ and the electrical measurement circuit only suffers from the noise in the circuit. Averaged over the entire duration of data collection, root mean squared (RMS) noise is $v_{noise} = 0.02\ \mu V$ . The noise voltage is plugged in Eq. 3.6 to calculate NET shown in the next subsection. Even if this value is used in NET calculation, we repeat averaging over duration of each gap distance the near-field experiment is conducted, and the error in the temperature measurement will be the noise calculated for each gap distance separately.

***Noise equivalent temperature (NET)***

We quantify NET of the differential circuit using two methods: 1- Power spectral density measurements using FFT analyzer, and 2- averaging actual lock-in measurements over time.

Figure 3.10 shows power spectral density of voltage signal fed into FFT analyzer when 1μA DC current is driven across the circuit. Around 500 Hz, we measure a power spectral density of $9 \times 10^{-14}\ V^2Hz^{-1}$. Within a bandwidth of 27.5 mHz (used setting in lock-in amplifier for the near-field experiment), we calculate 1.4 mK NET using Eq. 3.6.

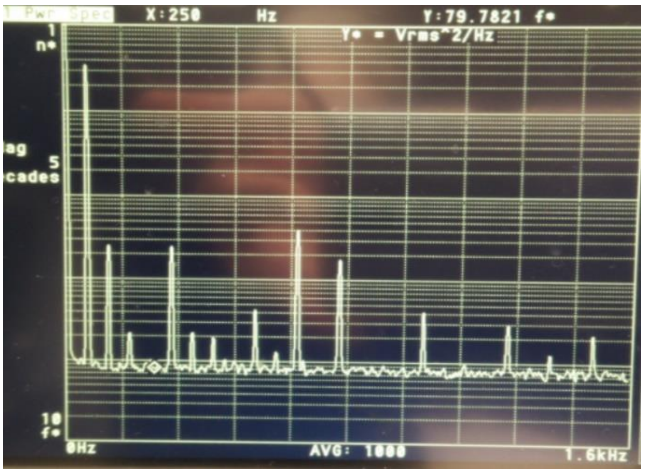


Figure 3.9. Power spectral density measurements in a frequency span of 1.6 kHz. The peaks at various frequencies should be avoided because they are a consequence of equipment around the circuit or of unknown sources. All results are RMS averaging of 1000 data.

We also check NET of the circuit output when connected to the lock-in amplifier (SR7265) used for the near-field experiments. Our voltage measurements reveal RMS NET is ~2 mK for an AC current of 1 μA at a frequency of ~500 Hz driven by a current source (Keithley 6221). This confirms FFT analyzer results, and means our measurement circuit can resolve temperature variation greater than 2 mK.

***Heating up substrate***

To heat up the substrate, a kapton heater (HK5543R78.1L12A) compatible with vacuum conditions is used. To power the heater, we use a power source (TENMA 72-6908) and raise the substrate temperature ($T_{H,base}$) above room temperature ($T_{Room}$) by $\Delta T_{base}$ (= $T_{H,base} - T_{C,base}$). A thermocouple (Omega 5TC-TT-K-40-36), calibrated using a dry block calibrator, is used to measure the surface of the substrate, $T_H$. Figure 3.10 shows the calibration results for $\Delta T$ as a function of voltage supplied to the heater, which closely follows the trend of $V^2$. For the experiments, we supplied constant voltage of 4.5 V, 5.5 V and 6.5 V, and estimated ΔT of 4.8 K, 7.1 K and 9.8 K, respectively.

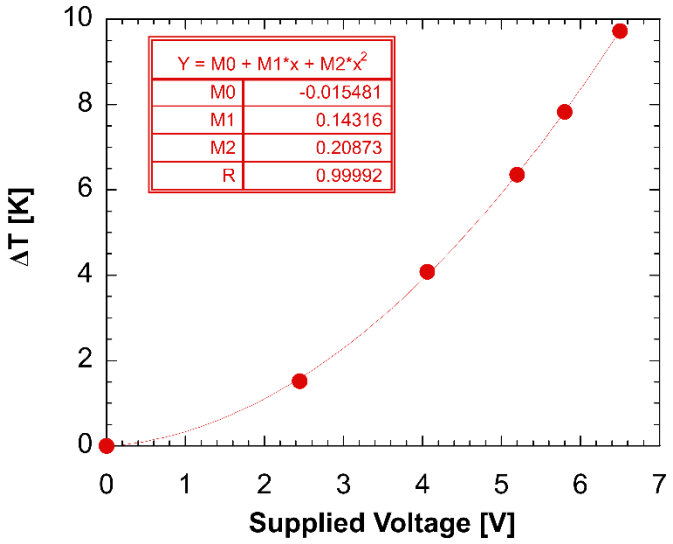


Figure 3.10. Calibration of the substrate temperature, $T_{H,base} = \Delta T_{base} + T_{Room}$.

### 3.2.4 Gap Measurement and Measurable Minimum Gap Distance

Measuring the gap distance is very critical for the near-field experiment. As discussed in Section 3.1.3, the ISPI system suffices to achieve the precise and accurate gap measurement. In addition, the ISPI system used in our lab proved its reliability with a drift < 1 nm over 30 minutes under controlled temperature fluctuations of the environment if a feedback loop is exploited [103].

Surface cleanliness plays an important role for our measurements. In addition to normal cleaning procedures using piranha, acetone/IPA/DI water, plasma cleaning is usually used in between steps as indicated in the procedures above and RF plasma pre-treating (cleaning) is always used before metal deposition. The cleaning procedures are found to be especially necessary during the fabrication of the ISPI mask (with the island) as discussed in the procedures above since the island is subject to a second round of e-beam fabrication of the ISPI marks. The cleanliness of the sensor and island area are also monitored against contamination at each step throughout the fabrication processes using SEM and microscopy. Before experiments, dark field optical microscope (DFOM) images are taken. DFOM is chosen over contact methods such as AFM because of its speed and less chance of contamination. DFOM is also capable of showing nm size particles.[95], [110] Figures 3.11a and b show regions around the near-field interaction

on the substrate and the mask, respectively. Samples are carried in vacuum sample holders, and are exposed to air only under ULPA filters.

Figure 3.11. (a) Dark field optical microscope image of a region around near-field interaction on the substrate. Particles seen in red dashed circles are outside the interaction surface, and has no effect on gap separation. (b) Dark field optical microscope image of the island on the mask. A few bright spots are dead (or saturated) pixels which are confirmed by taking images at different locations. (c) AFM image over 10 μm × 10 μm area on the substrate. Color bar ranges from 2 nm to −2 nm. Scan results show that RMS roughness is <1 nm with a peak-to-peak value of about 4 nm. These values confirm specification of the manufacturer (Quartz Scientific). The plot below the AFM image shows the height profile along the green line in the AFM image. One division of the x-axis is 1 μm and of the y-axis is 1 nm. (d) AFM image over 10 μm × 10 μm area on the mask. Color bar ranges from 1.7 nm to −1.9 nm. Scan results demonstrate an RMS roughness of < 1 nm with a peak-to-peak value of < 4 nm. These values confirm specification of the manufacturer (Mark Optics). The plot below the AFM image shows height profile along the green line on the AFM scan. A division of the x-axis is 1 μm and of the y-axis is 0.5 nm. (e) Flatness measurement of the substrate. The red curve shows the measured profile over the entire length of the bulk substrate, the green is the reference for a flat surface. Height variation over 20 mm is 350 nm. (f) Flatness measurement of the mask. Height variation over 11 mm is 70 nm. The bumps in the image shows features fabricated on the surface.

a)

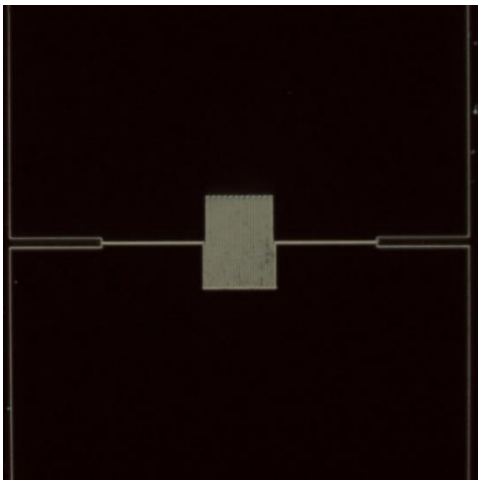

b)

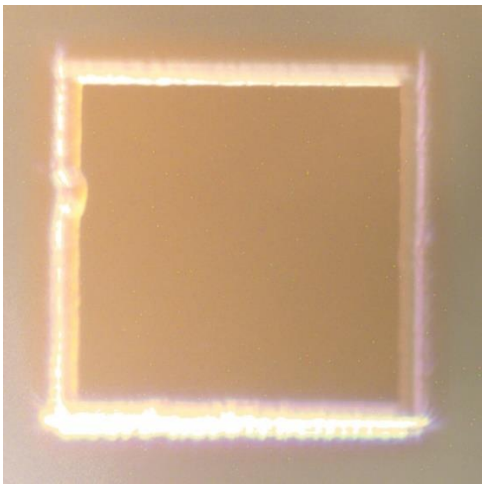

c)

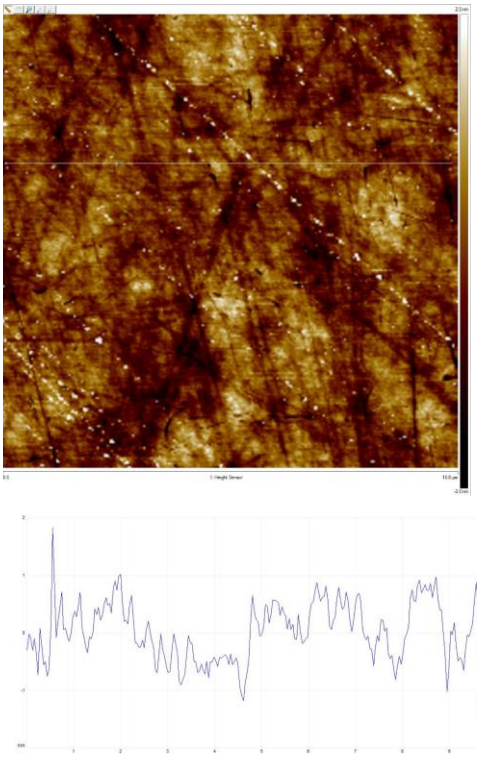

d)

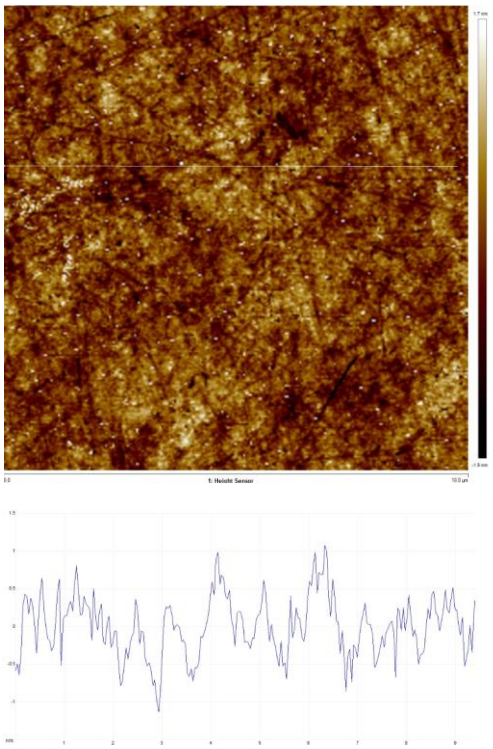

e)

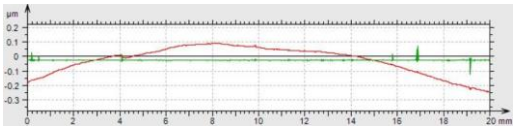
µm
0.2
0.1
0
-0.1
-0.2
-0.3
0
2
4
6
8
10
12
14
16
18
20 mm

f)

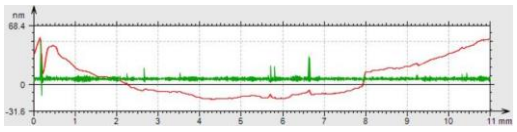
nm
68.4
0
-31.6
0
1
2
3
4
5
6
7
8
9
10
11 mm

To analyze the surface roughness of both the near-field interaction surfaces, AFM scans are performed on spare substrate and mask that are from the same batch of the samples used in the near-field experiment. Figure 3.11c and d show images of AFM scans. We evaluate RMS roughness of the substrate as < 1 nm and of the mask as < 1 nm. Also, the scans show that peak-to-peak roughness is 4 nm for the substrate and < 4 nm for the mask. We also consider flatness in our measurements. The flatness is defined as the maximum deviation of a point on the surface from a flat surface, measured against the entire surface. Based on our measurements using a stylus profiler (KLA P17) and shown in Figure 3.11e and f, the flatness of the substrate is 350 nm over 20 mm, and that of the mask is 70 nm over 11 mm. These values correspond to a deviation of 2 nm in flatness for the substrate and of < 1 nm for the mask over interaction area with a side length of 100 μm.

For the temperature sensors, our goal is to embed Pt wires in the recessed area without any extension above the substrate surface. Height profile of Pt trace over a line is measured. Figure 3.12a shows schematic design of a sensor and line over which height profile is measured. The measurement results, seen in Figure 3.12b, reveals that height of the sensor is about 2 nm below the substrate surface. Figure 3.12b also shows that depth of the recessed area around the sensor is 30 nm.

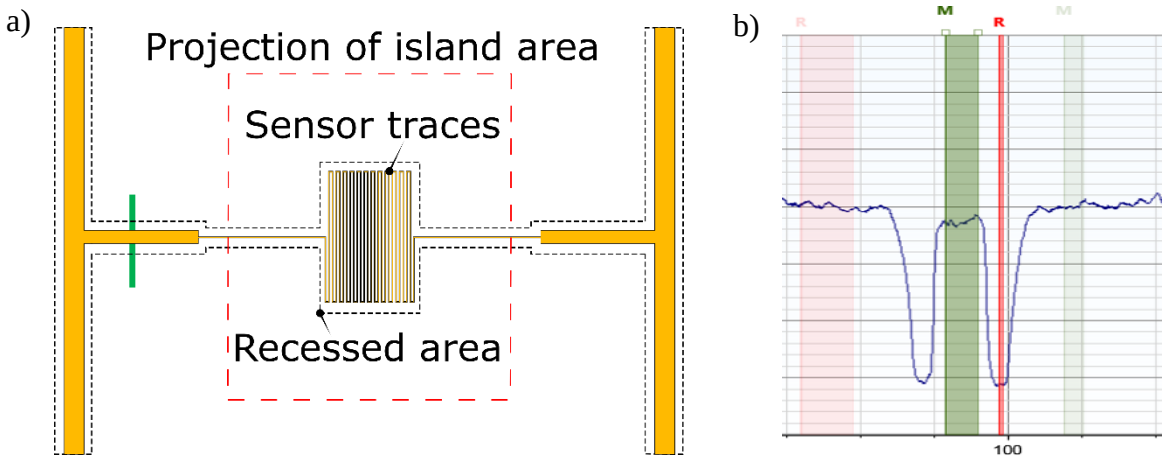


Figure 3.12. (a) Location of height profile scanning on outer Pt trace (Green line). (b) Height profile over the green line in (a). The horizontal axis is the position over the green line in (a), the vertical axis represents height. A division in horizontal (vertical) axis is 10 μm (2 nm). Green colored area shows Pt trace below the surface level. Red line shows depth of the recessed area.

### 3.2.5 Experiment Procedure

Step by step, we list the procedure, which will be followed to accomplish the data collection of the near-field radiation experiment.

1. Remove substrate holder, and fix the substrate on the holder. Replace the holder.
2. Align the substrate using tip/tilt adjustment until the reflected beam from the substrate forms image on the screen used for coarse alignment.
3. Remove mask holder, and fix the mask on the holder. Replace the holder.
4. Align the mask using the 3-point adjustment holder until the reflected beam from the mask interferes with that from the substrate. Roughly, minimize the fringes to parallelize the samples.
5. With small deviations from the minimum number of fringes, approach the mask towards the substrate using the 3-point screws.
6. Position the ISPI scope on one of the gratings to observe reflection of the TCG.
7. Repeat the approach until the gap between the mask and the substrate is < 150 nm, which is the translation range of the piezo stage controlling the substrate position with 5-axis ($x$, $y$, $z$, $\theta_x$, $\theta_y$).
8. Close the chamber door, and pump down the chamber.
9. Turn on the heater to bring $T_H$ to $T_{H,base}$.
10. Using the 5-axis piezo stage, raise the substrate. Simultaneously, control gap readings from at least three TCGs to make sure that the parallelism is sustained.
11. At near contact, confirm the parallelism between the two plates by observing the sensing temperature variation in response to tip-tilt adjustment (See Section 3.2.6).
12. Retract the substrate for the desired gap value with an increment specific to the gap range.
13. At each gap value recorded, wait the system to reach thermal equilibrium, and, collect the voltage signal for enough duration under equilibrium.

### 3.2.6 Confirmation of Parallelism using Temperature Readings

We further use temperature readings in the near-field distances to make sure the mask and the substrate are in parallel, as indicated in step 11 in Section 3.2.5. When the surfaces are parallel at a separation distance, the near-field radiative heat transfer is maximum; hence, the

temperature of the sensing sensor reaches its minimum. Any deviation from the parallelism leads to less heat transfer and a higher temperature reading. We rotate substrate around the two in-plane axes, x and y, using a piezo nanopositioner (MCL Nano series). Figure 3.13 shows an example of the measured temperature variation in response to the rotation around one axis. The results show that temperature reading can be used to confidently indicate an angular deviation less than 0.02 mrad. This corresponds to 2 nm uncertainty in height across 100 μm × 100-μm area.

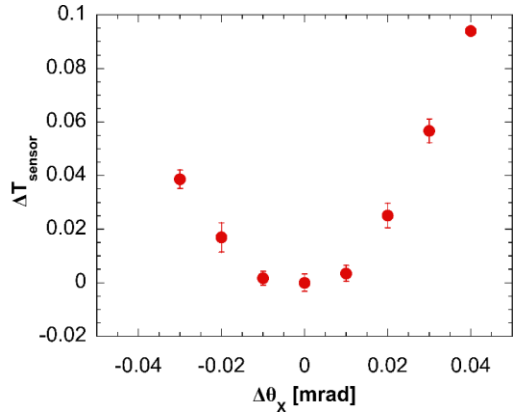


Figure 3.13. Determination of parallelism between two near-field interaction surfaces on the mask and the substrate. Temperature reading varies in response to tilt adjustment.

### 3.2.7 Near-field Radiative Heat Transfer Experiment Results

Once the fine parallel alignment is done to the best of the system's capability, the substrate is retracted and then the gap is gradually reduced to take the temperature readings. Figures 14a-c show $\Delta T_{rel}$ in the region of the gap $d$ less than 80 nm, for $\Delta T$ (the temperature difference between the substrate and the mask away from the island) of 4.8 K, 7.1 K and 9.8 K, respectively. The experimental measurements show a rapid increase in $\Delta T_{rel}$ with the decreasing gap separation. This is particularly notable when the gap is reduced to below ~ 25 nm.

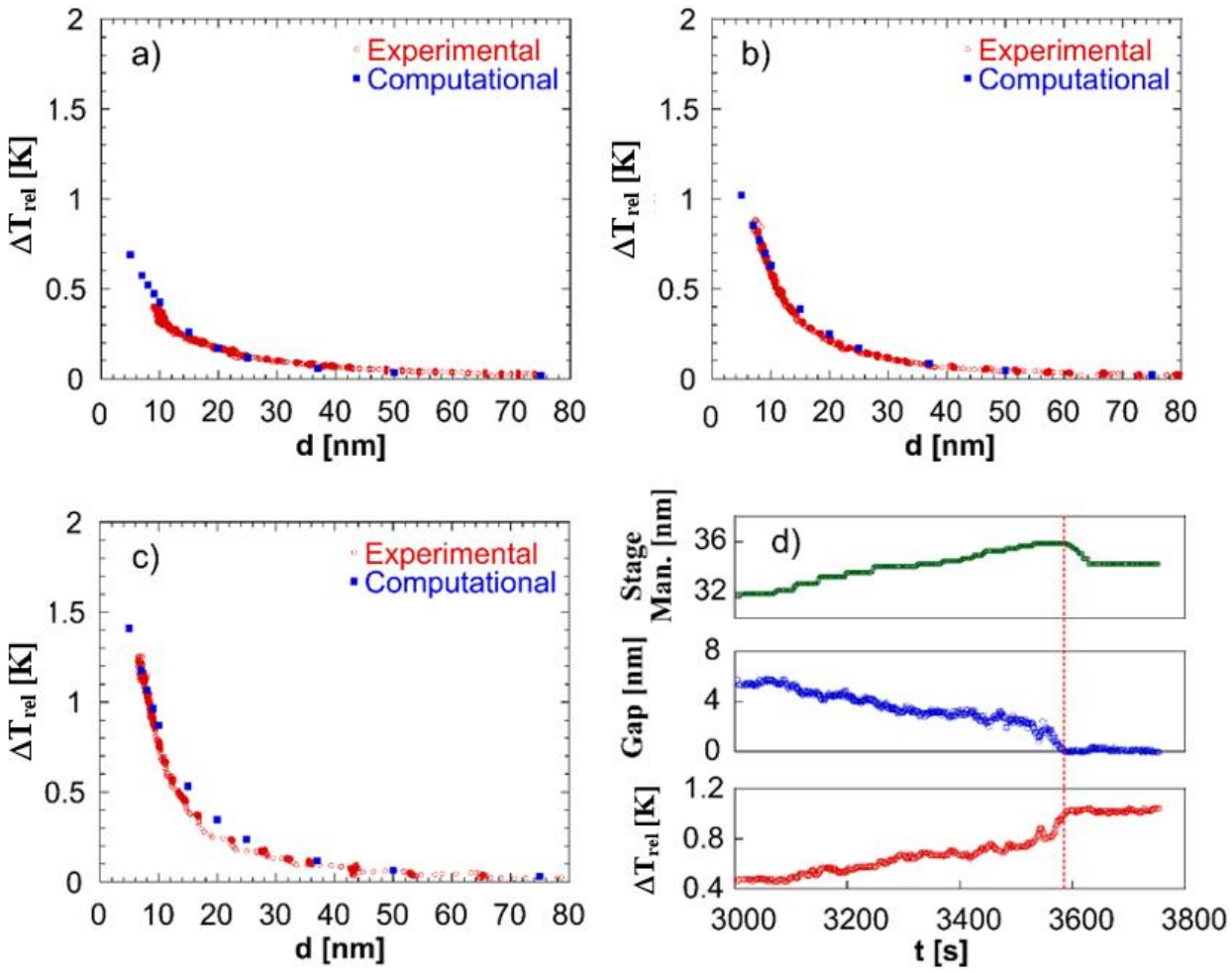


Figure 3.14. Comparison of measured and computed temperature variation for $\Delta T$ (the temperature difference between the substrate and the mask at locations far from the near-field interaction regions) of (a) 4.8 K, (b) 7.1 K and (c) 9.8 K. Experimental results agree with computations from near-field radiation theory. For the computational results in (a)-(c), the uncertainty ranges from ~ ±12% at $d$ = 25 nm to ~ ±6% at $d$ = 7 nm. (d) Real-time approaching data of stage manipulation (top, green), the corresponding ISPI gap reading (middle, blue) and the temperature reading (bottom, red) for $\Delta T$ = 7.1 K. The stage reading (top, green) is not absolute. The red dashed vertical line indicates contact. Right before the contact, ISPI gap reading shows sudden drop. At the contact, temperature jumps as well.

Figure 3.14d shows real-time data of gap manipulation (top), ISPI gap reading (middle), and temperature reading (bottom) vs. time for the case with $\Delta T$ = 7.1 K. As the mask is approaching the substrate using the piezoelectric nanopositioner, the ISPI reading shows the corresponding decrease in the gap. The decrease in the gap results in temperature change due to near-field radiation (cooling of the surface underneath the island). There is a sudden jump in ISPI

reading and temperature reading at contact in Figure 3.14d, which lasts over a distance of 1−2 nm. After that the readings do not change in the time window shown in Figure 3.14d. The contact point is assigned as 0 gap in ISPI reading as the ISPI reading is relative (see Supporting Information 1). The red dashed line indicates the time of the contact. We notice that when these sudden changes happen, they cannot be easily reversed even when we try to retract the distance as seen in the top green line in Figure 3.14d. Larger manipulation (using more than 10 nm input in the piezoelectric nano-manipulator) does break the contact (not shown in figure).

The experimental data $\Delta T_{rel}$ in Figures 14a-c are plotted starting from the smallest gap of ~7 nm, which match with the computational results (see below). The reasons for this 7 nm gap can be the combination of the peak-to-peak roughness of the sample surfaces (~ 2 nm above the surface level of substrate sensing area, and < 2 nm above that of the island, the RMS roughness is about 1 nm, see Section 3.2.4), the flatness of the samples (< 1 nm for the mask and 2 nm for the substrate, see Section 3.2.4), the parallelism achieved between the substrate and the mask (0.02 mrad or 2 nm, as discussed previously) and possibly a jump due to attractive forces at 1−2 nm separation distance (Figure 3.14d). The last point is also consistent with experimental observation of strong attraction between the mask and the substrate. The collect effects of all the above contribute to a smallest distance of about 7 nm that we can measure the near-field radiation.

The computed $\Delta T_{rel}$ in Figures 14a-c are obtained based on the theoretical heat flux of near field radiation (see Section 3.2.1 the computation model). We also show this theoretical near-field heat flux, $q_{NF}$, computed using fluctuational electrothermodynamics,[31] in Figure 3.15a. The experimental heat flux is the heat flux that produces the measured temperature variations shown in Figures 14a-c. The drastic increase in the near-field heat flux is well documented,[6], [30], [88] due to enhancement in energy transport by surface phonon polaritons excited at near resonance frequencies (see Section 1.3 for the theoretical calculation).

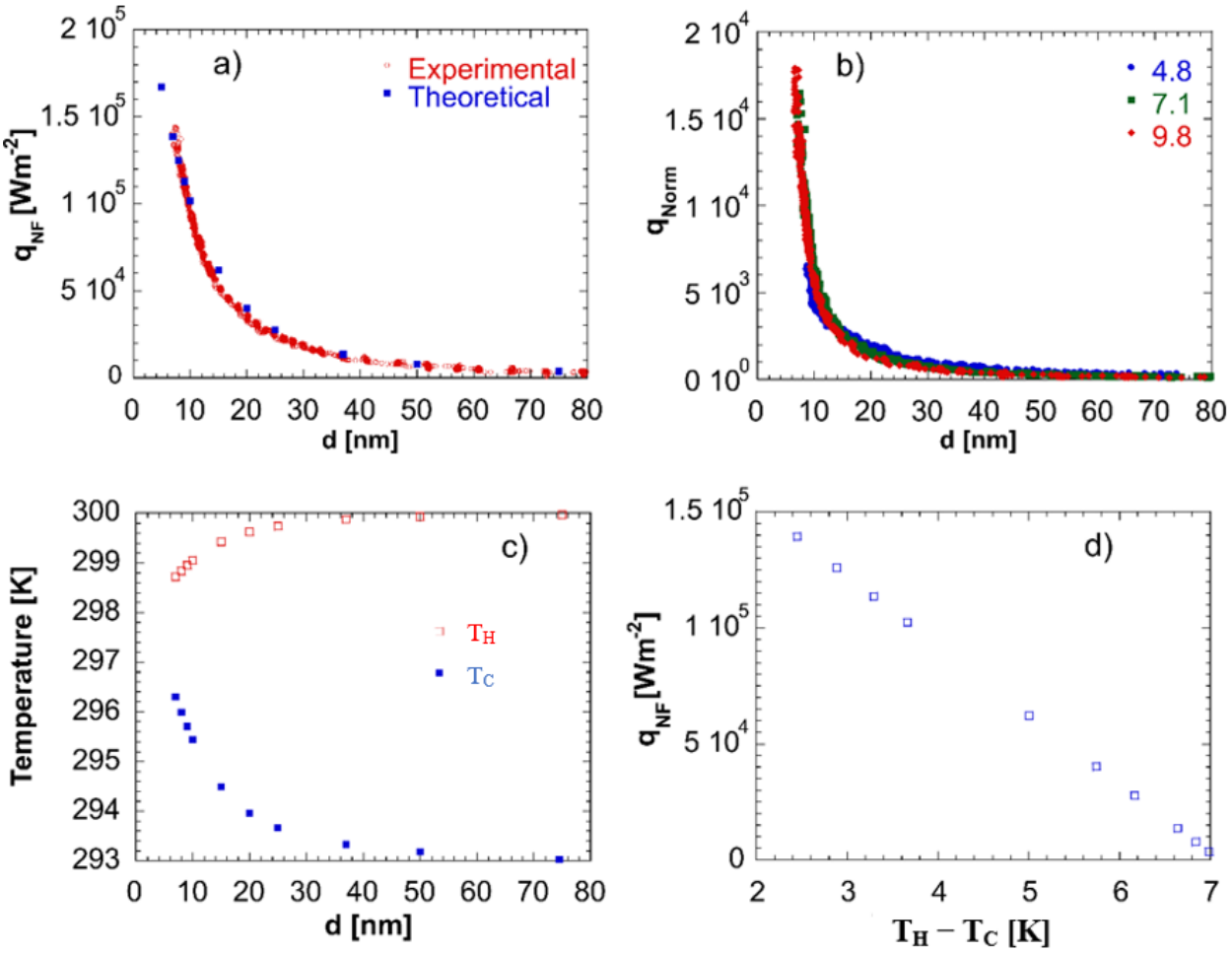


Figure 3.15. (a) Experimental vs theoretical near-field heat flux vs. separation gap for $\Delta T$ = 7.1 K. Uncertainty in $q_{NF}$ is ~ ±2% at $d$ = 25 nm, increases with decreasing gap up to ~ ±9% at $d$ = 7 nm. (b) Experimental $q_{Norm}$, the normalized heat flux with respect to blackbody, for all $\Delta T$ used. (c) Temperature change over the distance between the two surfaces. $T_H$ and $T_C$ represent the temperature of the surface around the sensor on the substrate (hot surface) and the temperature of the island (cold surface), respectively. (d) Near-field radiative heat flux with respect to the temperature difference of the hot and cold surfaces when $\Delta T$ = 7.1 K.

To further analyze near-field radiation enhancement, we define a normalized radiative heat flux, $q_{Norm}$, expressed as ratio of $q_{NF}$ to the far-field radiative heat transfer, $q_{FF}$, for the same temperature difference. Figure 3.15b shows $q_{Norm}$ for $\Delta T$ = 4.8, 7.1 K and 9.8 K. We find that the normalized radiative heat flux overlaps for the three $\Delta T$, indicating the reliability of the experimental results. We calculate a standard deviation of ~ 460, ~ 700, and ~ 90 for a mean of ~ 14500, ~ 5400, and ~ 1530 at 7 nm, 10 nm, and 20 nm gap separations, respectively. The

experimental results also agree with theoretical computations down to 7 nm, showing a more than 4 orders enhancement in near-field thermal radiation ($q_{Norm}$~18,000).

Figure 3.15c shows the change in temperatures of the hot and cold surfaces exposed to near-field thermal radiation over the distance between the surfaces. The temperature of the hot surface, $T_H$, cools down with the decreasing gap, and the temperature of the cold surface, $T_C$, heats up with the decreasing gap due to near-field heat transfer. We note that, similar to the observation of the notable variation in $\Delta T_{rel}$ in Figure 3.14b, $T_H$ and $T_C$ also change significantly below 25 nm. We also notice that the rate of temperature change for the hot surface over the distance is less than that for the cold surface. This arises from the difference in thermal conductivity, that the thermal conductivity of the substrate of the hot surface is greater than that of the mask of the cold surface (See Section 3.2.1 for thermal conductivity). We also show the near-field heat flux as a function of the temperature difference between the hot and cold surfaces ($T_H - T_C$) in Figure 3.15d when $\Delta T$ = 7.1 K. Despite of decrease in the temperature difference, heat flux, $q_{NF}$, grows approximately linearly with the temperature difference.

Lastly, we anticipate that the experimental technique presented in this work can be used to probe near-field heat transfer between two surfaces at even closer distances. The experiments can be further optimized, for example, by reducing the roughness of the surfaces from processing and using substrates with better flatness. The method can also be extended to study radiative heat transfer between other types of materials such as metasurfaces.

## 3.3 Summary

In this chapter, we proposed an experimental technique to measure near-field radiative heat transfer. Special geometry of the two objects undergone near-field radiation was explained. The regions formed by the geometry were detailed, and temperature profiles over the regions were discussed. A differential measurement circuit based on resistive thermometry to measure the defined temperatures was outlined. To predict the defined temperatures, a computational method was employed. The method exploits a commercially available package program and relies on convective heat transfer coefficient to mimic near-field radiative heat transfer. Results of the method helped design the temperature measurement circuit and calculate near-field radiative heat

transfer as a function of gap distance for the calculated temperature profiles. This section was concluded with alignment and gap control technique. The next section presented a gap measurement technique with high precision for gap measurement, dynamic gap control, and reliable sensitivity for extreme near-field measurements. We implemented the technique explained in Section 3.1 to our experiment. Temperatures on the active surfaces of quartz samples were predicted. By means of the estimated temperature profiles, the temperature sensors, made of platinum, were designed, and their characterizations were reported. In addition, the variables of the differential measurement circuit, such as the amplitude and reference frequency of the sensing current, were determined. Additional variables limiting our experiment were discussed, and the noise equivalent temperature arising from the noise in the circuit and the minimum achievable gap reading due to surface roughness, flatness, the vibration of the setup and the possible contamination were assessed. Finally, a procedure including the experiment steps to collect the near-field radiation data was listed. We reported experimental results and observed 18,000 times enhancement in thermal radiation at the smallest gap achieved. Our study validates theoretical framework (fluctuation-dissipation theorem) down to separation region below 10 nm.

# 4. NEAR-FIELD THERMAL RADIATION BY BULK POLARITONS IN HYPERBOLIC MATERIALS

This chapter has been partially reproduced from a previous publication*: Salihoglu, H.; Xu, X. Near-field radiative transfer by bulk hyperbolic polaritons across vacuum gap*. *Int. J. Heat Mass Transf.* ***2021****, 170, 120984.*

Until this chapter, radiation has been investigated for the condition that thermal emission is from an object at uniform temperature. However, thermal radiation can also be emitted from a surface that has a temperature gradient into the surface. Our study, presented in Chapter 5, has shown, in a hyperbolic material, a temperature gradient can drive radiation inside the hyperbolic material due to the large number of the propagating bulk hyperbolic phonon polaritons (HPhP) modes in Reststrahlen bands. So far, contribution of HPhP modes to near-field radiative heat transfer has been analyzed as surface modes using the two body formalism as explained in Chapter 1 and 2. Importantly, our work in Chapter 5 has shown that the radiation heat flux in hBN can be comparable to phonon conduction. In this chapter, our aim is to understand the physical process of near-field radiation arising from HPhPs, driven by a temperature gradient inside hyperbolic materials. Developed in this chapter, many-body approach considers radiation between planar objects with non-uniform temperature and across a vacuum gap. Several studies have implemented this method to study radiation, for example, to take into account carrier concentration gradient [111] or layered material structures [112], [113]. Findings in this chapter will help compare many-body and two-body approaches. This chapter also elucidates the detailed processes of propagation of HPhPs across a vacuum gap and their contribution to near-field radiative transfer in the presence of temperature gradients in the material.

## 4.1 Theoretical Framework

In this section, first, the two-body approach is summarized with important details. Then, many-body approach derived for radiative heat transfer calculations from planar objects with nonuniform temperature is presented.

### 4.1.1 Formalism of near-field radiative transfer for two-body system with uniform temperature

To describe two-body system, two planar continuous media, each at a uniform temperature and separated by a vacuum gap, *d*, along the $z$ axis ($\perp$) are considered and are in contact with hot and cold reservoirs at $T_H$ and $T_C$, respectively, in the x-y plane ($\parallel$). Hot (1) and cold (2) media are at reservoir temperatures, $T_1 = T_H$ and $T_2 = T_C$. Heat flux (the net radiative heat transfer) from medium 1 to 2 reads: [31]

$$q^2 = -q^1 = \int \frac{d\omega}{2\pi} [\Theta(\omega, T_1) - \Theta(\omega, T_2)] \int_{\omega/c}^{\kappa_{max}} \frac{d\kappa}{2\pi} \kappa \sum_{i=s,p} \mathcal{T}_q^{1,2} \tag{4.1}$$

This equation is in the same form of Eq. 1.16 with different notations. For sake of completeness, Eq. 4.1 is given. Here, $\Theta(\omega, T)$ is mean energy of Planck oscillators with frequency $\omega$ at temperature T, and is given by $\hbar\omega/(e^{\hbar\omega/k_B T} - 1)$, where $\hbar$ and $k_B$ are the reduced Planck constant and Boltzmann constant, respectively. $\kappa$ denotes the wave vector component parallel to planar surface ($k = \boldsymbol{\kappa} + k_z\hat{z} = k_x\hat{x} + k_y\hat{y} + k_z\hat{z}$, where $\hat{x}$ is unit vector in x direction). Since the contribution from propagating waves in vacuum ($\kappa < \omega/c$) is negligible for near-field regime of interest, we only consider the contribution of evanescent waves in vacuum ($\kappa > \omega/c$). Each mode represented by $\kappa$ corresponds to a channel that energy can flow through. Energy transmission across the vacuum gap by a mode is expressed by an energy exchange function, $\mathcal{T}_q^{1,2}$, as (same with Eq. 1.18): [31]

$$\mathcal{T}_q^{1,2} = \frac{4Im(r_1^q)Im(r_2^q)e^{-2Im(k_{z,o})d}}{\left|1 - r_1^q r_2^q e^{2ik_{z,o}d}\right|^2} \tag{4.2}$$

$\mathcal{T}_q^{1,2}$ represents the fraction of energy across the vacuum gap and is equal to or smaller than 1. The exponential term cuts off contributions from modes with wave vectors $Im(k_{z,o}) \gg d^{-1}$. For waves supported at resonant frequencies, $\left|1 - r_1^q r_2^q e^{2ik_{z,o}d}\right|^2$ becomes very small and compensates for the exponential decay of waves. In this case, $\mathcal{T}_q^{1,2}$ approaches unity.

Derivation of Eq. 4.1 starts from the expression of thermal radiation, the ensemble averaged Poynting vector $\langle \boldsymbol{S}(z, \omega, T)\rangle_z$ from medium 1 at temperature *T* to an observation point $z$ in medium 2: [6]

$$\langle S_z(z, \omega, T)\rangle = \frac{\omega^2}{c^2} \frac{\Theta(\omega, T)}{\pi^2} Re\left\{ i \int_{z'} dz' \int d\kappa\, \kappa \left( g_{Ex\alpha} \varepsilon''_{\alpha\alpha} g^*_{Hy\alpha} - g^*_{Hx\alpha} \varepsilon''_{\alpha\alpha} g_{Ey\alpha} \right) \right\} \tag{4.3}$$

Repeating indices are summed, and index $\alpha$ represents an orthogonal component (x, y, z). Subscript $z$ indicates the $z$ component of Poynting vector, $c$ is speed of light in vacuum and $\varepsilon''_{\alpha\alpha}$ is the imaginary part of diagonal component of dielectric tensor. $z'$ represents the coordinate, and integration over $z'$ is performed for medium 1. $g_{Ex\alpha}$ and $g_{Hy\alpha}$ are the Weyl components of dyadic Green tensor of electric and magnetic fields, respectively [6]. The Weyl tensor for the electric field is given as

$$\overleftrightarrow{g}_E(\kappa, z, z', \omega) = \frac{i}{2}\frac{1}{k_{z,1}^q}\sum_{q=p,s}\tau_{1\to 2}^q \boldsymbol{E}_q(z,\kappa)\otimes\boldsymbol{E}_q(z',\kappa) \tag{4.4}$$

$\tau_{1\to 2}^q$ is transmission function for the vacuum gap and $\tau_{1\to 2}^q = \frac{t_{1+}^q t_{2-}^q e^{2ik_{z,o}d}}{1-r_1^q r_2^q e^{2ik_{z,o}d}}$ where $r_1$ and $r_2$ are Fresnel reflection coefficients for interfaces between hot-side and vacuum (1) and cold-side and vacuum (2), and are given as $r_i^p = \frac{\varepsilon_\parallel k_{z,o} - k_z^p}{\varepsilon_\parallel k_{z,o} + k_z^p}$ for p-polarization and $r_i^s = \frac{k_{z,o} - k_z^s}{k_{z,o} + k_z^s}$ for s-polarization at interface $i$ $(= 1, 2)$, where $k_{z,o}$ $\left(= [\omega^2/c^2 - \kappa^2]^{1/2}\right)$ is the out-of-plane component of wave vector in vacuum. $t_{i-}^q$ is the Fresnel transmission coefficient from vacuum to material (−) at interface $i$ for polarization $q$ and is given as $t_{i-}^p = \frac{2\sqrt{\varepsilon_\parallel}k_{z,o}}{\varepsilon_\parallel k_{z,o} + k_{z,i}^p}$ for p-polarization, and $t_{i-}^s = \frac{2k_{z,o}}{k_{z,o} + k_{z,i}^s}$ for s-polarization. The Weyl components of the tensor given in Eq. 4.4 relate a source point in medium 1 with an observation point in medium 2 via the transmission from medium 1 to 2 across the vacuum gap, $\tau_{1\to 2}^q$. $\boldsymbol{E}_q(z',\kappa)$ is right going wave at $z$ = 0 (the interface of the hot medium) originated from unit strength wave at $z'$ in medium 1, and $\boldsymbol{E}_q(z,\kappa)$ is wave at $z$ in medium 2 originated from unit strength wave at $d$ (the interface of the cold medium):

$$\boldsymbol{E}_q(z',\kappa) = \boldsymbol{e}_{q+}e^{-ik_{z,1}^q z'} \tag{4.5}$$

$$\boldsymbol{E}_q(z,\kappa) = \boldsymbol{e}_{q+}e^{ik_{z,2}^q (z-d)} \tag{4.6}$$

$\boldsymbol{e}_{q+}$ is the polarization vector for waves propagating to the right direction (+) and for s-polarization $\boldsymbol{e}_{s+}^j = \frac{1}{\kappa}\left(k_y\hat{x} - k_x\hat{y}\right)$, and for p-polarization, $\boldsymbol{e}_{p+} = \frac{1}{k}\left(-k_z^q\frac{\boldsymbol{\kappa}}{\kappa} + \frac{\varepsilon_\parallel}{\varepsilon_\perp}\kappa\hat{z}\right)$. $k_{z,1}^q$ is the out-of-plane component of wave vector in medium 1. $k_z^s = [\varepsilon_\parallel\omega^2/c^2 - \kappa^2]^{1/2}$ for s-polarization and $k_z^p = [\varepsilon_\parallel\omega^2/c^2 - \varepsilon_\parallel/\varepsilon_\perp\kappa^2]^{1/2}$ for p-polarization. The expressions of the Weyl components for a source point at $z'$ in medium 1 and an observation point at $z$ in medium 2 for the two-body system are found to be:

$$g_{Exx}^{j\gamma} = \frac{i}{2}\frac{1}{k_{z,1}^{p}}\frac{k_{z,2}^{p}}{k_2}\frac{k_{z,1}^{p}}{k_1}\tau_{1\to 2}^{p}\left\{e^{ik_{z,2}^{p}(z-d)}\right\}e^{-ik_{z,1}^{p}z'} \tag{4.7}$$

$$g_{Exz}^{j\gamma} = -\frac{i}{2}\frac{1}{k_{z,1}^{p}}\frac{\varepsilon_{\parallel}}{\varepsilon_{\perp}}\frac{k_{z,\gamma}^{p}}{k_\gamma}\frac{\kappa}{k_j}\tau_{1\to 2}^{p}\left\{e^{ik_{z,2}^{p}(z-d)}\right\}e^{-ik_{z,1}^{p}z'} \tag{4.8}$$

$$g_{Eyy}^{j\gamma} = \frac{i}{2}\frac{1}{k_{z,1}^{s}}\tau_{1\to 2}^{s}\left\{e^{ik_{z,2}^{s}(z-d)}\right\}e^{-ik_{z,1}^{s}z'} \tag{4.9}$$

$$g_{Ezx}^{j\gamma} = -\frac{i}{2}\frac{1}{k_{z,1}^{p}}\frac{\varepsilon_{\parallel}}{\varepsilon_{\perp}}\frac{\kappa}{k_2}\frac{k_{z,1}^{p}}{k_1}\tau_{1\to 2}^{p}\left\{e^{ik_{z,2}^{p}(z-d)}\right\}e^{-ik_{z,1}^{p}z'} \tag{4.10}$$

$$g_{Ezz}^{j\gamma} = \frac{i}{2}\frac{1}{k_{z,1}^{p}}\frac{\varepsilon_{\parallel}^{2}}{\varepsilon_{\perp}^{2}}\frac{\kappa^2}{k_2 k_1}\tau_{1\to 2}^{p}\left\{e^{ik_{z,2}^{p}(z-d)}\right\}e^{-ik_{z,1}^{p}z'} \tag{4.11}$$

Here, $k_i(=\sqrt{\varepsilon_{\parallel}}\frac{\omega}{c})$ is the magnitude of wave vector in medium *i* (=1,2).

We are able to express the Weyl components apart from the dyadic Green's function because the dyadic Green's function for electric field can be expanded in the following form for planar structures owing to symmetry in x-y plane [6], [15]

$$\overleftrightarrow{\boldsymbol{G}}^{E}(\boldsymbol{r},\boldsymbol{r}',\omega) = \int \frac{d^2\kappa}{(2\pi)^2}\overleftrightarrow{g}_{E}(\kappa,z,z',\omega)e^{i\boldsymbol{\kappa}.(\boldsymbol{R}-\boldsymbol{R}')} \tag{4.12}$$

Here, $\boldsymbol{r} = \boldsymbol{R} + z\hat{z} = (x\hat{x} + y\hat{y} + z\hat{z})$, and $\overleftrightarrow{g}_E$ is given in Eq. 4.4. Note that $\overleftrightarrow{\boldsymbol{G}}^{H}$ has the same form of 4.12 with $\overleftrightarrow{g}_H$ in place of $\overleftrightarrow{g}_E$. For components of $\overleftrightarrow{g}_H$ used in Eq. 4.3, we evaluate $\overleftrightarrow{\boldsymbol{G}}^{H} = \nabla_r \times \overleftrightarrow{\boldsymbol{G}}^{E}$, and extract $\overleftrightarrow{g}_H$ out of the equality. Consequently, the Weyl components for magnetic field are:

$$g_{Hxy}^{j\gamma} = \frac{1}{2}\frac{1}{k_{z,1}^{s}}k_{z,2}^{s}\tau_{1\to 2}^{s}\left\{e^{ik_{z,2}^{s}(z-d)}\right\}e^{-ik_{z,1}^{s}z'} \tag{4.13}$$

$$g_{Hzy}^{j\gamma} = -\frac{1}{2}\frac{1}{k_{z,1}^{s}}\kappa\tau_{1\to 2}^{s}\left\{e^{ik_{z,2}^{s}(z-d)}\right\}e^{-ik_{z,1}^{s}z'} \tag{4.14}$$

$$g_{Hyx}^{j\gamma} = -\frac{1}{2}\frac{1}{k_{z,1}^{p}}\frac{k_{z,1}^{p}}{k_2 k_1}\left[\left(k_{z,\gamma}^{p}\right)^2 + \frac{\varepsilon_{\parallel}}{\varepsilon_{\perp}}\kappa^2\right]\tau_{1\to 2}^{p}\left\{e^{ik_{z,2}^{p}(z-d)}\right\}e^{-ik_{z,1}^{p}z'} \tag{4.15}$$

$$g_{Hyz}^{j\gamma} = \frac{1}{2}\frac{1}{k_{z,1}^{p}}\frac{\kappa}{k_2 k_1}\frac{\varepsilon_{\parallel}}{\varepsilon_{\perp}}\left[\left(k_{z,\gamma}^{p}\right)^2 + \frac{\varepsilon_{\parallel}}{\varepsilon_{\perp}}\kappa^2\right]\tau_{1\to 2}^{p}\left\{e^{ik_{z,2}^{p}(z-d)}\right\}e^{-ik_{z,1}^{p}z'} \tag{4.16}$$

We derived the Weyl components for magnetic and electric fields and now evaluate Poynting vector in Eq. 4.3. To find the total radiative energy from medium 1 to 2, the Poynting vector is evaluated at the surface of medium 2 ($z = d$) and infinity. The difference of these Poynting vectors yield the total radiative energy from medium 1 to 2. The procedure is repeated for that from medium 2 to 1, and the difference of the two is the net radiative heat flux expressed in Eq. 4.1.

### 4.1.2 Formalism of near-field radiative transfer for many-body system with nonuniform temperature

To account for the temperature gradient in the media, a many-body scattering method is used and shown in Figure 4.1. The global system consists of *N* bodies or slabs (slabs 1 and *N* are hot and cold reservoirs, respectively), and each slab, labelled with *j*, *γ*, or *m* in Figure. 4.1 is at a local equilibrium temperature. We consider a uniaxial material with out-of-plane component (⊥) lying along the *z* axis, and in-plane components (∥) within the invariant x-y plane.

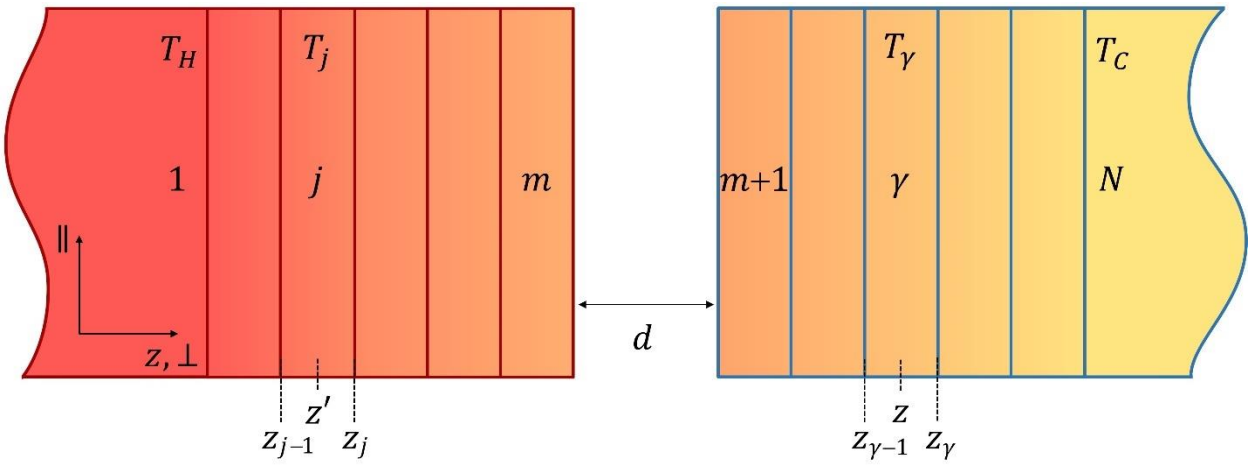


Figure 4.1. Many-body system of two semi-infinite media with temperature gradient. Slabs extend to infinity in the in-plane ∥ direction (x, y plane). The global system consists of *N*-bodies or slabs, and slabs 1 and *N* correspond to hot and cold reservoirs at constant temperatures $T_H$ and $T_C$, respectively. Undergoing radiative heat exchange, intermediate slabs reach their local equilibrium temperature, $T_j$. The region between two media is the vacuum gap with separation *d*. Position of slabs *j* and *γ* represented here corresponds to the second scenario.

Derivation of radiative heat transfer from an emitting slab labelled as $j$ to a point $z$ in a receiving slab $\gamma$, starts from Eq. 4.3. Based on relative positions of the slabs, the Weyl components in Eq. 3 need to be derived, which here relate the source point originated at $z'$ in slab $j$ with an observation point $z$ in slab $\gamma$. Three scenarios can occur: 1, both slabs are in the left (hot) medium; 2, the two slabs are in separate medium; and 3, both are in the right (cold) medium. In all scenarios, we analyze the case that the emitter is located to the left of the receiver, and the reversed situation can be obtained from reciprocity. For derivation, the Green's function method [15] is used, and the Weyl tensor of electric field for slabs $j$ and $\gamma$, $\overleftrightarrow{\mathcal{G}}_E^{j\gamma}$, can be expressed as:

$$\overleftrightarrow{\mathcal{G}}_E^{j\gamma}(\kappa, z, z', \omega) = \frac{i}{2}\frac{1}{k_{z,j}^q}\sum_{q=p,s}\tau_{j+1\to\gamma-1}^q \boldsymbol{E}_q^{\gamma}(z,\kappa)\otimes\boldsymbol{E}_q^{j}(z',\kappa) \tag{4.17}$$

Here, the second scenario is mostly referred, where $\tau_{j+1\to\gamma-1}^q$ represents the transmission of waves emanating from the surface of slab $j$, transmitting in medium 1 towards the vacuum gap ($\tau_{j+1\to m}^q$), across the vacuum gap ($T^q$), and in medium 2 reaching the surface of slab $\gamma$ ($\tau_{m+1\to\gamma-1}^q$), and is expressed as $\tau_{j+1\to m}^q T^q \tau_{m+1\to\gamma-1}^q$. $T^q$ has the same expression as the transmission function in the two-body formalism, $\tau_{1\to 2}^q$. $m$ and $m$+1 are the slabs adjacent to the vacuum gap as shown in Figure 4.1. $k_{z,j}^q$ is normal component of wave vector in slab $j$. $\boldsymbol{E}_q^j$ and $\boldsymbol{E}_q^{\gamma}$ are expressed as:

$$\boldsymbol{E}_q^j(z',\kappa) = \boldsymbol{e}_{q+}^j e^{ik_{z,j}^q(z_j - z')} \tag{4.18}$$

$$\boldsymbol{E}_q^{\gamma}(z,\kappa) = \boldsymbol{e}_{q+}^{\gamma} e^{ik_{z,\gamma}^q(z - z_{\gamma-1})} \tag{4.19}$$

Eq. 4.18 represents right going wave originated from unit strength wave at $z'$and emerging from the boundary of the emitting slab ($z_j$, see Fig. 1). $\boldsymbol{E}_q^{\gamma}$ in Eq. 4.19 is the field of the right going wave originated from unit strength wave at $z_{\gamma-1}$ (the left boundary of slab $\gamma$) to $z$. Substituting Eqs. 4.18 and 4.19 into Eq. 4.17 results in the detailed expressions of the Weyl components, which are used to find the Poynting vector at an observation point $z$ due to radiation from the emitting slab by integrating $z'$ from $z_{j-1}$ to $z_j$ in Eq. 4.3. As an example, we list the detailed Weyl components for the electric and magnetic fields of the second scenario derived using Eq. 4.18 and 4.19.

$$g_{Exx}^{j\gamma} = \frac{i}{2}\frac{1}{k_{z,j}^{p}}\frac{k_{z,\gamma}^{p}}{k_\gamma}\frac{k_{z,j}^{p}}{k_j}\tau_{j+1\to m}^{p}T^{p}\tau_{m+1\to\gamma-1}^{p}\left\{e^{ik_{z,\gamma}^{p}(z-z_{\gamma-1})}\right\}e^{ik_{z,j}^{p}(z_j-z')} \tag{4.20}$$

$$g_{Exz}^{j\gamma} = -\frac{i}{2}\frac{1}{k_{z,j}^{p}}\frac{\varepsilon_\parallel}{\varepsilon_\perp}\frac{k_{z,\gamma}^{p}}{k_\gamma}\frac{\kappa}{k_j}\tau_{j+1\to m}^{p}T^{p}\tau_{m+1\to\gamma-1}^{p}\left\{e^{ik_{z,\gamma}^{p}(z-z_{\gamma-1})}\right\}e^{ik_{z,j}^{p}(z_j-z')} \tag{4.21}$$

$$g_{Eyy}^{j\gamma} = \frac{i}{2}\frac{1}{k_{z,j}^{s}}\tau_{j+1\to m}^{s}T^{s}\tau_{m+1\to\gamma-1}^{s}\left\{e^{ik_{z,\gamma}^{s}(z-z_{\gamma-1})}\right\}e^{ik_{z,j}^{s}(z_j-z')} \tag{4.22}$$

$$g_{Ezx}^{j\gamma} = -\frac{i}{2}\frac{1}{k_{z,j}^{p}}\frac{\varepsilon_\parallel}{\varepsilon_\perp}\frac{\kappa}{k_\gamma}\frac{k_{z,j}^{p}}{k_j}\tau_{j+1\to m}^{p}T^{p}\tau_{m+1\to\gamma-1}^{p}\left\{e^{ik_{z,\gamma}^{p}(z-z_{\gamma-1})}\right\}e^{ik_{z,j}^{p}(z_j-z')} \tag{4.23}$$

$$g_{Ezz}^{j\gamma} = \frac{i}{2}\frac{1}{k_{z,j}^{p}}\frac{\varepsilon_\parallel^2}{\varepsilon_\perp^2}\frac{\kappa^2}{k_\gamma k_j}\tau_{j+1\to m}^{p}T^{p}\tau_{m+1\to\gamma-1}^{p}\left\{e^{ik_{z,\gamma}^{p}(z-z_{\gamma-1})}\right\}e^{ik_{z,j}^{p}(z_j-z')} \tag{4.24}$$

Here, $k_{z,j}^{q}$ is out-of-plane component of wave vector in slab j for polarization q, and $k_j(=\sqrt{\varepsilon_\parallel}\frac{\omega}{c})$ is magnitude of wave vector in slab j. After evaluating $\nabla_r \times \overleftrightarrow{\boldsymbol{G}}^{E}$, we find magnetic field components from $\overleftrightarrow{\boldsymbol{G}}^{H}$ in the same form as Eq. S3:

$$g_{Hxy}^{j\gamma} = \frac{1}{2}\frac{1}{k_{z,j}^{s}}k_{z,\gamma}^{s}\tau_{j+1\to m}^{s}T^{s}\tau_{m+1\to\gamma-1}^{s}\left\{e^{ik_{z,\gamma}^{s}(z-z_{\gamma-1})}\right\}e^{ik_{z,j}^{s}(z_j-z')} \tag{4.25}$$

$$g_{Hzy}^{j\gamma} = -\frac{1}{2}\frac{1}{k_{z,j}^{s}}\kappa\tau_{j+1\to m}^{s}T^{s}\tau_{m+1\to\gamma-1}^{s}\left\{e^{ik_{z,\gamma}^{s}(z-z_{\gamma-1})}\right\}e^{ik_{z,j}^{s}(z_j-z')} \tag{4.26}$$

$$\begin{aligned} g_{Hyx}^{j\gamma} = -\frac{1}{2}\frac{1}{k_{z,j}^{p}}\frac{k_{z,j}^{p}}{k_\gamma k_j}\Big[&\left(k_{z,\gamma}^{p}\right)^2 \\ &+\frac{\varepsilon_\parallel}{\varepsilon_\perp}\kappa^2\Big]\tau_{j+1\to m}^{p}T^{p}\tau_{m+1\to\gamma-1}^{p}\left\{e^{ik_{z,\gamma}^{p}(z-z_{\gamma-1})}\right\}e^{ik_{z,j}^{p}(z_j-z')} \end{aligned} \tag{4.27}$$

$$\begin{aligned} g_{Hyz}^{j\gamma} = \frac{1}{2}\frac{1}{k_{z,j}^{p}}\frac{\kappa}{k_\gamma k_j}\frac{\varepsilon_\parallel}{\varepsilon_\perp}\Big[&\left(k_{z,\gamma}^{p}\right)^2 \\ &+\frac{\varepsilon_\parallel}{\varepsilon_\perp}\kappa^2\Big]\tau_{j+1\to m}^{p}T^{p}\tau_{m+1\to\gamma-1}^{p}\left\{e^{ik_{z,\gamma}^{p}(z-z_{\gamma-1})}\right\}e^{ik_{z,j}^{p}(z_j-z')} \end{aligned} \tag{4.28}$$

To find the radiative heat flux from the emitter $j$ to the receiver $\gamma$, we evaluate the difference in the Poynting vectors at the boundaries of slab $\gamma$, $z_{\gamma-1}$ and $z_\gamma$ which can be expressed in a compact form as:

$$q_{j\to\gamma} = \int \frac{d\omega}{2\pi}\left(\langle S_z(z_{\gamma-1},\omega)\rangle - \langle S_z(z_\gamma,\omega)\rangle\right) = \int \frac{d\omega}{2\pi}\Theta(\omega,T_j)\int_{\omega/c}^{\kappa_{max}} \frac{d\kappa}{2\pi}\kappa \sum_{i=s,p} \mathcal{T}_q^{j,\gamma} \qquad (4.29)$$

Similar to $\mathcal{T}_q^{1,2}$ in Eq. 4.1, we call $\mathcal{T}_q^{j,\gamma}$ energy exchange function. The final expression of $\mathcal{T}_q^{j,\gamma}$ for the second scenario is derived as:

$$\mathcal{T}_q^{j,\gamma} = \beta_q^j\left(1-e^{-2Im(k_{z,j}^q)\delta_j}\right)\left\{\left|\tau_{j+1\to m}^q\right|^2|T^q|^2\left|\tau_{m+1\to\gamma-1}^q\right|^2\right\}\left(1-e^{-2Im(k_{z,\gamma}^q)\delta_\gamma}\right)\beta_q^\gamma \qquad (4.30)$$

The expressions for the first and third scenarios are given as, respectively,:

$$\mathcal{T}^{j,\gamma} = \beta_q^j\left(1-e^{-2Im\left(k_{z,j}\right)\delta_j}\right)\left\{\left|\tau_{j+1\to\gamma-1}^q\right|^2 + \left|\tau_{j+1\to m}^q\right|^2(1-|T^q|^2)\left|\tau_{m\to\gamma+1}^q\right|^2\right\}\left(1 - e^{-2Im(k_{z,\gamma}^q)\delta_\gamma}\right)\beta_q^\gamma \qquad (4.31)$$

$$\mathcal{T}^{j,\gamma} = \beta_q^j\left(1-e^{-2Im(k_{z,j}^q)\delta_j}\right)\left\{\left|\tau_{j+1\to\gamma-1}^q\right|^2 + \left|\tau_{j-1\to m+1}^q\right|^2(1-|T^q|^2)\left|\tau_{m+1\to\gamma-1}^q\right|^2\right\}\left(1 - e^{-2Im(k_{z,\gamma}^q)\delta_\gamma}\right)\beta_q^\gamma \qquad (4.32)$$

Eq. 4.30, 4.31 and 4.32 are the central result of the derived many-body formalism. The energy exchange function, $\mathcal{T}_q^{j,\gamma}$, represents the interaction of the emitter and the receiver for a given mode. Similar to $\mathcal{T}$ in the two-body formalism, $\mathcal{T}_q^{j,\gamma} \leq 1$. Emission of waves from slab $j$ with thickness $\delta_j$ is given by $\beta_q^j\left(1-e^{-2Im(k_{z,j})\delta_j}\right)$. $\beta_q^j$ is related to the out-of-plane wave vector $k_z^q$ and is a constant in either medium 1 or 2 owing to continuous media. For p-polarized wave, For p-polarization, $\beta_p^j = Re\left(\varepsilon_\parallel k_{z,j}^{p,*}\right)/\left|\varepsilon_\parallel\right|\left|k_{z,j}^p\right|$, and for s-polarization $\beta_p^j = Re\left(k_{z,j}^p\right)/\left|k_{z,j}^p\right|$. The emitted waves interact with the receiver after transmitting through the slabs in medium 1, represented by $\left|\tau_{j+1\to m}^p\right|^2$ in Eq. 4.11, tunneling across the vacuum gap $|T^q|^2$, traversing through the slabs in medium 2 $\left|\tau_{m+1\to\gamma-1}^q\right|^2$ and reaching the receiver. During the interaction with the receiver, waves are absorbed as $\left(1-e^{-2Im(k_{z,\gamma}^q)\delta_\gamma}\right)\beta_q^\gamma$. $|T^q|^2$ represents the fraction of transmitted energy across the vacuum gap. It can be shown that $\beta_q|T^q|^2\beta_q$ has exactly the same expression as Eq. 4.2 for evanescent waves. We find $|T^q|^2$ from definition of $T^q$ as $\left|\frac{t_{m+}^q t_{m+1-}^q e^{ik_{z,o}d}}{1-r_m^q r_{m+1}^q e^{2ik_{z,o}d}}\right|^2$. Using Fresnel identities, it can be shown $\frac{Re\left(\varepsilon_\parallel k_{z,j}^{p,*}\right)}{|\varepsilon_\parallel|}\left|t_{m+}^p\right|^2 =$

$\frac{\left|k_{z,j}^{p}\right|^2}{\left|k_{z,o}\right|^2}\left[Re\left(k_{z,o}\right)\left(1-\left|r_m^p\right|^2\right)-2Im(k_{z,o})Im\left(r_m^p\right)\right]$ and $\frac{Re\left(\varepsilon_{\|}k_{z,j}^{p,*}\right)}{|\varepsilon_{\|}|}\left|t_{m-}^{p}\right|^2=Re\left(k_{z,o}\right)\left(1-\left|r_{m+1}^{p}\right|^2\right)+2Im(k_{z,o})Im\left(r_{m+1}^{p}\right)$. Then, $\beta_q|T^q|^2\beta_q$ becomes $\frac{1}{\left|k_{z,j}\right|^2}\frac{\left\{\left|k_{z,j}^{p}\right|^2/|k_{z,o}|^2\left[Re\left(k_{z,o}\right)\left(1-|r_m^p|^2\right)-2Im(k_{z,o})Im\left(r_m^p\right)\right]\right\}\left\{Re\left(k_{z,o}\right)\left(1-|r_{m+1}^p|^2\right)-2Im(k_{z,o})Im\left(r_{m+1}^p\right)\right\}e^{-2Im(k_{z,o})d}}{\left|1-r_m^p r_{m+1}^p e^{2ik_{z,o}d}\right|^2}$.

$k_{z,o}$ takes the form either $Im(k_{z,o})$ or $Re\left(k_{z,o}\right)$ depending on if the wave in vacuum is evanescent or propagating. In our case, evanescent waves are the main contributor to energy transport across the vacuum gap. Thus, $Re\left(k_{z,o}\right)=0$ and $\left|k_{z,o}\right|^2=Im\left(k_{z,o}\right)^2$. This leads to $\beta_q|T^q|^2\beta_q=\frac{\{4Im(r_m^p)Im(r_{m+1}^p)\}e^{-2Im(k_{z,o})d}}{\left|1-r_m^p r_{m+1}^p e^{2ik_{z,o}d}\right|^2}$. Since $r_m^p=r_1^p$ and $r_{m+1}^p=r_2^p$, the final expression of $\beta_q|T^q|^2\beta_q$ becomes Eq. 2. The same procedure for s-polarization also returns Eq. 2, although its contribution is small. Lastly, it can be shown that the energy exchange function obeys reciprocity, i.e. $\mathcal{T}^{j,\gamma}=\mathcal{T}^{\gamma,j}$. Therefore, the expressions are valid when the emitter is located to the right of the receiver.

Now, net radiative heat exchange between two slabs, $j$ and $\gamma$ can be expressed as

$$q_{j,\gamma}=q_{j\to\gamma}-q_{\gamma\to j}=\int\frac{d\omega}{2\pi}\left[\Theta\left(\omega,T_j\right)-\Theta\left(\omega,T_\gamma\right)\right]\int_{\frac{\omega}{c}}^{\kappa_{max}}\frac{d\kappa}{2\pi}\kappa\,\mathcal{T}_q^{j,\gamma} \tag{4.33}$$

and the net radiative heat transfer into slab $j$, $q^j$, by summation over all slabs as

$$q^j=-\sum_{l\neq j}^{N}q_{j,l}=\sum_{l\neq j}^{N}q_{l,j}=\int\frac{d\omega}{2\pi}\sum_{l\neq j}^{N}\left[\Theta(\omega,T_l)-\Theta\left(\omega,T_j\right)\right]\int_{\frac{\omega}{c}}^{\kappa_{max}}\frac{d\kappa}{2\pi}\kappa\,\mathcal{T}_q^{l,j} \tag{4.34}$$

Equation 4.34 has a similar form as Eq. 4.1. To solve for the radiative heat transfer for given reservoir temperatures, we find the set of net radiative heat transfer $(q^1,q^2,\dots,q^N)$ and a temperature profile that yields $q^j=0$ for the entire set except reservoirs (which can be done using an iterative procedure), then the global system reaches global equilibrium. The corresponding temperature profile in the media is unique to the state and is the global equilibrium temperature profile. In the computed set, $q^1(=-q^N)$ represents the net radiative heat transfer between the hot and cold media, which is also the near-field radiative transfer between the two media.

## 4.2 Many-body vs. Two-body Formalism

Derived above to the situation when the medium on each side of the gap has a uniform temperature, the many-body formalism is applied. All slabs in hot and cold media are at their reservoir temperatures, $T_H$ and $T_C$. From Eq. 4.33, it is seen that for slabs in the same medium, $q_{j,\gamma} = 0$. Thus, the net radiation is only transferred between slabs in separate media. To find net heat transfer from slab j in medium 1 to the entire medium 2, $\sum_{\gamma=m+1}^{N} q_{j,\gamma} = q_{j,cold}$ is calculated. The net heat transfer from medium 1 to 2 is obtained by summing the net heat transfers, $q_{j,cold}$, for all slabs in medium 1, $q_{1,2} = \sum_{j=1}^{m} q_{j,cold} = \sum_{j=1}^{m}\sum_{\gamma=m+1}^{N} q_{j,\gamma}$. Owing to the uniform temperatures, the summation only needs to be applied to $\mathcal{T}_q^{j,\gamma}$, i.e., $\sum_{j=1}^{m}\sum_{\gamma=m+1}^{N}\mathcal{T}_q^{j,\gamma}$. Here, $\mathcal{T}_q^{j,\gamma}$ is expressed as Eq. 4.30 for the scenario that the two slabs are on different sides of the vacuum separation. The inner summation over $\gamma$ for multiplication of $\left|\tau_{m+1\to\gamma}^{q}\right|^2$ with $\left(1 - e^{-2Im(k_{z,\gamma}^{q})\delta_\gamma}\right)$ in Eq. 4.30 yields 1. Similarly, the outer summation over $j$ for multiplication of $\left|\tau_{j+1\to m}^{q}\right|^2$ with $\left(1 - e^{-2Im(k_{z,j}^{q})\delta_j}\right)$ also results in 1. Hence, the summations reduce $\mathcal{T}_q^{j,\gamma}$ to $\beta_q|T^q|^2\beta_q$, which is the same expression as the energy exchange function between two slabs with uniform temperature and is the same expression as Eq. 4.2 as indicated in Section 4.1. Therefore, the final result is the exact result of the two-body formalism. This shows the two-body formalism with uniform temperatures is simply a special case of the many-body formalism.

The many-body model reducing to the two-body model under uniform temperature condition indicates that the two formalisms consider phonon polaritons with the same origin for near-field radiative transfer, which depends on the probability of phonon polaritons tunneling across the vacuum gap. Although the two-body formalism is sometimes equivalated using a surface treatment[29], it in fact does not distinguish the origin of radiation. At uniform temperature, radiation is also generated from the bulk, but a wave removes a net amount of heat only when crossing the surface, whereas there is no net radiation exchange within each body with a uniform temperature. On the other hand, the many-body formalism accounts for the net radiation exchange via phonon polaritons within the same medium, as well as their contribution to the near-field radiative transfer across the gap.

## 4.3 Near-field Radiation Driven by Temperature Gradient

Here, the results of near-field radiative heat flux using the many-body approach is presented. To generate results, a global system of 250-nm thick hexagonal boron nitride (hBN) films in contact with reservoirs at $T_H$ = 330 K and $T_C$ = 300 K is selected. Figure 4.2a shows the net radiative heat transfer, $q_{NF}$, from the hot to the cold medium with respect to $d$. The net radiative heat transfer increases with the decrease in $d$ that allows HPhPs with larger wave vectors tunneling across the vacuum gap as seen from $e^{-2Im(k_{z,o})d}$ in Eq. 4.2. Figure 4.2a also shows the net radiative heat transfer, $q_{NF}$, calculated using the two-body formalism when hot and cold media are set at reservoir temperatures, 330 K and 300 K. $q_{NF}$ for two-body and many-body approaches almost overlap for separations greater than 5 nm. This is because the temperatures are nearly uniform for the many-body formalism when the separation is large. Figure 4.2b shows the temperature distributions in the hot medium for $d$ = 10 nm, 5 nm, 2 nm, and 1 nm. The temperature profile or gradient is similar in the cold medium. For $d$ = 5 nm and above, where $q_{NF}$s overlap in Figure 4.2a, the temperature is nearly uniform. Note that the near-field radiation heat transfer is much greater than that of blackbody, which is ~210 $Wm^{-2}$ between two surfaces at the same temperatures. Figure 2a also shows $q_{NF}$ from the many-body approach is less than that obtained using the two-body approach. This is because HPhP modes tunneling across the vacuum gap remove heat from the bulk, which leads to the temperature gradient and lower temperatures near the interface in the hot medium and higher temperature in the cold medium, resulting in a less amount of heat exchange.

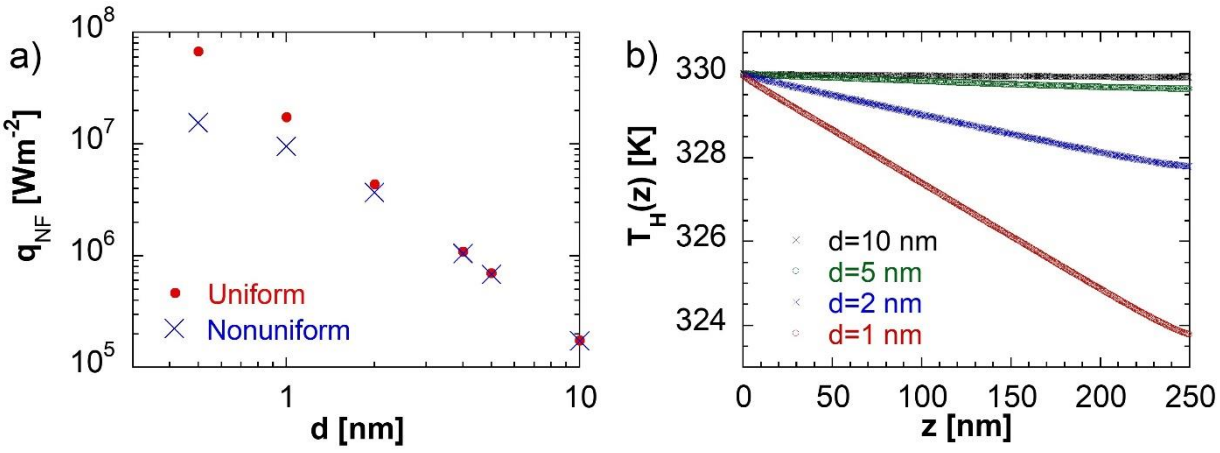


Figure 4.2. a) Radiative heat transfer from the hot to cold medium with respect to vacuum separation for uniform and nonuniform temperature conditions. Results overlap for separation gaps greater than 5 nm. b) The temperature profile across hot medium for $d$ = 10 nm, 5 nm, 2 nm, and 1 nm. Slab thickness throught this study is 0.5 nm.

Now, discussion in details on propagations of phonon polaritons driven by the temperature gradient across the vacuum gap takes place. For this purpose, consider a pair of slabs, with one in the hot medium and the other in the cold medium, each is positioned 5 nm away from the vacuum-material interface. Figure 4.3a shows the heat transfer coefficient or the coupling strength between the pair of slabs, defined as $h_{j,\gamma} = \frac{q_{j,\gamma}}{T_j - T_\gamma}$, for different vacuum separations. The coupling between the slabs increases when the two media are brought closer. This is explained by the wave vector dependent coupling strength shown in Figure 4.3b. When the separation is decreased, the range of $\kappa$ for tunneling polaritons increases. However, there is also a limit or cutoff for $\kappa$ for each separation distance which is governed by the exponential decay in Eq. 4.2. This cutoff corresponds to $\kappa \sim (2d)^{-1}$, which is equivalent to total internal reflection. In addition to the increasing in range, the strength of coupling also increases when the gap is reduced due to the less attenuation of energy carried by a given wave vector across the gap as seen in Figure 4.3b. When we compare coupling strengths for a given wave vector at different vacuum gaps, we also see the coupling strength enhances at shorter gap distances, which arises from less attenuation across the vacuum gap. Summation of $h_{j,\gamma}$ over $j$ and $\gamma$, $\sum_{j=1}^{m} \sum_{\gamma=m+1}^{N} h_{j,\gamma}$, results in total heat transfer coefficient, $h_{hot,cold}$, between hot and cold media and is shown as a function of gap size in Figure 3c. Comparison of Figure 4.3a and 4.3c reveals similar trends of $h_{j,\gamma}$ and

$h_{hot,cold}$ for the corresponding gap sizes. It is also shown the wave vector dependent total heat transfer coefficient, $h_{hot,cold,\kappa}$, in Figure 4.3d. The trend of $h_{hot,cold,\kappa}$ is similar to that of $h_{j,\gamma,\kappa}$ in Figure 4.3b for the corresponding gaps size due to cutoff of wave vectors corresponding to the gap size.

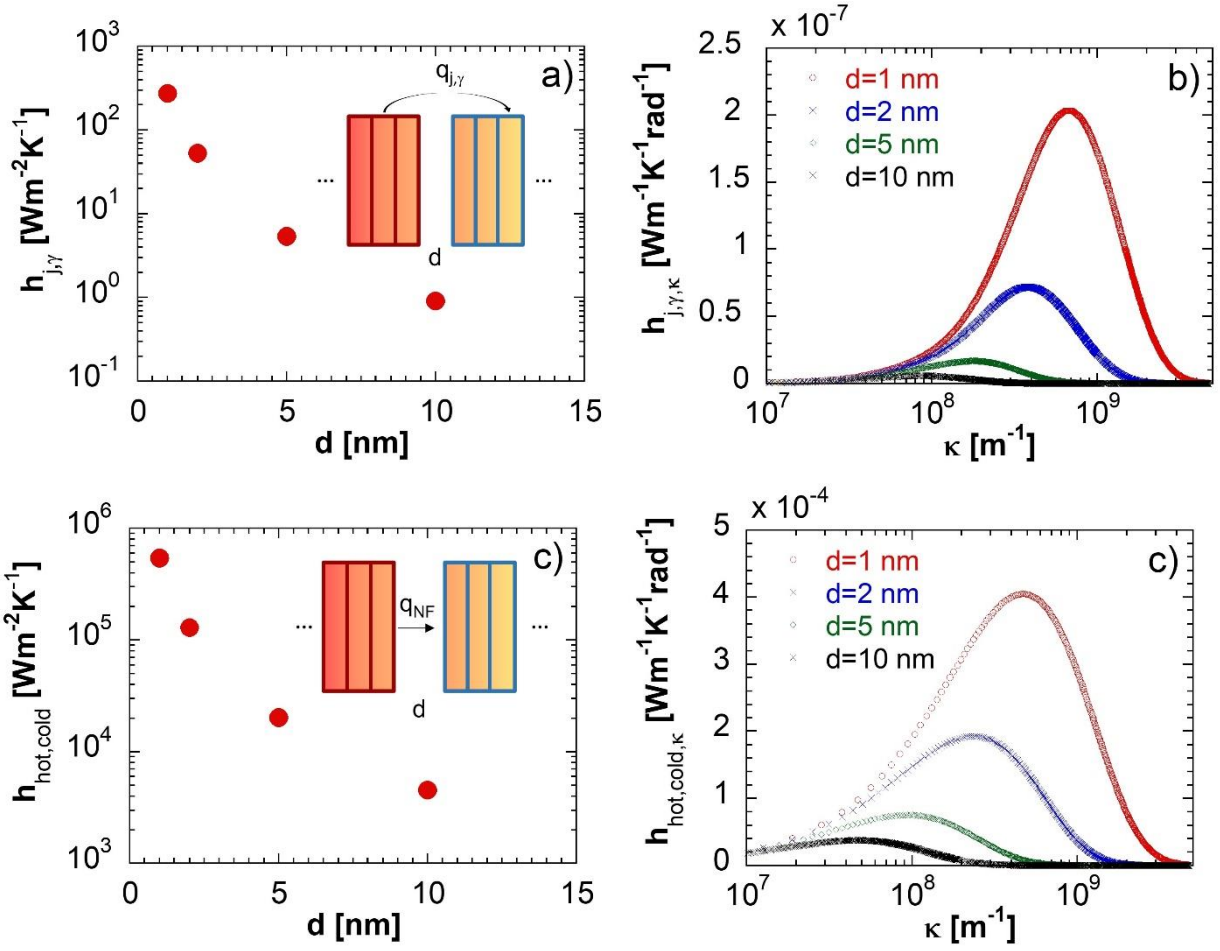


Figure 4.3. a) Heat transfer coefficient, as a measure of coupling strength, between two slabs located 5 nm away from the vacuum-material interface at opposite sides of the vacuum separation as a function of gap size. The slab thickness used for the calculations is 0.5 nm. b) Wave vector dependent heat transfer coefficient for the corresponding gap sizes. c) Total heat transfer coefficient between hot and cold media as a function of gap size. d) Wave vector dependent total heat transfer coefficient between two media for the corresponding gap sizes.

Slabs near the interface have a stronger interaction with the medium across the vacuum gap than those farther away from the interface. To account for interaction, the following expression is calculated: $h_{j,cold} = \sum_{\gamma=m+1}^{N} h_{j,\gamma}$ where $h_{j,cold}$represents the coupling strength of slab j in the hot

medium with the entire cold medium. Figure 4 shows $h_{j,cold}$ for all the slabs in the hot medium as a function of position of the slabs from the reservoir ($z$ = 0 nm) for d = 10 nm, 5 nm, 2 nm and 1 nm. It is seen each individual slab contributes to the net radiative heat transfer from the hot to the cold medium. This is another indication that the origin of near-field heat transfer between hot and cold media is HPhPs generated within the bulk, even though the contribution by a slab decreases with distance away from the interface by orders of magnitude due to the short propagation lengths of the highly confined modes that contribute most to the near-field radiation transfer. Figure 4 also shows that $h_{j,cold}$ increases with the decrease in the vacuum gap for all slabs due to less attenuation of the modes across the vacuum gap with shorter separation.

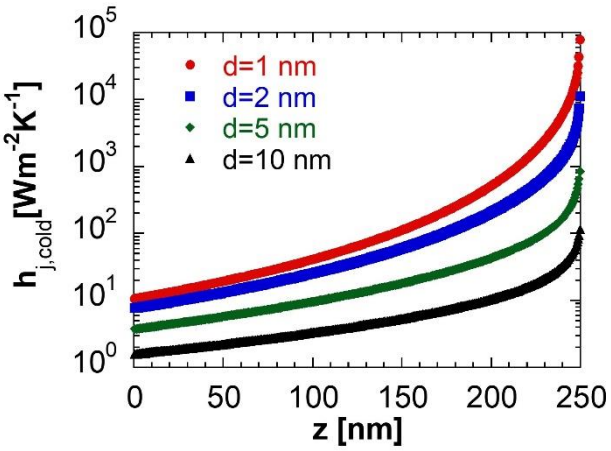


Figure 4.4. Heat transfer coefficient of individual slabs with a thickness of 0.5 nm in the hot medium arising from interaction of the slab with the entire cold medium at vacuum separation of 1 nm, 5 nm, and 10 nm.

Lastly, it is noted that this study considers only radiative transport as the heat transfer mechanism. Conduction also transports energy within a material. The many-body model can incorporate conduction during the temperature calculation and solve for local thermal equilibrium temperature by applying energy balance to each slab [114]. Additionally, conductive heat transfer across the vacuum gap can take place for sub-nm separations through phonon tunneling [84], [86], [115], [116]. Even we have computed the near-field radiation effect with a separation below 1 nm (Figure. 4.2a), at that small gap phonon tunneling will likely need to be considered which will be the subject of another study.

## 4.4 Summary

With the study in this chapter, it is found that HPhPs responsible for energy transport across the vacuum gap between hyperbolic materials are bulk-originated polaritons. At uniform temperatures, the many-body approach that accounts for bulk-originated polaritons reduces to the two-body formalism, indicating the near-field radiative transfer described by the two-body formalism is just a special case of the many-body approach. When a temperature gradient exists in the media, HPhPs transfer net heat through the material as well as across the vacuum gap. Energy transfer across the vacuum gap is largely due to HPhPs with large wave vectors, which contribute even more to the enhanced near-field radiative transfer when the gap is reduced.

# 5. ENERGY TRANSPORT BY RADIATION IN HYPERBOLIC MATERIALS

This chapter has been partially reproduced from a previous publication*: Salihoglu, H.; Iyer, V.; Taniguchi, T.; Watanabe, K.; Ye, P.; Xu, X. Energy Transport by Radiation in Hyperbolic Material Comparable to Conduction. Adv. Funct. Mat.* ***2020****, 30(6), 6-11.*

In solids, it has been understood that the primary energy carriers are phonons and electrons. Another energy carrier, photons, has been treated as a surface phenomenon, and as such, its contribution to energy transfer inside a material is negligible. However, the role of photons in thermal transport is also originated from the bulk. Rytov's seminal work employed the fluctuation dissipation theorem (FDT) to link thermal fluctuations in a material with the generated electromagnetic energy, which enables prediction of radiative emission from the material in equilibrium [8]. Recently, the extent of FDT was mainly expanded for near-field radiation arising from evanescent waves or resonant surface waves [6], [25], [27], [28], [38], [76], [117]. The much enhanced thermal radiation in extreme near-field implies strong electromagnetic interactions in the bulk, and is predicted by FDT well [97].

In nonequilibrium condition, temperature gradient in hBN drives energy transport by thermal radiation. Derived for equilibrium condition, FDT in this study is employed to estimate radiative heat transfer in hBN. With this aim, a many-body method is developed and exploited. We also explain the far-field reflection measurement of hBN at 300 K, 400 K, 500 K and 600 K. It is conducted to derive the fitting parameters given in Table 1.3.

Under temperature gradient, polaritons transport energy in $\alpha$–$MoO_3$, biaxial material, too. To account for radiative heat transfer by polaritons in all three axes, the many-body approach applied to the global system with vacuum separation given in Chapter 4 is modified and implemented. Our analysis explains temperature dependent thermal conductivity with unusual trend.

## 5.1 Radiative Transfer inside hBN

In this section, we explain many-body model derived to account for radiative transfer in hBN and interpret theoretical and experimental results.

### 5.1.1 Reflection spectra of hBN over a temperature range of 300 K to 600 K

Since no data for dielectric properties of hBN over a temperature range of 300 K to 600 K is available in literature, we measure far-field reflection spectrum of hBN thin film to extract dielectric properties of hBN at various temperatures. We followed the procedure: Nexus 670 FTIR Bench with a Continuum Microscope is used to collect reflection spectra of ~ 1 μm thick hBN on bulk $CaF_2$. Sample was placed on a Linkam THMS720 heating stage to control its temperature. After temperature stabilization, reflected light collected by a 15x objective lens was averaged over 64 scans. Figure 5.1A shows the experimental reflectance spectrum. The calculated reflectance results using temperature dependent dielectric constants are shown in Figure 5.1B. Measurement is repeated to ensure the repeatability of data. The Lorentz model with one oscillator for both components of dielectric permittivity agrees with the temperature dependent reflection data. We use least-square fitting to extract parameters. Γ is the most sensitive parameter to fitting in Reststrahlen bands. This parameter also governs the calculated $k_{rad}$. There is up to 20% of uncertainty in fitting of Γ, giving rise to an uncertainty in the calculated $k_{rad}$ of about 10% - 20% for temperatures from 300 K to 600 K. Figure 5.1C demonstrates the fitting results with ±20% uncertainty in Γ at 500 K. For precise value of Γ, the best fitting is applied to experimental results of the Type-II Reststrahlen band ($2.58\times10^{14} < w < 3.03\times10^{14}$ rad/s). Figure 5.1D also shows the best fit. It is noteworthy that even though FTIR bench was purged, the sample was exposed to the ambient air. Thus, C-O absorption corresponding to the frequency range over majority of the Type-II Reststrahlen band skews the results, and leads to the mentioned uncertainty. Note that with increasing temperature, C-O absorption becomes more prominent. The fitting parameters of 300 K are in good agreement with literature [118], and all parameters are listed in Table 1.3. In addition, for $CaF_2$, wavelength-independent dielectric properties (2, *i*0.02) are used.

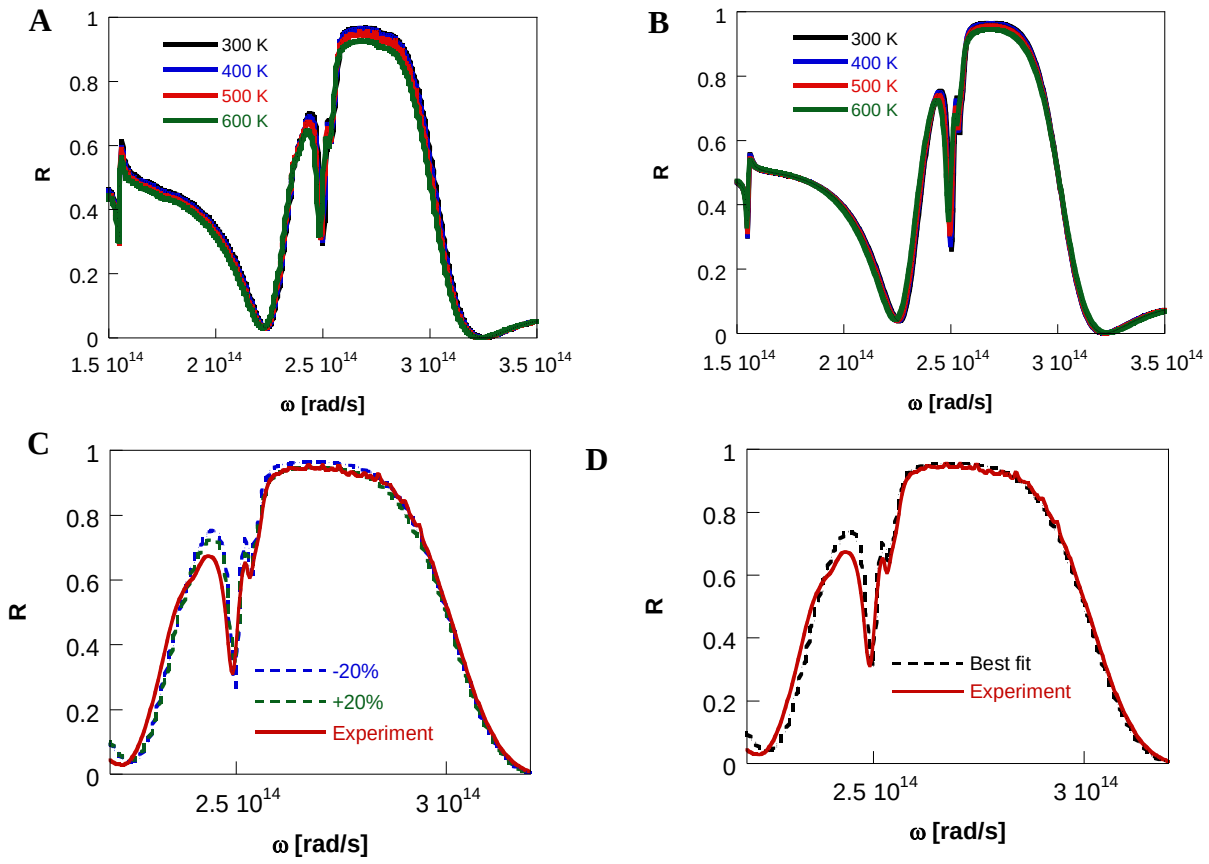


Figure 5.1. Experimental vs. fitted reflection. A) Temperature dependent experimental reflection spectra from hBN thin film. B) Calculated reflection spectra. C) Effect of the fitting values on the calculated reflection spectrum at 500 K. As blue dashed line represents the calculated reflection spectra when $\Gamma_{\parallel} = \Gamma_{\parallel,Best} + 0.2\Gamma_{\parallel,Best}$, green dashed line is for the calculated reflection spectra when $\Gamma_{\parallel} = \Gamma_{\parallel,Best} - 0.2\Gamma_{\parallel,Best}$, where $\Gamma_{\parallel,Best}$ is the best fitting value for losses in in-plane direction at 500 K given in Table 1.3. D) Best-fitting result is shown.

### 5.1.2 Many-body model to calculate radiative heat transfer in hBN

For a system under out-of-equilibrium condition, we develop a model. Our microscopic many-body model consists of a continuous medium, under investigation, sandwiched by two heat baths (Figure 5.2A). The medium is divided into many bodies (slabs) in the z-direction (out-of-plane) and extending to infinity in x- and y- directions. Each slab is assumed in local thermal equilibrium at a local temperature, hence correlation of the generated fields at an interface, let's say $\gamma$ as in Figure 5.2B, generated by each slab, let's say $l$ as in Figure 5.2B, due to thermal radiation is calculated by plugging Eq. 1.8 and Green's functions into Eq. 1.7. The generated

field interacts with all slabs along the path from the slab *l* to the interface γ, and this interaction is accounted by Green's functions. As given in Eq. 1.9 for a flat interface, Green's function from a source to generated field at an interface is derived for the many-body system by tracing the generated field from its source, and the tracing is repeated for all the generated fields at the interface from all sources in the system separately. The derivation is cumbersome, but can be found in [119]. Contribution of all slabs to the generated fields at the interface is summed up and plugged into energy flux:

$$\langle S \rangle = Re(\boldsymbol{E} \times \boldsymbol{H}) \tag{5.1}$$

Note that the summation of the contributions from all slabs is possible with the help of the continuous energy flux owing to the continuity of tangential components of *E* and *H* throughout the system. The contribution from all slabs yields the radiative heat flux at interface $\gamma$, $\Phi_\gamma$, given as [119]:

$$\Phi_\gamma = \int_0^\infty \frac{d\omega}{2\pi} \int_0^{\kappa_{max}} \frac{d\kappa}{2\pi} \kappa \sum_{s,p} \sum_{l}^{N} \mathcal{N}_l \hat{\mathcal{T}}_\gamma^l \tag{5.2}$$

where $\mathcal{N}$ and $\hat{\mathcal{T}}$ are mean thermal energy of an oscillator, $\hbar\omega n(\omega, T$ as used in Eq. 1.2. and transmission function to interface $\gamma$ from the source in slab *l*, respectively. Eq. 5.2 computes contributions of all slabs in the system to the radiative heat flux at interface $\gamma$. The transmission function ($\hat{T}_\gamma^l$) accounts for the radiation emitted by slab *l* and reaching out the interface $\gamma$ after interacting all slabs between the slab and the interface. The general form of the transmission function is derived using the scattering-matrix method and is expressed as [119]:

$$\begin{aligned}
\hat{\mathcal{T}}_\gamma^j = \prod^{pw} \Bigg[ & \frac{\left|\tau^{j+1\to\gamma}\right|^2 \left(1 - \left|\rho_+^{-1\to j}\right|^2\right)}{\left|1 - \rho_+^{0\to j}\rho_-^{j+1\to\gamma}\right|^2} \\
& - \frac{\left|\tau^{j\to\gamma}\right|^2 \left(1 - \left|\rho_+^{-1\to j-1}\right|^2\right)}{\left|1 - \rho_+^{-1\to j-1}\rho_-^{j\to\gamma}\right|^2} \Bigg] \frac{1 - \left|\rho_+^{-1\to j-1}\right|^2}{\left|1 - \rho_+^{0\to\gamma}\rho_-^{\gamma+1\to N+1}\right|^2} \\
+ \prod^{ew} \Bigg[ & \frac{\left|\tau^{j+1\to\gamma}\right|^2 \mathrm{Im}(\rho_+^{-1\to j})}{\left|1 - \rho_+^{0\to j}\rho_-^{j+1\to\gamma}\right|^2} \\
& - \frac{\left|\tau^{j\to\gamma}\right|^2 \mathrm{Im}(\rho_+^{-1\to j-1})}{\left|1 - \rho_+^{-1\to j-1}\rho_-^{j\to\gamma}\right|^2} \Bigg] \frac{4\mathrm{Im}(\rho_-^{\gamma+1\to N+1})}{\left|1 - \rho_+^{0\to\gamma}\rho_-^{\gamma+1\to N+1}\right|^2}
\end{aligned} \tag{5.3}$$

Here, $\tau^{j\to\gamma}$ is the transmission coefficient through slabs from *j* to $\gamma$, and the explicit expression is given in the next paragraph. $\prod^{pw}$ and $\prod^{ew}$ are propagating and evanescent waves defined using

the Heaviside step function $\mathcal{H}(\omega - c\kappa)$ and $\mathcal{H}(c\kappa - \omega)$, respectively. $\rho_{+/-}^{j\to\gamma}$ is the reflection coefficient of a block consisting of slabs from $j$ to $\gamma$ (left $-$, right $+$). In our case, the evanescent field contribution can be neglected since only the propagating waves contribute to radiation. We set all reflection coefficients to zero because of continuous medium. Eq. 5.3 then simplifies to:

$$\hat{\mathcal{T}}_{\gamma}^{j} = (1 - |\tau_j|^2)|\tau^{j+1\to\gamma}|^2 \tag{5.4}$$

This is the simplified transmission function used in our study.

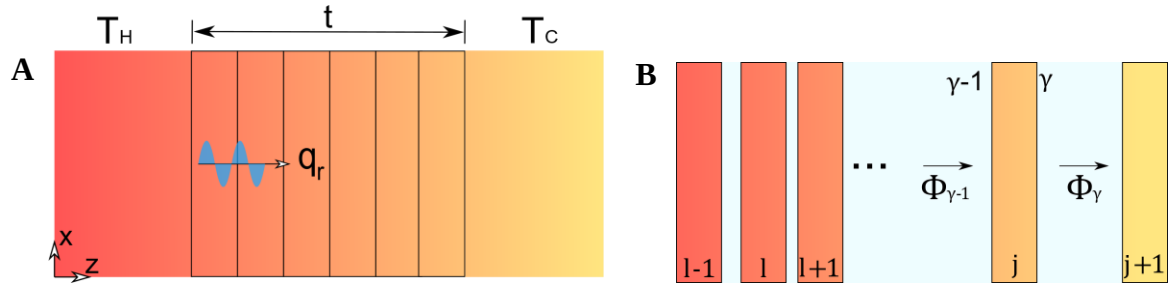


Figure 5.2. Microscale many-body model. A) Schematic of the radiative heat transfer problem under investigation. Combination of slabs forms continuous medium. The medium is in contact with two heat baths of prescribed temperatures, $T_H$ and $T_C$. B) Control volume around single slab $j$ and energy transfer. $\Phi_{\gamma-1}$ and $\Phi_{\gamma}$ are evaluated at interfaces $\gamma - 1$ and $\gamma$, respectively. $\Phi_{\gamma-1} = \Phi_{\gamma}$ represents local thermal equilibrium condition for the single slab. Slab $l$ contains the source contributing to the thermal radiation at interface where $\Phi$ is evaluated. Summation over l in Eq. 4.5 ensures the contribution of all slabs in the system.

To compute the net radiative heat transfer into slab $j$, $\Phi^j$, we apply energy balance equation to the slab. Figure 5.2B illustrates that $\Phi_{\gamma-1}$ and $\Phi_{\gamma}$ represent the heat flux received by and removed from the slab $j$, respectively. Then, we can write $\Phi^j = \Phi_{\gamma-1} - \Phi_{\gamma}$. Evaluating Eq. 5.2 for the interfaces $\gamma - 1$ and $\gamma$ enables to calculate $\Phi^j$. The final form as a result of algebraic manipulations casts into the formula expressed in a Landauer-like form as [119]:

$$\Phi^j = \Phi_{\gamma-1} - \Phi_{\gamma} = \int_0^{\infty} \frac{d\omega}{2\pi} \int_0^{\kappa_{max}} \frac{d\kappa}{2\pi} \kappa \sum_{s,p} \sum_{l=0}^{N} \Theta_{l,j} \mathcal{T}^{l,j} \tag{5.5}$$

where $\omega$, $\kappa$, $s$, and $p$ are frequency, wavenumber, and TE and TM polarizations, respectively. $\Theta_{l,j}$ represents the difference in mean energy of oscillators generated in slabs $l$ and $j$ $(\Theta_{l,j} = \mathcal{N}_l - \mathcal{N}_j)$. The energy exchange function, $\mathcal{T}^{l,j}$, accounts for energy exchange between slabs $l$ and $j$.

Using Eq. 5.4 for $\hat{\mathcal{J}}_{j-1}^{l}$ and $\hat{\mathcal{J}}_{j}^{l}$,the energy exchange function ($\mathcal{T}^{l,j}$) between slabs *l* and *j* can be written as:

$$\mathcal{T}^{l,j} = \hat{\mathcal{J}}_{j-1}^{l} - \hat{\mathcal{J}}_{j}^{l} = (1 - |\tau_l|^2)\left|\tau^{l+1\to j-1}\right|^2(1 - \left|\tau_j\right|^2) \tag{5.6}$$

The transmission coefficient, $\tau_j$, describing transmission through single slab j, is given in general form as [20]:

$$\tau_j = \frac{(1 - r_j^2)e^{ik_{z,j}\delta_j}}{1 - r_j^2 e^{2ik_{z,j}\delta_j}} \tag{5.7}$$

where $\delta_j$ is thickness of slab *j* and $k_{z,i}$ is out-of-plane component of wavevector expressed as $\sqrt{\varepsilon_{\parallel}\omega^2/c^2 - \varepsilon_{\parallel}/\varepsilon_{\perp}\,\kappa^2}$ ($\sqrt{\varepsilon_{\parallel}\omega^2/c^2 - \kappa^2}$) for p(s)-polarized waves. $r_j$ is the Fresnel's reflection coefficient for interface between vacuum and slab and is zero in continuous medium. Then, Eq. 4.7 reads $\tau_j = e^{ik_{z,j}\delta_j}$ by setting $r_j$=0. $\tau^{l+1\to j-1}$ in Eq. 5.6 is the transmission coefficient through slabs from $l+1$ to $j-1$, which is $\tau^{l+1\to j-1} = \tau_{l+1} \ldots \tau_{j-1}$. Inserting $\tau_j$ into $\tau^{l+1\to j-1}$ yields $\tau^{l+1\to j-1} = e^{i\sum_{m=j-1}^{j-1} k_{z,m}\delta_m}$. The sum over *l* in Eq. 5.5 guarantees to account the energy exchange between the slab *j* and all the remaining slabs in the system arising from the energy difference, $\Theta_{l,j}$, between the slabs, *l* and *j*.

To explain Eq. 5.6, the term $1 - |\tau_l|^2$ on the right hand side can be considered as an emission coefficient of slab *l*, and the term $1 - \left|\tau_j\right|^2$ is an absorption coefficient. This satisfies the Kirchoff's Law because emission $(1 - |\tau_l|^2)$ by slab *l* equals absorption$(1 - \left|\tau_j\right|^2)$ by slab *j* in the same medium. The transmission coefficient of heat baths ($\tau_0$ and $\tau_N$) is zero as boundary conditions, hence semi-infinite heat baths generate and absorb all modes.

To obtain temperature profile of the medium with temperature gradient, we should solve Eq. 5.5. It is solved to obtain an energy balance condition for each slab: $\Phi_{\gamma-1} = \Phi_{\gamma}$. Hence, the total radiative heat transfer is simply $\Phi_{\gamma}$. An initial temperature distribution is first assumed, and $\Phi^j$ are computed. Calculations are iterated until $\Phi^j = 0$ ($\Phi_{\gamma-1} = \Phi_{\gamma}$) is satisfied for each slab, and then a temperature distribution in the medium is also obtained. The obtained temperature profile corresponds to the temperatures of the slabs at local equilibrium. Local equilibrium of the slabs in the system also guarantees energy balance (steady-state) condition. This means the

energy removed from the hot bath is equal to the energy received by the cold bath due to energy balance of the system at global equilibrium. Besides, the number of iterations depends on two factors: the number of slabs and temperature range. The number of slabs increases the number of the iterations necessary for equilibrium condition because, physically, the system reaches the equilibrium condition slower due to higher internal energy requirement. As for the second criteria, increase in temperature results in the larger number of iterations. At higher temperatures, loss increases. Consequently, the transported energy along the system decreases, and the propagation of energy slows down, meaning that solution of the equilibrium temperature profile needs a larger number of iterations. Total energy of the system, in turn transported energy, enhances with temperature as well. This also increases the number of the iterations to find the equilibrium condition. By considering these two factors and the energy balance conditions, we determine the total number of iterations at several temperatures and distances.

We compute spectral radiative heat transfer using the method developed and compare the result with the conventional blackbody theory. We consider a problem consisting of two blackbodies at 300 K with a temperature difference of 1 K ($T_H = 301$ K and $T_C = 300$ K) and separated by vacuum. Note that we only calculate contribution of propagating modes to radiative heat transfer in our model. Figure 5.3 demonstrates both results of our model and the blackbody theory. For the problem under consideration, the blackbody theory over the frequency range in Figure 5.3 indicates a total radiative heat transfer as 5.673 W/m$^2$ whereas our calculation results in 5.677 W/m$^2$.

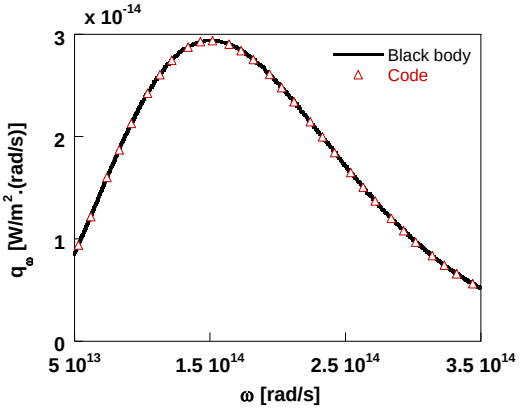


Figure 5.3. Validation of the calculation method against blackbody radiation. The result computed with our method is in good agreement with the results calculated using the blackbody theory.

The equations derived in this work, Eq. 5.2 and 5.5, can also be reduced to the blackbody expression in hyperbolic materials given by [120]:

$$\Phi = \int_0^\infty \frac{d\omega}{2\pi}[\Theta(\omega, T_H) - \Theta(\omega, T_C)] \sum_{s,p} \int_\kappa \frac{d\kappa}{2\pi} \kappa \tag{5.8}$$

This blackbody expression considers dispersive and non-dissipative hyperbolic materials and is derived for two hyperbolic blackbodies at temperatures $T_H$ and $T_C$ separated by a lossless hyperbolic medium. To compare Eq. 5.5 with Eq. 5.8, we apply the same dispersive and non-dissipative conditions. In this case, only the energy exchange function between the hot and cold baths, $\mathcal{T}^{0,N}$, survives, and $\mathcal{T}^{l,j}$ for intermediate slabs is zero because of $\tau_l = \tau_j = 1$ (since $\kappa^{"} = 0$ in the transmission coefficients). Consequently, Eq. 5.5 takes the exact form of Eq. 5.8. Thus, Eq. 5.5 expresses a general form of blackbody radiation in a material with losses.

### 5.1.3 Thickness and temperature dependent transmission functions

We first look at the transmission coefficient $\tau$. Figure 5.4A, B and C illustrate transmission coefficients with respect to frequency and wave vector for p-polarized waves (phonon-polaritons) traveling a distance $d$ = 10 nm, 100 nm, and 10 μm, respectively. The majority of phonon-polaritons with very high wave vectors (here defined as $\kappa > 10^8$ m$^{-1}$, thus $\lambda<10$ nm) carry energy over a distance of about 10 nm without significant loss (Figure 5.4A); however, these carriers lose over 80% of their energies over a distance of 100 nm because of the exponential decay $e^{-2\kappa^{"}d}$ (Figure 5.4B). For phonon-polaritons with wave vectors in the range $10^7 < \kappa < \sim 10^8$ m$^{-1}$ (defined as high-κ phonon-polaritons here, corresponding to $100 > \lambda > 10$ nm), travelling a distance greater than 1 μm nulls their contribution (Figure 5.4B). For phonon-polaritons with even smaller $\kappa$ values ($\kappa \sim 10^6$ m$^{-1}$, thus $\lambda\sim1$ μm), its decay distance is about of 10 μm (Figure 5.4C).

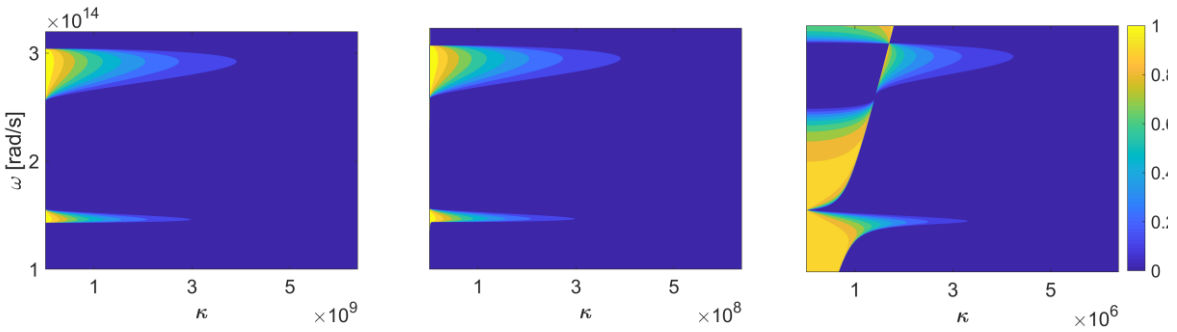


Figure 5.4. Transmission coefficients of p-polarized waves traveling A) 10 nm, B) 100 nm, and C) 10 um. Scales and ranges of the y-axis for (A) to **(**C) are the same. Both high-κ ( $10^7 < \kappa < 10^8$ $m^{-1}$) and very high-κ ($\kappa \sim \pi/a > 10^8$ $m^{-1}$) modes transfer energy in 10 nm, whereas very high-κ modes mostly attenuate over a thickness of about 100 nm. Red dashed line in (C) corresponds to the modes with $\kappa \sim n\omega/c$.

Using the temperature dependent dielectric properties derived using the fitting parameters given in Table 1.3, the transmission coefficient $\tau^{l \to j}$ at elevated temperatures is calculated. Figure 5.5A shows the transmission coefficient through a 200 nm-thick hBN at room temperature. Increasing temperature to 400 K (Figure 5.5B) and 500 K (Figure 4.5C) reduced the propagation length because of increasing loss at higher temperatures. Despite the temperature dependency of dielectric properties, phonon polaritons at elevated temperatures transport energy approximately over the similar distance as those at room temperature (Figure 5.5).

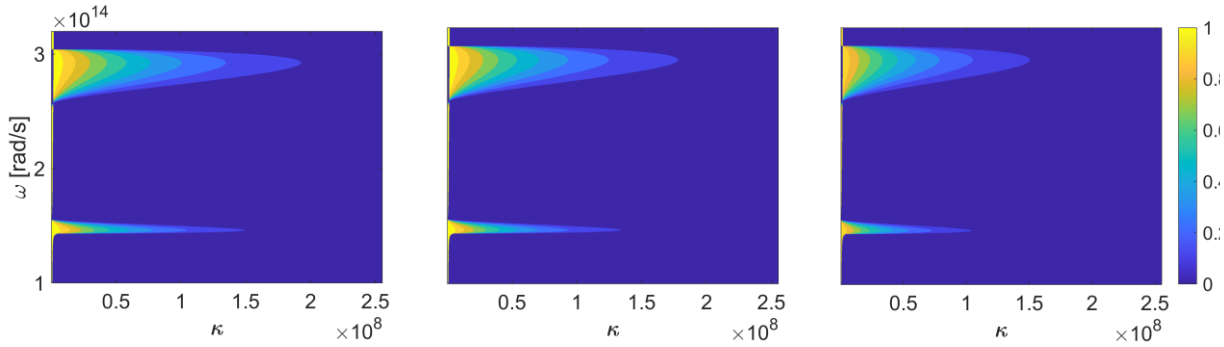


Figure 5.5. Transmission coefficient of traversing 200 nm in hBN at A) 300 K, B) 400 K, and C) 500 K. Despite higher losses in the material with temperature increase, the range of modes contributing energy transfer over the distance remains almost the same.

### 5.1.4 Spectral and total radiative heat transfer

We next examine spectral radiative heat transfer across the medium at room temperature (300 K). A 1 K temperature difference between the heat baths is imposed to drive radiative heat transfer in hBN. Figure 5.6A shows the spectral radiative heat transfer which has two characteristic peaks in the Reststrahlen bands, arising from the available large number of modes and resulting in super-Planckian emission. Phonon-polaritons transport energy via all transport channels (modes) at frequencies inside Reststrahlen bands, producing six orders of magnitude higher radiative transport compared to that outside Reststrahlen bands. The reason that the spectral radiation outside Reststrahlen bands exceeds that of blackbody in vacuum (Figure 5.6A) is due to the higher index of refraction of hBN than vacuum (n > 1).

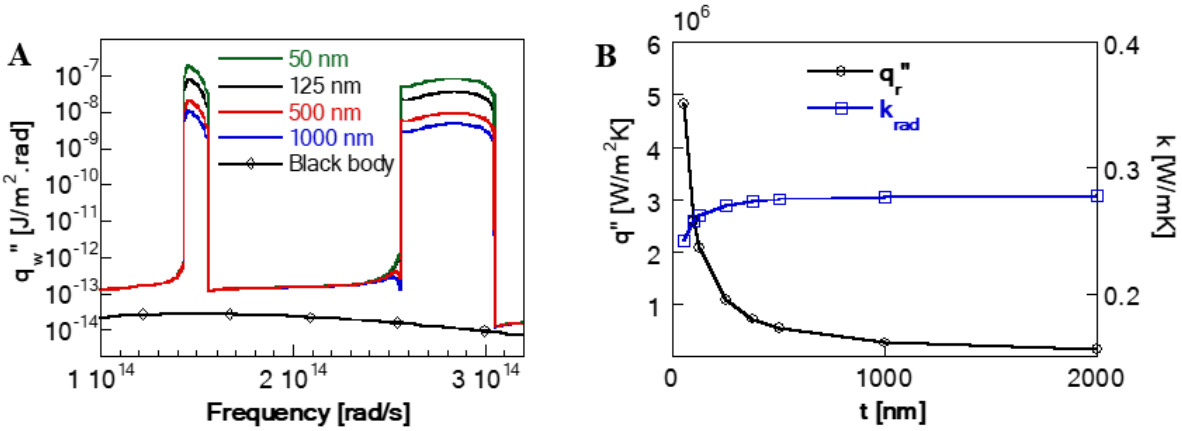


Figure 5.6. Spectral and total radiative heat transfer with respect to thickness. A) Spectral radiation transfer in hBN with 1 K temperature difference between heat baths. The enhancement within the Reststrahlen bands clearly demonstrates contributions of phonon polariton modes. B) Total radiation and radiative thermal conductivity at various thicknesses. The contribution of very high-κ modes to radiative transport decreases with thickness due to losses in thicker films.

We further analyze contributions of all modes over the entire frequency range, the total radiative heat transfer. The total radiative heat transfer depends on the material's thickness, as suggested by the previous analysis on the dependence of transmission coefficient of phonon polariton modes on thickness. Figure 5.6B shows that the total radiative heat transfer decreases with thickness. Here, the density of modes as a function of wave vector plays the key role. The greatest contribution to total radiative heat transfer in short distances comes from very high-κ phonon-polaritons as the high density of energy channels (modes) for very high-κ phonon-

polaritons enables energy transport with a large number of energy carriers. However, the energy carried by these modes dissipates rapidly over short distances as seen in the spectral analysis. As the distance increases, less carriers contribute to transferring energy, leading to a decrease in total heat transfer.

### 5.1.5 Radiative thermal conductivity

We can also define a radiative thermal conductivity based on the Fourier's Law, i.e., $k_{rad} = q_r'' t/\Delta T$, where $q_r''$ is the total radiative heat transfer, $t$ is the thickness, and $\Delta T$ is the temperature difference of the two heat baths. Figure 5.6B indicates that $k_{rad}$ increases with $t$ and approaches a constant value ~ 500 nm. In thin hBN, $k_{rad}$ increases with thickness since the number of energy carrier that vanishes due to dissipation is less than that excited by adding more materials to the medium as the thickness increases. The conductivity reaches a constant value at the thickness ~500 nm as the number of disappeared carrier and that of the added carrier reaches a balance.

We calculated the temperature-dependent radiative thermal conductivity by raising the temperatures of the thermal baths, but maintained the temperature difference at 1 K. Figure 5.7A shows radiative thermal conductivity increases with temperature. Raising the temperature excites a larger number of energy states and also shifts thermal energy peak (hyperbolic blackbody radiation) towards higher frequencies according to the Wien's displacement law.

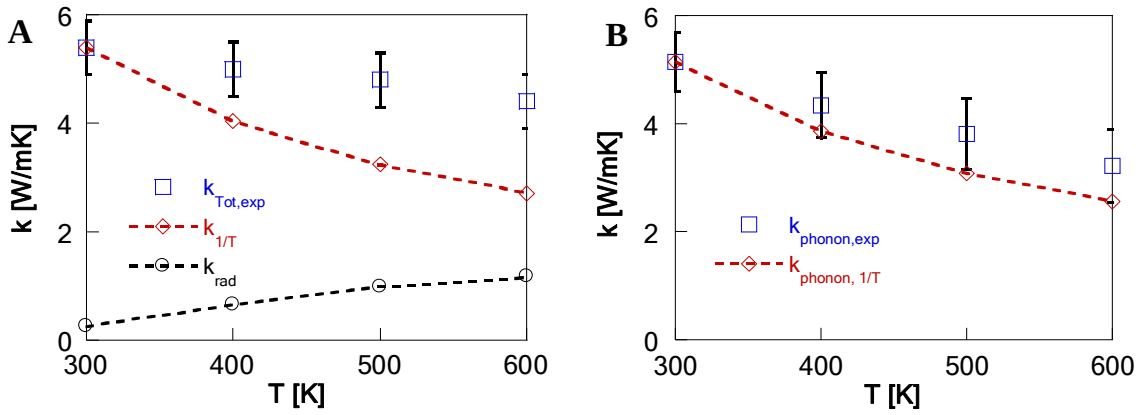


Figure 5.7. Radiative thermal conductivity. A) Radiative thermal conductivity $k_{rad}$ and measured total thermal conductivity ($k_{Tot,exp}$) with respect to temperature. The total thermal conductivity consists of both photonic and phononic contributions, and does not follow the normal 1/T dependence of phonon conductivity (red dashed line). B) Experimental phonon thermal conductivity $k_{Phonon,exp}$ obtained by subtracting $k_{rad}$ from $k_{Tot,exp}$ and comparison to the 1/T dependence of phonon conductivity.

***Experiment to measure out-of-plane thermal conductivity***

The out-of-plane (in the direction perpendicular to the thin film) total thermal conductivity in hBN thin films is measured in the temperature range from 300 K to 600 K . Sample used in the experiment is prepared in the following way: Ultrapure h-BN films were exfoliated a few times with Nitto dicing tape and subsequently transferred onto a thermal release tape (Nitto), which was adhered to the silicon substrate. The tape was release by heating the substrate to 120 ˚C to obtain clean and high yield transfer of h-BN films with various thicknesses. Within a few hours of exfoliation, 110 nm gold was deposited on the entire sample using e-beam evaporation for thermal conductivity measurement. The sample was cleaned with toluene, acetone and IPA just before the gold deposition. AFM (NIST-NT) scans were performed after gold deposition to precisely determine the film thicknesses.

Thermal conductivity was measured with a home-built nanosecond thermoreflectance setup [121] and performed by Vasudevan Iyer. The sample is pumped to higher temperature ($T_{excess}$< ~10 K ) with a 6.4 ns, 5 kHz pulsed laser (Spectra Physics) operating at 532 nm wavelength. The change in surface temperature is measured with a CW He-Ne probe laser beam coupled to a balanced fast photodiode (Thorlabs PDB130A), and directly recorded on a high speed

oscilloscope (Tektronix TDS744A) set to AC coupling mode averaging 10,000 acquisitions. The pump beam is expanded to a 164 μm $1/e^2$ diameter to minimize in-plane heat diffusion. The probe spot is 20 μm in diameter. The sample is mounted on a heating stage (Linkam THMS 720) and annealed at 600 K for one hour before performing temperature dependent measurements. The measurements were repeated several times to ensure reproducibility.

To extract the out-of-plane (total) thermal conductivity, a 2D axi-symmetric simulation was performed using COMSOL to solve the heat diffusion equation, taking into account the contact resistance between gold and h-BN and between h-BN and silicon. The literature value of in-plane thermal conductivity was used [122] and a parametric sweep was performed to obtain best fit for out-of-plane thermal conductivity. Fitting for 1,030 nm thick film at 300 K is shown in Figure 5.8, which yielded an out-of-plane thermal conductivity of 5.4 W/m·K. The uncertainty is about 0.5 W/m·K, obtained from 25% higher than the best fit $R^2$ value. The large in-plane thermal conductivity of hBN warrants the use of a large pump spot to ensure minimum contribution from lateral heat spreading. A laser spot size of 164 μm diameter was used to ensure this, and the effect of small pump spot of 20 μm diameter (simulated) shows the effect of in-pane heat diffusion as seen in Figure 5.8.

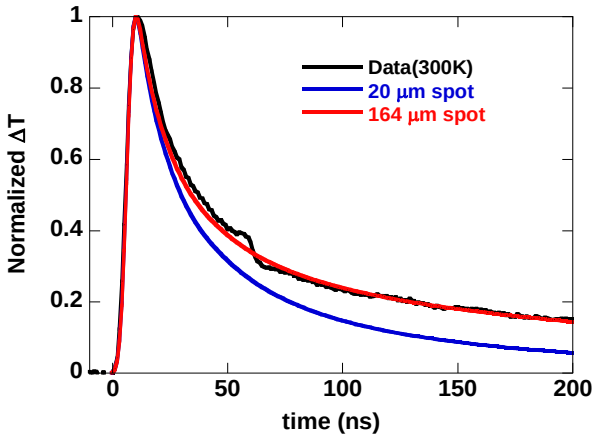


Figure 5.8. Fitting of 1030 nm film data at 300 K with COMSOL simulation to extract out-of-plane thermal conductivity. For a small simulated pump spot size of 20 μm diameter, the effect of in-plane heat diffusion is clearly visible by the faster decay. The fitting is less sensitive to spot size for large spot sizes. The experimental laser spot size is 164 μm diameter, for which the in-plane thermal conductivity contribution is minimal.

The data for several films in the 700 to 1200 nm range (shown in Figure 5.9) was collected at each temperature, i.e. 300 K to 600 K. The COMSOL fitting was performed on these films and the obtained out-of-plane thermal conductivities were within a 0.2 W/m·K range of variation, less than the measurement uncertainty. This is consistent with our calculation that radiation thermal conductivity reaches a constant value when the thickness is greater than ~ 500 nm. From the fitting, the contact resistances between gold and hBN are in the $3 \times 10^{-8}$ to $6x10^{-8}$ $m^2$ K $W^{-1}$ range for different films and temperatures, slightly decreasing with increasing temperature. The fitting is rather insensitive to contact resistance between hBN and silicon substrate and a value of $3 \times 10^{-8}$ was used. Unfortunately, it was not able to determine thermal conductivity of thinner films accurately, as the data fitting is much influenced by the contact resistance between the gold and the hBN film and the contact resistance between hBN film and the substrate. Figure 5.10 shows the large uncertainties of the fitted thermal conductivity data for thinner films. The upper bound of the thermal conductivity goes higher for thinner films (no upper bound for the two thinnest films) since the contact resistances become comparable with or greater than the resistance of thinner films with larger thermal conductivity.

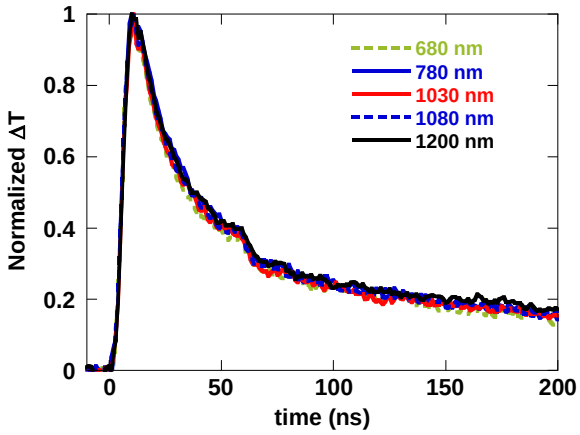


Figure 5.9. Transient reflectivity measured at 400 K on five films of 680, 780, 1030, 1080 and 1200 nm thickness.

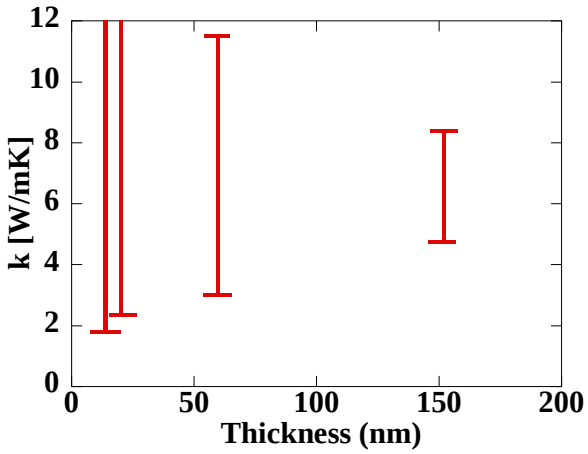


Figure 5.10. Fitting of 300 K data for thin flakes. The uncertainty becomes larger as the film thickness is reduced due to contact resistances dominating the heat flow.

The procedure explained above is used to measure out-of-plane thermal conductivity. The measured thermal conductivity, $k_{Tot,exp}$, contains both photonic (phonon polariton modes) and phononic contributions, and is shown in Figure 5.7A for a 1030 nm thick hBN film. We can see that there is a decrease of the measured total thermal conductivity from 300 K to 600 K. However, this decrease is much slower than the 1/T dependence for phonon transport alone, which suggests a temperature dependent phonon-polariton radiative contribution. We calculate the difference between the calculated radiation thermal conductivity $k_{rad}$ and the experimentally determined $k_{Tot,exp}$, which yields the experimental phonon conductivity, $k_{Phonon,exp}$, as shown in Figure 5.7B. The resulting $k_{Phonon,exp}$ follows a much closer 1/T trend of phonon conductivity, which will be further discussed below.

We notice a large contribution of radiative thermal transport as the temperature increases, from ~ 5% at 300 K to ~ 27% at 600 K. The increase of radiative thermal conductivity with temperature originates from the increased contribution of thermally excited phonon-polaritons in the Reststrahlen band. The peak radiation at 300 K is at a frequency around ~10 μm (~$1.9 \times 10^{14}$ rad $s^{-1}$), which is below the lower bound of the Reststrahlen band ($2.5 \times 10^{14}$ rad $s^{-1}$). Increasing temperature increases populated photon states with thermal energy inside the Reststrahlen band. At 400 K, the peak radiation moves into the Reststrahlen band, and at higher temperatures, it moves toward the upper bound of the Reststrahlen band ($3 \times 10^{14}$ rad $s^{-1}$). Moreover, the

radiative thermal conductivity increases due to higher energy carried by the phonon-polariton at higher temperature.

We now discuss the small deviation of the extracted $k_{Phonon,exp}$ vs. the expected 1/T phonon conductivity. This can be a result of experimental uncertainties, as indicated in the error bars of the measured total thermal conductivity which is about +/-0.5 W $m^{-1}$ $K^{-1}$. Computation of radiative thermal conductivity uses dielectric constants, which were also measured experimentally using FTIR). We estimate that the uncertainty in dielectric constant measurement can contribute up to 20% of uncertainty in the calculated radiative thermal conductivity (Section 4.1). Given these considerations, the extracted $k_{Phonon,exp}$ is in a reasonable agreement with the expected 1/T trend. On the other hand, we also notice a recent study on the out-of-plane thermal conductivity of hBN which showed that thermal conductivity does not follow 1/T in a temperature range between over 100 K to 400 K [122]. This deviation was attributed to the contribution of high frequency acoustic phonons which do not follow the 1/T trend at temperatures below 400 K. At temperatures above 400 K, however, contribute of high frequency phonons also decreases with temperature, resulting in ~ 1/T trend in phonon thermal conductivity.

Lastly, we emphasize the contribution of high-κ phonon-polariton modes to radiative thermal transport. Phonon polaritons and phonons in hyperbolic material coexist and both contribute to energy transport. In a normal material, the spherical or ellipsoidal κ-space contour limits the wave vector, and the modes with wave vectors greater than that of the light cone do not propagate, i.e. Planckian emission. On the other hand, in the Reststrahlen bands of HMs, the hyperboloidal κ-space which is a result of opposite signs of the dielectric constants along the principal directions, allows propagations of phonon-polaritons with wave vectors larger than the light cone, resulting in super-Planckian emission, as large as $\kappa \sim 1/a$, where a is the characteristic length of the material. The number of modes with wave vectors larger than the light cone is very large in the Reststrahlen bands. Various studies [81], [123], [124] also suggested that integration of wave vector should be cut off at $\kappa \sim 1/a$. Hence, high-κ phonon-polariton modes in bulk are responsible for the rise of the notable radiative contribution.

## 5.2 Radiative Transfer inside $MoO_3$

Here, we discuss our theoretical results for radiative thermal conductivity in MoO3 in three principal axis. As different from the model derived for hBN in Section 5.1, the many body-formalism used for $MoO_3$ is extended from the many-body approach explained in Chapter 4.

### 5.2.1 Radiative heat transfer equation and Dispersion relation for $MoO_3$

To account for radiative heat transfer in α–$MoO_3$, we exploit the macroscopic many-body approach using the fluctuation-dissipation theorem and the green's function method, as discussed in derived in Chapter 4. Figure 1 shows a continuous biaxial medium between hot and cold baths at temperature $T_H$ and $T_C$, respectively. The z-axis shows the out-of-plane direction, and *x* and *y* are in-plane directions. The medium expands to infinity in in-plane directions and experiences temperature variation along the z-axis. Each slab, *j*, is assumed at a local equilibrium temperature, $T_j$. The radiative heat transfer into slab *j*, $\Phi^j$, as a result of interaction with all slabs in a system with two uniaxial materials has been derived [114]. Here, we extend its use to biaxial material by rearranging the integration over in-plane components ($k_x$, $k_y$) of wavevector as (see Supplementary Document for details):

$$\Phi^j = \Phi_{j-1} - \Phi_j = \int_0^\infty \frac{d\omega}{2\pi} \int_0^{k_{x,m}} \int_0^{k_{y,m}} \frac{dk_x}{\pi} \frac{dk_y}{\pi} \sum_{l \neq j}^{N} \hbar\omega n_{l,j} \mathcal{T}^{l,j} \tag{5.9}$$

Here, $\omega$ is frequency of a mode, $\hbar$ is reduced Planck's constant. Inner double integration is over x-, $k_x$, and y-, $k_y$, component of wavevector. $\Phi_j(\Phi_{j-1})$ is radiative thermal energy flux at the boundary between slabs *j* and *j*+1 (*j*−1 and *j*). $n_{l,j}$ is the difference of finding a state occupied by a mode generated at temperature of slab *l*, $T_l$, and slab *j*, $T_j$. Summation over *l* adds up radiative contribution arising from interaction of slab *j* with all other slabs in the N-body system. The energy exchange function, $\mathcal{T}^{l,j}$, defines interaction strength of slabs *l* and *j* and plays key role in heat transfer analysis. Derived for many-body system with a vacuum separation [125], the function simplifies to the following expression in our case:

$$\mathcal{T}^{l,j} = \chi^j \left(1 - e^{-2Im(k_z)\delta_j}\right) \left|\tau_{j+1 \to l-1}\right|^2 \left(1 - e^{-2Im(k_z)\delta_l}\right) \chi^l \tag{5.10}$$

To simplify the expression in Eq. 4.30 to Eq. 5.10, we set $T^q = 1$ in Eq. 4.30. In Eq. 5.10, $\chi^j$ determines propagation condition of modes, in turn energy carrying modes. With regards the simplification of the expression in Eq. 4.30, we assume $\chi^j = k_z'/|k_z|$ for both s- and p-

polarizations. $\tau_{j+1\to l-1}$ is transmission function through slabs $j$+1 to $l$−1 and given as $e^{i2k_z(\delta_{j+1}+\cdots+\delta_{l-1})}$ where $\delta_i$ represents thickness of slab $i$. $\mathcal{T}^{l,j}$ is valid for waves generated by the source slab $j$ located to the left of the receiver slab $l$. We note that the exchange function satisfies reciprocity, $\mathcal{T}^{l,j} = \mathcal{T}^{j,l}$, and can be explained in the following way: polariton emitted by slab $j$ with a probability of $\beta^j\left(1 - e^{-2k_z''\delta_j}\right)$, traverses through intermediate slabs, $\left|\tau_{j+1\to l-1}\right|^2$, and is absorbed by slab $l$ with a probability of $\left(1 - e^{-2k_z''\delta_l}\right)\beta^l$. We note the Kirchhoff's law is applicable because the emission probability is equal to absorption probability. Here, $k_z''$ is imaginary part of wavevector component along the z-axis, $k_z(= k_z' + ik_z'')$. In a bulk biaxial material with diagonal dielectric tensor in the given coordinates, $k_z$ is obtained by solving a biquadratic equation [64]. The discussion of the solutions for $k_z$ is given in Section 5.2.2. In Eq. 5.9, the upper limit of integral over $k_x$ and $k_y$ determines the maximum wavevector, $k_{x,m}\sim\pi/a$ and $k_{y,m}\sim\pi/b$, of the mode excited by thermal radiation with minimum spatial correlation length [83] defined by lattice constants of a = 0.396 nm and b = 0.370 nm [126] at x- and y-axes, respectively. To find radiative heat flowing through the system, we solve Eq. 5.8 iteratively for all intermediate slabs until $\Phi_{j-1} = \Phi_j$ which indicates the local thermal equilibrium condition of any slab $j$. The temperature distribution obtained is the solution, and $\Phi_j$ yields total radiative heat flux, $q_z''$.

By applying temperature gradient in the x- (y-) axis and assuming uniform temperature in the z-axis, we also compute radiative heat transfer in the x- (y-) axis, $q_{r,x}''$ ($q_{r,y}''$). To find complex wavevector in the direction temperature gradient, quadratic dispersion equation is solved for $k_x$ ($k_y$) after replacing $k_z$ and $\varepsilon_z$ with $k_x$ ($k_y$) and $\varepsilon_x$ ($\varepsilon_y$) for $q_x''$ ($q_y''$) calculation (See Supplementary Document for details). In addition, integration limit over $k_x$ ($k_y$) becomes over $k_z$, and $\mathcal{T}^{l,j}$ in Eq. 1 is calculated using $k_x$ ($k_y$). Finally, the iterative calculation explained above is repeated to solve for the temperature profile in x- (y-) axis.

### 5.2.2 Proper solutions of propagating waves in $MoO_3$

For discussion of solutions of the equation, we recall Eq. 1.21-1.24. Eq. 1.21 yields four complex solutions of $k_z$ ($k_{z,1}$, $k_{z,2}$, $k_{z,3}$, $k_{z,4}$), corresponding to two extraordinary waves going to the +z direction (right) and two extraordinary waves going to the −z direction (left). In Eq. 1.24, the discriminant $\Delta = A^2 - 4B. \neq 0$ and is complex. We present it using its modulus, *R*, and its principal argument, ν. Then, $\Delta = Re^{iv}$ where $R = |A^2 - 4B|$ and $-\pi < v \leq \pi$. To avoid ambiguity in solutions, we use the principal value to produce solutions. Then, from Eq. 1.24, $k_{z,1}^2$ and $k_{z,2}^2$ become:

$$k_{z,1}^2 = -\frac{A}{2} + \frac{R^{1/2}e^{iv/2}}{2} \tag{5.11}$$

$$k_{z,2}^2 = -\frac{A}{2} - \frac{R^{1/2}e^{iv/2}}{2} \tag{5.12}$$

Hence, the four solutions of Eq. 1.5 for biaxial material take the following forms:

$$k_{z,1} = \sqrt{-\frac{A}{2} + \frac{R^{1/2}e^{iv/2}}{2}} = -k_{z,3} \tag{5.13}$$

$$k_{z,2} = \sqrt{-\frac{A}{2} - \frac{R^{1/2}e^{iv/2}}{2}} = -k_{z,4} \tag{5.14}$$

One pair, $k_{z,1}$ and $k_{z,3}$, represents one type of waves, the other pair, $k_{z,2}$ and $k_{z,4}$, represents second type of waves, called a and b waves, or fast and slow waves. Both fast and slow waves are extraordinary waves because their Poynting's vector points to a direction different from phase propagation direction. These two forms of waves exist over entire frequency region. Outside RS bands, we call them ordinary waves in the main text. Inside RS bands, one component of the dielectric property has negative value, and dispersion relation supports existence of high-k modes, polaritons. We note that polaritons exist in the slow wave form. For right going waves, solutions with $k_z'' > 0$ are selected because, with definition ($e^{ik_z z}$) of the electric field, waves with $k_z'' > 0$ vanishes when z→+∞.

### 5.2.3 Modes propagating and contributing to energy transport in $MoO_3$

$\chi$ in the energy exchange function determines propagation condition of a mode in a given wavevector region. In Figure 5.11, we plot absolute value of $\chi$ for three frequencies from separate RS bands as a function of $k_x$ and $k_y$. We observe in Figure 5.11a and b that $\chi$ ~1 within a conic region (bright yellow region). In these regions, dispersion relation dictates that $k_z' >> k_z''$, and this indicates that, when excited, these modes propagate over a distance longer than its wavelength ( $\lambda \sim 1/k_z'$) with relatively weak attenuation in the material (attenuation distance or penetration depth ~ 1/ $k_z''$). These modes are hyperbolic phonon polaritons. In Figure 5.11c, $\chi \sim 1$ over entire $k_x$ and $k_y$ range. Thus, hyperbolic polariton modes exist and are supported. On the other hand, in Figure 5.11a and b, $\chi$ < 0.1 outside the conic region in which modes are highly damped and vanish in distances shorter than its wavelength. Thus, these modes are not supported in the material (no electromagnetic wave form, i.e. polaritons).

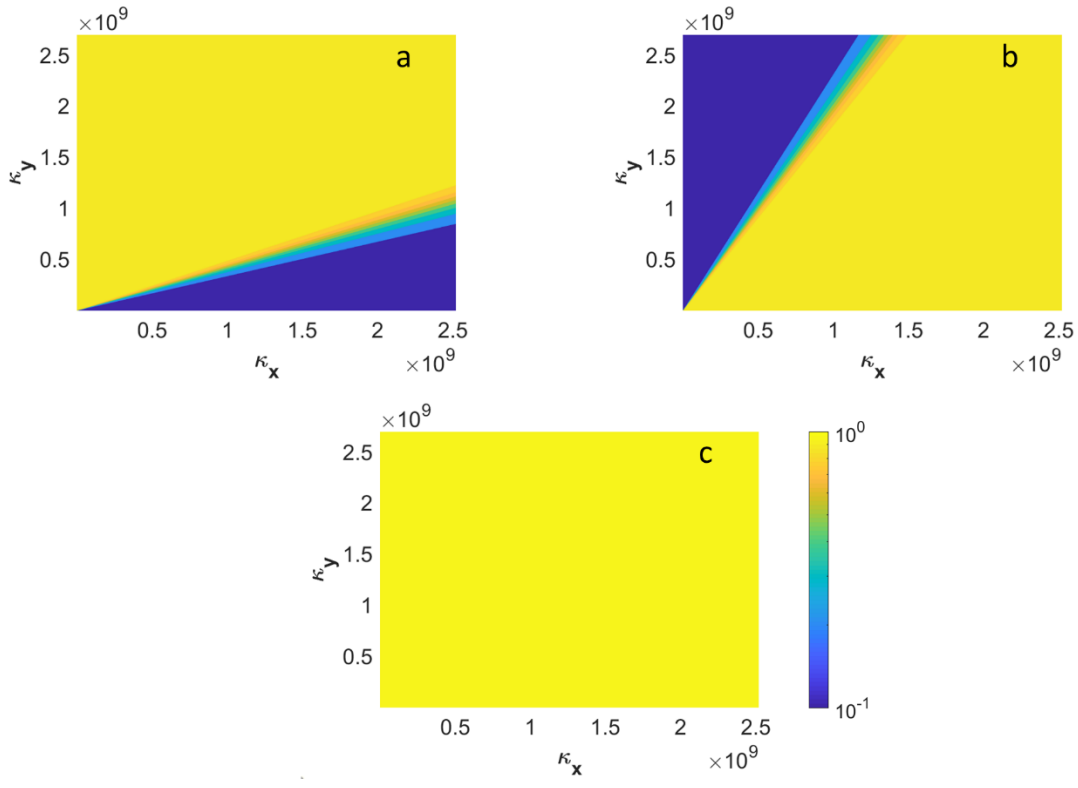


Figure 5.11. Absolute value of $\chi$ as a function of $k_x$ and $k_y$ at A) ω = 1.12 × $10^{14}$ ($\varepsilon_x$ = 7.55, $\varepsilon_y$ = −38.3, $\varepsilon_z$ = 5.25) B) ω = 1.70 × $10^{14}$ ($\varepsilon_x$ = −4.15, $\varepsilon_y$ = 1.11, $\varepsilon_z$ = 9.02) and C) ω = 1.84 × $10^{14}$ ($\varepsilon_x$ = 0.52, $\varepsilon_y$ = 2.13, $\varepsilon_z$ = −7.20). Absolute values are plotted because *Re($k_z$)* in A and B are negative.

To understand energy transport of the supported and unsupported modes, we analyze energy exchange function, $\mathcal{T}$, in Eq. 5.9. We select the frequency ($\omega = 1.70 \times 10^{14}$ rad/s) used for Figure 5.11b and plot $\mathcal{T}^{l,j}$ for two baths ($l$=1 and $j$=N) sandwiching the intermediate medium with a thickness of $t$ = 15 nm, 25 nm and 50 nm in Figure 5.12a-c. At a glance, we see that wavevector region of modes with $\mathcal{T}$ greater than 0.1 coincides with that of the hyperbolic phonon polariton modes shown in Figure 5.11b, indicating that polaritons transport energy. We also recognize for all three cases that $\mathcal{T}$ of the polaritons increases with smaller $k_x$-$k_y$ values. The reason lies in that, for high-k modes, $k_z$ value of polaritons has about the same order with their $k_x$-$k_y$ values and decreases/increases proportional to the $k_x$-$k_y$ values. Thus, polaritons with smaller $k_x$-$k_y$ dissipate less along a given distance due to smaller $k_z''$ (longer penetration depth) and carry more energy (greater $\mathcal{T}$). In addition, Figure 3a-c show that wavevector region of the polaritons carrying considerable energy ($\mathcal{T} > 0.1$) is bounded. Outer boundary of the wavevector region depends on penetration depth, in turn $k_z''$, of the energy carrying polaritons. For instance, polaritons with wavevector beyond the outer bound dissipate its total energy in t = 15 nm (Figure 5.12a) because penetration depth of these polaritons is shorter than $t$. Inside the wavevector region, polaritons have penetration depth longer than $t$ and carry considerable energy, resulting in $\mathcal{T} > 0.1$. Furthermore, from comparison of Figure 5.12a-c, we deduce that the wavevector region shrinks with increase in thickness $t$. Polaritons with relatively higher wavevectors (shorter penetration depth) in the wavevector region of a thinner material attenuates in thicker material without carrying energy across the baths and their $\mathcal{T}$ gets < 0.1. Consequently, their contribution to energy transport disappears in thicker material, and the wavevector region gets smaller.

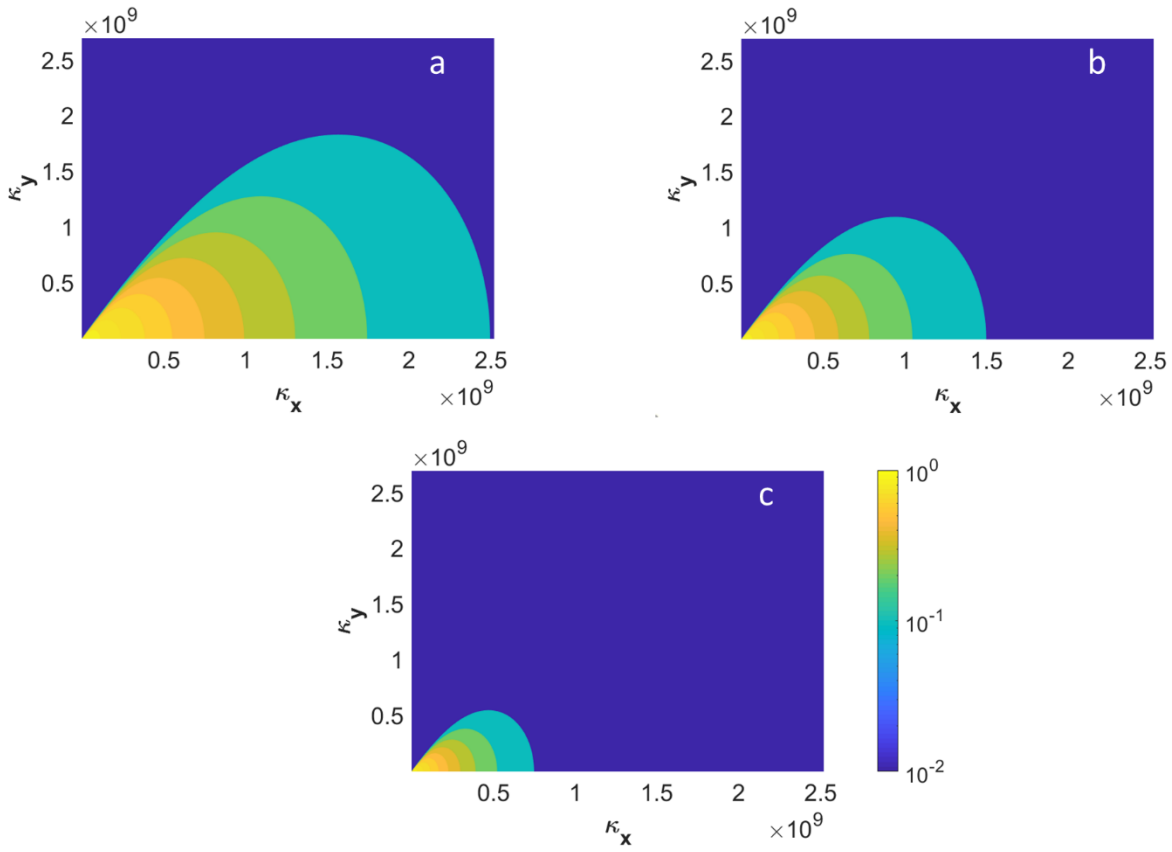


Figure 5.12. Energy exchange function as a function of $k_x$ and $k_y$ between two heat baths on opposite sides of intermediate material with a thickness of a) t = 15 nm, b) t = 25 nm, and c) t = 50 nm.

### 5.2.4 Calculation results for radiative heat flux

To understand contribution of polaritons to heat transfer, we plot spectral radiative heat flux, $q''_{\omega,z}$, for various thicknesses at $\Delta T$ = 1 K for $T_C$ = 300 K in Figure 5.13a. Spectral radiative heat flux in RS bands is about 6 orders greater than that outside RS bands. Compared to ordinary radiation waves outside RS bands, polaritons have access to greatly enhanced number of radiative states in RS bands, enabling energy transport through higher number of channels. Thus, contribution of the polaritons considerably increases spectral radiative heat transfer. We also plot $q''_{\omega,z}$ for various thicknesses and see that $q''_{\omega,z}$ in RS bands decreases with increase in thickness. Polaritons with a given penetration depth transport less energy across thicker material, resulting in smaller energy exchange function, $\mathcal{T}$, and $q''_{\omega,z}$ decreases for thicker materials. In addition, we observe 3 separate peaks in $q''_{\omega,z}$. Frequency of these peaks correspond to frequency regions where material loss, imaginary dielectric component, is minimal over the region.

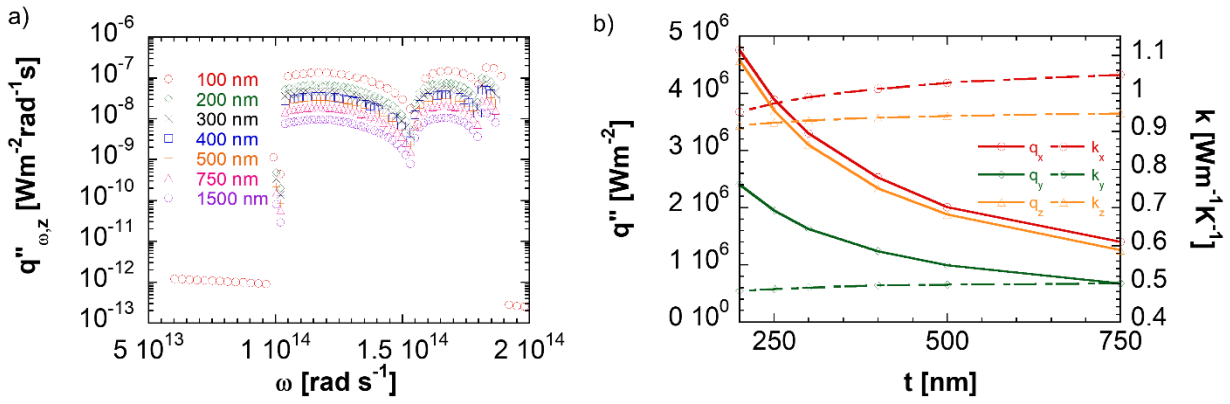


Figure 5.13. a) Spectral radiative heat transfer in RS bands for $q''_{\omega,z}$. b) Thickness-dependent heat flux and thermal conductivity for all three axes. In Figure 3a and 3b, ΔT = 1K and $T_C$ = 300 K. Radiative contribution to energy transport by modes outside RS bands is negligible. Due to this reason and high computational demand, we omit $q''_{\omega,z}$. outside RS bands for the cases with thicknesses except that of 100 nm in a).

We also analyze total radiative heat flux, and Figure 5.13b shows total heat flux, $q''$, in three axes as a function of thickness. We see that $q''$ decreases with thickness in all three axes. As explained in discussion of thickness-dependence for $q''_{\omega,z}$, the decrease happens due to higher dissipation along thicker material. On the other hand, the rate of change decreases. We realize that the relationship between $q''$ and t can be cast in the form of $q'' = At^{-B}$ for all three axes and interpret that as coefficient A indicates maximum limit of radiative heat flux under the given temperature difference, B represents losses in the given direction. In Figure 5.13b, A (B) is found as 6.69 × $10^8$, 3.778 × $10^8$, and 8.036 × $10^8$ $Wm^{-2}$ (0.9323, 0.9553, and 0.9748) for x-, y-, and z-axis, respectively. The reason of the decrease in the rate is that radiative heat generated by fluctuations in added material increases and supplies the heat dissipated by added material more. Furthermore, our results show that $q''_x \sim q''_z$, and $q''_y$ is about half of them over entire thickness range. Our analysis on spectral radiative heat flux in x- and y-axes (not shown here) reveals that $q''_{\omega,y}$ over RS3 (RS2) band is one order less than $q''_{\omega,z}$ ($q''_{\omega,x}$ and $q''_{\omega,z}$) over the same band, and, hence; $2q''_y \sim q''_x \sim q''_z$.

We calculate an equivalent radiative thermal conductivity, $k_i$, in $i$-axis using Fourier's equation, $q''_i = k_i \Delta T/t$, in Figure 5.13b. $k_y$ and $k_z$ remains relatively constant at a value of ~0.49 and ~0.95 $Wm^{-1}K^{-1}$, respectively, over entire thickness range whereas $k_x$ slightly increases

with thickness and approaches a constant value of 1.05 $Wm^{-1}K^{-1}$ at greater thicknesses (bulk material limit). This relatively constant $k_y$ and $k_z$ values and slightly changing $k_x$ arise from losses represented by coefficient B. In thinner material, temperature profile tends to be nonlinear that violates Fourier's equation relying on diffusive transport; hence, linear temperature growth. In materials with higher loss, linear temperature gradient grows even in thin materials. Therefore, slightly higher optical loss in y and z direction (B values are greater) leads in linear temperature gradient in thinner material. In contrast, linear temperature growth in x-axis happens in thicker material due to less loss (lower B).

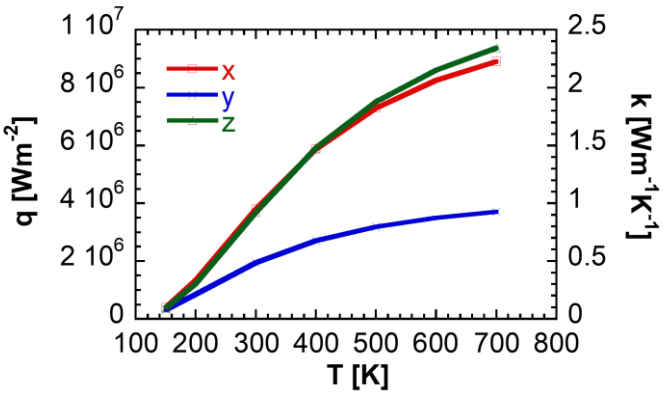


Figure 5.14. Temperature dependent thermal conductivity and radiative heat flux for all three axes.

Thermal conductivity increases with increasing temperature. Figure 5.14 shows temperature dependent radiative heat flux and thermal conductivity for t = 250 nm for all three axes. Both radiative flux and thermal conductivity increase with respect to temperature because increasing thermal energy populates more states in RS bands; therefore, excites more polaritons carrying energy. Inspection of trends in $k$ and $q''$ reveals that the rate of change increases from low temperatures to over 300 K and decreases with higher temperatures. With increase in temperature at lower temperatures, characteristic wavelength around which thermal energy maximizes shifts toward RS bands, and maximum thermal energy excites more hyperbolic polaritons around room temperature. Further increase in temperature results in the characteristic wavelength shifting away from the RS bands to higher energies. Excitation of polaritons minimally increases with higher temperature as a result of mismatch in characteristic wavelength

and RS bands and maximum thermal energy populates ordinary waves more. In addition, at higher temperatures, optical losses increase and lead to further decrease in the rate of change.

## 5.3 Summary

In summary, we studied radiative heat transfer in HM hBN and showed a major contribution to energy transport arising from phonon polaritons supported in Reststrahlen bands. This contribution increases spectral radiative transfer by six orders of magnitude inside Reststrahlen bands compared to that outside Reststrahlen bands. The equivalent radiative thermal conductivity increases with temperature increase, and the radiative thermal conductivity can be of the same order of the phonon thermal conductivity. Experimental measurements support our finding. The measured temperature dependent total thermal conductivity does not follow the usual 1/T phonon conductivity, which is attributed to the increase in radiative thermal conductivity with temperature. We showed the radiative contribution can account for as much as 27% of the total thermal transport at 600 K. Hence, in hBN the radiative thermal transport can be comparable to thermal conduction by phonons.

We also studied radiative heat transfer in HM $MoO_3$. Our analysis revealed that polaritons in RS bands contribute to energy transport in all three principal axes. At room temperature, radiative heat flux in y-axis is half of that in x- and z- axes for a thickness. The reason is that the spectral flux in y-axis over RS3 (RS2) band is one order less than that in z- (x- and z-) axis over the same band. Radiative energy transport decreases with thickness due to higher losses in thicker materials, and we found out that thickness dependence of the heat flux can be expressed in the form: $q'' = At^{-B}$. On the other hand, the equivalent radiative thermal conductivity in all three axes remain relatively still over the thickness range. The radiative thermal conductivity increases with temperature because higher thermal energy excites more polaritons carrying energy. We also pointed out that, compared to the literature results, the equivalent radiative thermal conductivity is in the same order of phonon thermal conductivity around room temperature and even exceeds at higher temperatures.

# 6. SUMMARY AND FUTURE WORK

This dissertation focuses on radiative heat transfer in micro and nanoscales. The studies presented will form a bridge across the knowledge gap between macro and nanoscale radiative heat transfer fields. Contribution of surface phonon polaritons and hyperbolic phonon polaritons to radiative heat transfer between two plates positioned in the near-field was compared using SiC and calcite. Contribution of high-$\kappa$ modes in calcite to near-field radiation is comparable to that of surface polaritons in SiC. The enhancement in calcite is about the same as that in SiC at a large temperature difference of 400 K.

To observe the near-field radiative heat transfer between two $SiO_2$ plates, an experimental technique has been developed and built. The setup enabled measuring temperature change induced by near-field radiation between the plates with a separation range from tens of nanometers to sub-10 nm. Results of the performed experiments agreed well with theoretical model, fluctuation-dissipation theorem. We showed 18000 times enhancement in radiative heat transfer compared to far-field radiation between two $SiO_2$ plates.

The fluctuation-dissipation theorem is not applicable for systems under thermal nonequilibrium. Partitioning the system (many-body model) exposed to temperature gradient extends use of the theory. Analysis conducted with the developed model showed that hyperbolic polaritons in hBN carry energy. The representative thermal conductivity increases with temperature increase and can be of the same order of the phonon thermal conductivity. Conducted experiments of total thermal conductivity agree well with our model. In $MoO_3$, polaritons in RS bands contribute to energy transport in all three principal axes. the equivalent radiative thermal conductivity is in the same order of phonon thermal conductivity around room temperature and even exceeds at higher temperatures.

Many-body approach was extended to account for radiative heat transfer across a vacuum separation. It was shown that two-body model derived for radiative heat transfer arising from surface excitations is a special case of the many-body approach. The many-body approach revealed that hyperbolic phonon polaritons are bulk generated and contribute to energy transport

across the vacuum gap. Driven temperature gradient inside the material saturates the radiative heat transfer and the temperature induced saturation was observed near contact regions where temperature profile inside the materials diverges from uniformity.

Exploration of spectral features of phenomena giving rise to near-field thermal radiation remains short. Research in this path will help better understanding of phenomena; hence, their contribution to radiative heat transfer. In the next section, we explain our effort to build an experimental setup that help exploration of spectral features of resonant near-field phenomena.

## 6.1 Preliminary Results

Analyzing spectral response of a material to incident radiation in infrared (IR) range provides insightful information about molecular structure of the material and help understand fundamentals of phenomena active in the range. Fourier-Transform Infrared (FTIR) spectroscopy is a well-established technique to analyze far-field reflection and transmission spectra of materials over a frequency range from far- to near-infrared with compatible equipment. As discussed in Chapter 1, resonant surface features enhance radiation in the near-field but are evanescent away from the surface. To analyze their spectral properties, in addition to the FTIR technique, use of an advanced technique that extracts near-field information and couple it to the far-field is required. One of these techniques is called Near-field Scanning Optical Microscopy (NSOM). Illuminated by a light at a given frequency, a cantilever tip on Atomic Force Microscope (AFM) confines far-field radiation in form of surface plasmons at apex of the tip and enables probing of near-field enhancement arising from the resonant features by enhancing the back scattered light. Then, the scattered light can be fed into FTIR. Coupling NSOM and FTIR techniques opens up a new path to examine spectral and spatial material response in the near-field. Below, we will explain our effort to couple NSOM and FTIR techniques and utilizes an external light source. Our method is different from the techniques in literature in that external, weak, and mid-IR light source is used to illuminate the tip. We will discuss challenges encountered during implementation of the method along with preliminary experimental results. Then, we will present solutions to overcome the challenges.

To perform near-field spectroscopy, we design a setup consisting of an FTIR system, an AFM system, and an external thermal source. Figure 6.1 shows schematic of the design under development. In what follows, we explain optical equipment used to couple FTIR and NSOM.

Optical system can be divided into two parts: 1- Illumination optics, 2- Collection optics. Orange dashed line in Figure 6.1 denotes pathway of the illuminating light, and green dashed line shows pathway of the collected light backscattered from the tip.

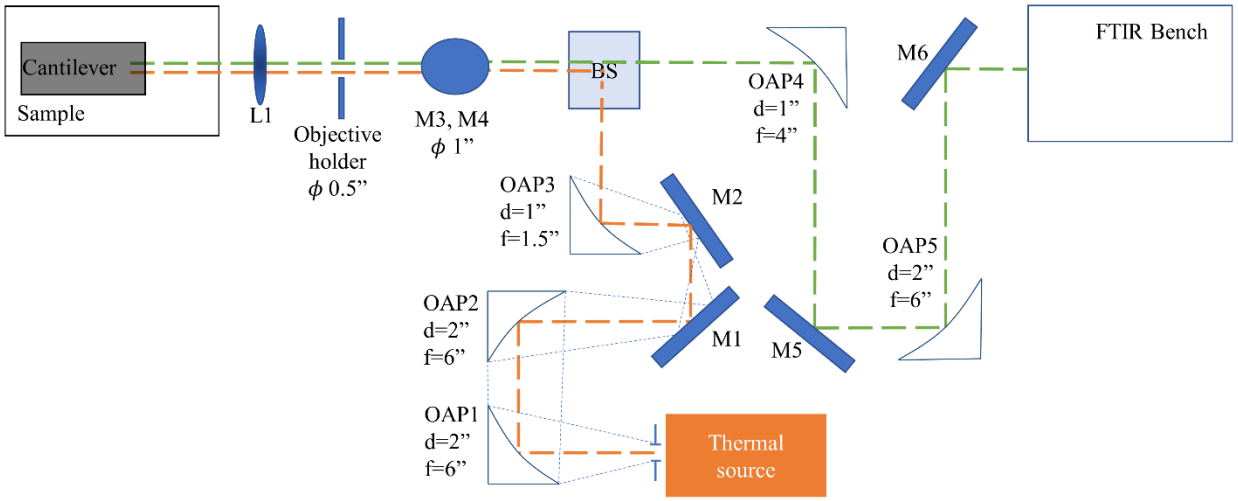


Figure 6.1. Schematic of near-field nanospectroscopy technique using an external thermal source. The system has 5 off-axis parabolic (OAP) mirrors with various diameter (d) and focal lengths (f) to collect, shrink and expand the beam. In addition, as flat mirrors (M) guides the beam, lens (L) focus and collect the light.

Main objective of the illumination optics, shown by orange dashed lines in Figure 6.1, is to collect radiation out of thermal source (housing, emitting ceramic element and elliptical focusing mirror) and to shine the light with the highest intensity on the tip. In terms of collecting, thermal source is highly divergent due to its diffuse emission nature along with finite emitting element. Active size of the ceramic element (Newport, 6575) in the source is 3 × 10 mm. The emitted light is focused to a spot via an elliptical mirror in the source housing. With an aperture at the spot, we can adjust numerical aperture (NA) and output power of irradiation coming out of the housing. To collect the thermal radiation from the housing, an off-axis parabolic mirror (OAP1) is used. Because of two reasons, OAP mirror is preferred over a collimating lens. First, OAP

mirrors are highly reflective over broad frequency range. In contrast, lenses in mid-IR range generally have narrower working spectrum, and lossy transmission. Second, multiple OAP use enables transporting light over long distances without losing significant amount of the light. Over the distance from the housing to the cantilever, we could not achieve focusing the light on the tip using a collecting lens in front of the housing without significant power loss. Shown in Figure 6.1, OAP2 and OAP3 are used to shrink the beam to 1" collimated beam. Here, we can see that NA of OAP2 and OAP3 does not match. The reason is many-fold. First, we would like to carry the light from thermal source to the tip over the shortest distance because divergence is a significant concern in use of thermal sources. Second, limited physical space impacts selection of optics. Third, economical aspects should be considered as well. Based on these considerations, the chosen optics are optimum in terms of carrying the maximum light over the shortest distance in the given physical space. Consequently, OAP3 prepares the beam before striking on beamsplitter (BS), flat mirrors with 1" diameter and objective holder with an aperture size of 0.5''. In theory, the holder blocks ¾ of the light collimated by OAP3. However, the loss is higher because the beam is not perfectly collimated due to finite aperture size, in turn, divergence. The loss at the holder can be minimized with the given system by tuning the position of OAP3. We consider the holder as aperture stop of the illumination optics because it mostly determines the power in the illumination system. The light passing through the holder is focused on the tip using a 1" ZnSe lens with a focal length of 1.5" (LX-1015-Z-ET3.0, Laser Research Optics).

Main objective of the collection optics, shown by green dashed lines in Figure 6.1, is to collect the light backscattered from the tip and to fall it onto detector sensing area in FTIR with maximum intensity. We note that in the collection path, divergence is not a concern because the source here is the tip. Typical size of tips used with weak sources in mid-IR is tens of nanometer and the tip acts as a point source. The backscattered light from the tip traces the illumination pathway up to the beamsplitter. Beamsplitter is potassium bromide (KBr), and its working range spans from 11,000 (~1 μm) to 375 (~26 μm) $cm^{-1}$. The beamsplitter can be considered as another optics that reduces the power. To eliminate the beamsplitter, in another design, the illumination and the collection of the light can be at different paths with different radial angles with respect to the tip. This also provides an advantage of uncoupled illumination and collection optical paths, in turn, additional freedom in optical design. In the design shown here, the backscattered light

passes the beamsplitter and is shrunk by OAP4 to expand the beam size to 2” using OAP5. The purpose of the expansion is to minimize the inevitable loss arising from openings with < Ø 0.5” on one of the mirrors and on another beamsplitter located in FTIR bench.

To test the design given in Figure 6.1, we carry out an experiment after slightly modifying the setup. Between L1 and the tip, we place a flat mirror at focal point of the lens. This does not exactly replace conditions of the tip (i.e. invalid point source assumption); however, it gives good output to analyze the system output. We use the following settings on power meter and OMNIC software: Source powering the thermal source is set to 8V. Aperture on the exit of the housing is fully open. Detector gain is 8, as seen in Figure 6.2. Optical velocity is 1.8988. With the test settings, we are able to observe the centerburst on the interferogram in Figure 6.2 that corresponds to a max generated voltage of 1.57 V at near zero optical path difference in interferogram (Later, this value has been increased to ~1.7 V with further optical alignment). Figure 6.3 shows spectrum of the light falling on sensing area of the detector. This output is weak for an actual experiment because intensity of the backscattered light from the tip will be a couple order less. Therefore, this signal needs to be improved.

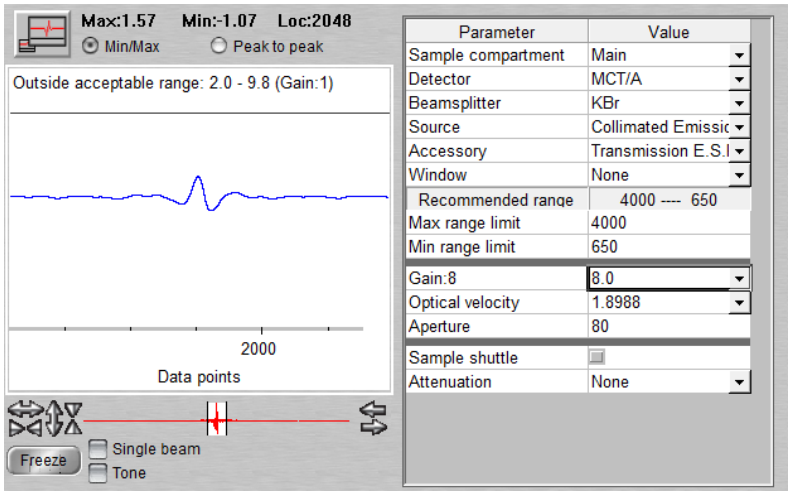


Figure 6.2. Interferogram of the test. The interferogram is taken from OMNIC software. The test is performed based on the settings seen on the right.

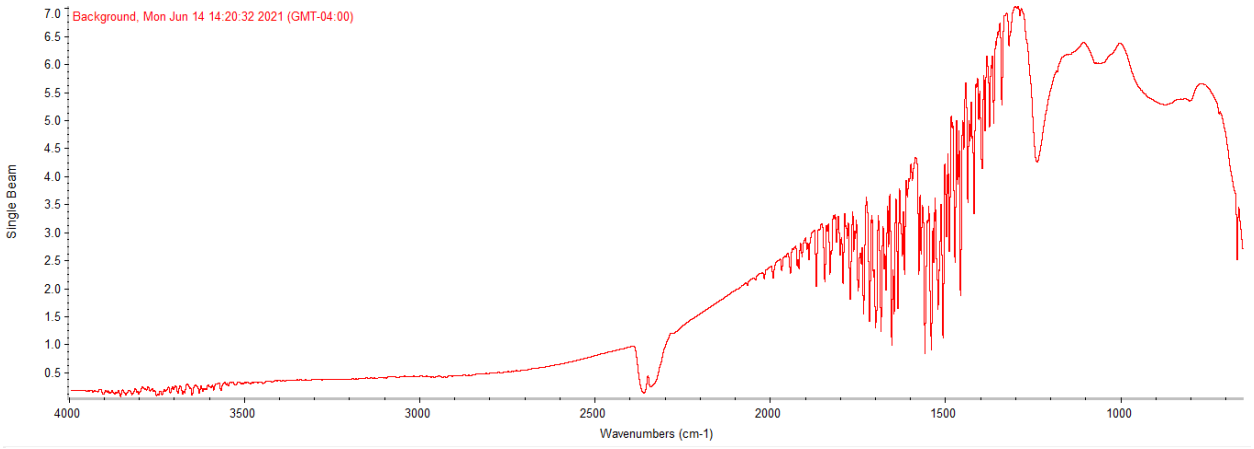


Figure 6.3. Spectrum of the test data.

To improve the signal, we use a chopper and a lock-in amplifier. The chopper is positioned between M5 and OAP5, and its frequency is set to ~1 kHz that is used as a reference frequency for the lock-in amplifier. The signal from the detector is fed to the lock-in amplifier. Then, the amplifier improves the signal at the reference frequency by filtering the signal outside the reference frequency band and outputs the improved signal to FTIR software for recording interferogram. The chopping frequency coincides with modulation frequency of a wavelength in Michelson interferometer, and continuous scan yields spectral response dominated at the chopping frequency. To overcome, step-scan feature of FTIR bench is used. Figure 6.4 shows interferogram obtained using step-scan feature. To acquire the interferogram, the following settings are selected: TC of the lock-in = 500 μs, lock-in gain = 2, average timing = 1 ms, ZPD=512, resolution=32 $cm^{-1}$, mirror velocity = 0.94 cm/s. Figure 6.5 shows spectrum of the chopped radiation. Comparison of Figure 6.3 and 6.5 reveals that we indeed improve the signal using the lock-in amplifier. To draw this conclusion, we check the maximum obtained signal in the spectra, and see that the maximum signal increases from 7 to 10 arbitrary unit with the given settings. Gain of the lock-in amplifier can be to thousands. However, while adjusting the gain, we should pay attention to the voltage input range of FTIR bench (the voltage of the signal from the lock-in to FTIR bench). This indicates a signal with a magnitude few orders less than the measured signal with the current setup can be extracted using the lock-in technique.

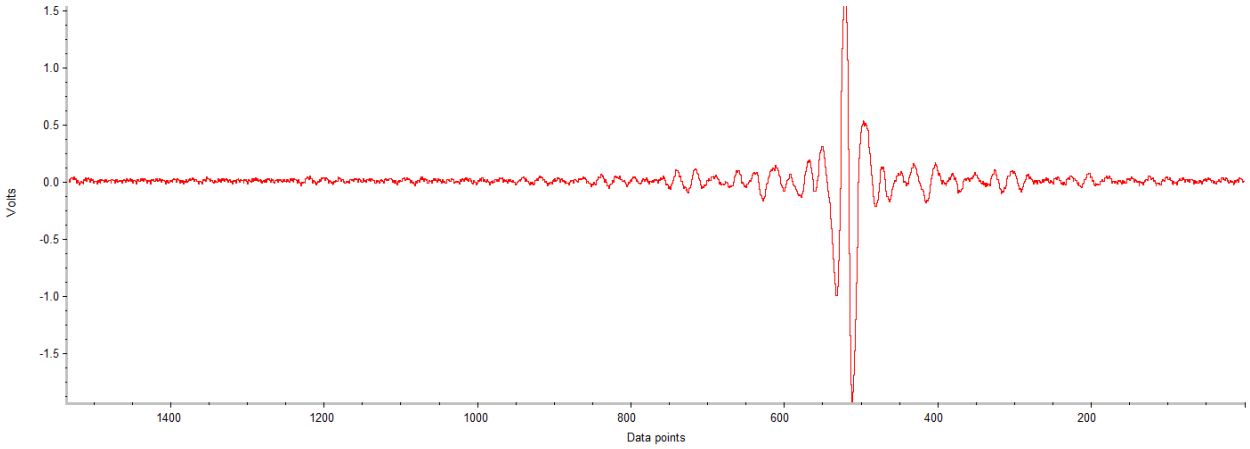


Figure 6.4. Interferogram acquired with step-scan feature.

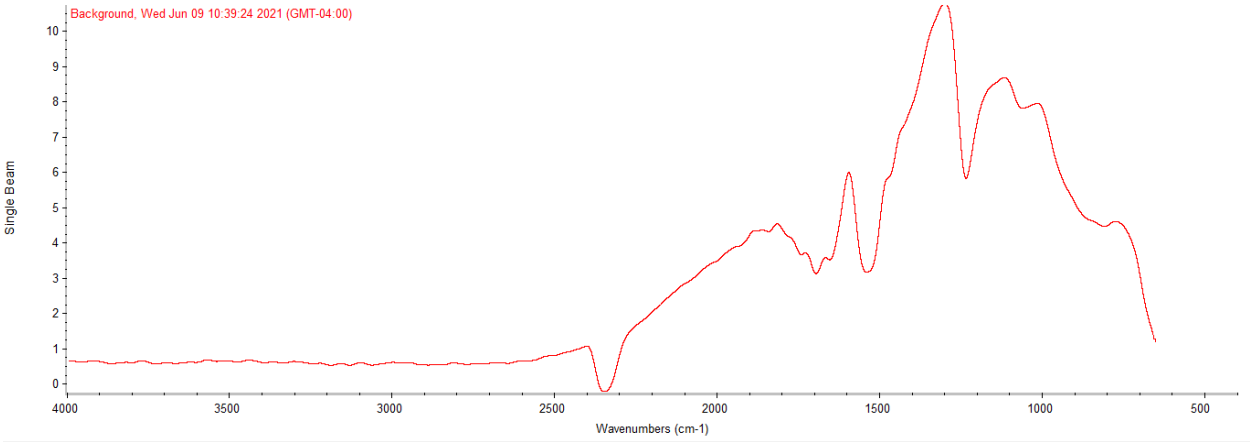


Figure 6.5. Spectrum of the chopped radiation.

## 6.2 Future Work

Based on studies covered in this thesis, there are several directions for future work. First, validation of fluctuation-dissipation theorem for two parallel plates still lacks for separation gaps below the gaps measured in our study. Second, the experimental near-field radiation study can be extended for hyperbolic materials such as hexagonal boron nitride. Third, the many-body model derived using macroscopic dielectric properties may be derived using microscopic properties. Forth, energy transport by polaritons in material is still in infancy, and better understanding its role may provide us more freedom to engineer devices with better thermal performance in small scale.

# REFERENCES


[1] A. Fiorino *et al.*, "A thermal diode based on nanoscale thermal radiation," *ACS Nano,* vol. 12, pp. 5774–5779, 2018.

[2] A. C. Jones and M. B. Raschke, "Thermal Infrared Near-Field Spectroscopy," *Nano Lett.*, vol. 12, pp. 1475–1481, 2012.

[3] Z. Shi *et al.*, "Amplitude-and Phase-Resolved Nanospectral Imaging of Phonon Polaritons in Hexagonal Boron Nitride," *ACS Photonics*, vol. 2, pp. 790–796, 2015.

[4] J. A. Schuller, T. Taubner, and M. L. Brongersma, "Optical antenna thermal emitters," *Nat. Photonics,* vol. 3, pp. 658–661, 2009.

[5] A. Fiorino, L. Zhu, D. Thompson, R. Mittapally, P. Reddy, and E. Meyhofer, "Nanogap near-field thermophotovoltaics," *Nat. Nanotechnol.*, vol. 13, pp. 806–811, 2018.

[6] K. Joulain, J.-P. Mulet, F. Marquier, R. Carminati, and J.-J. Greffet, "Surface electromagnetic waves thermally excited: Radiative heat transfer, coherence properties and Casimir forces revisited in the near field," *Surf. Sci. Rep.*, vol. 57, pp. 59–112, 2005.

[7] S. M. Rytov, Y. A. Kravtsov, and V. I. Tatarskii, *Principles of Statistical Radiophysics 3*. 1987.

[8] S. M. Rytov, *Theory of Electric Fluctuations and Thermal Radiation*. Air Force Cambridge Research, 1959.

[9] M. Modest, *Radiative heat transfer*, 3rd ed. Academic Press, 2013.

[10] J. H. Taylor, C. S. Rupert, and J. Strong, "An Incandescent Tungsten Source for Infrared Spectroscopy," *J. Opt. Soc. Am.*, vol. 41, no. 9, p. 626, Sep. 1951.

[11] A. C. Jones, B. T. O'Callahan, H. U. Yang, and M. B. Raschke, "The thermal near-field: Coherence, spectroscopy, heat-transfer, and optical forces," *Prog. Surf. Sci.*, vol. 88, no. 4, pp. 349–392, Dec. 2013.

[12] Y. Guo and Z. Jacob, "Fluctuational electrodynamics of hyperbolic metamaterials," *J. Appl. Phys.*, vol. 115, no. 10, p. 234306, 2014.

[13] K. Joulain, R. M. Carminati, J.-P. Mulet, and J.-J. Greffet, "Definition and measurement of the local density of electromagnetic states close to an interface," *Phys. Rev. B*, vol. 68, p. 245405, 2003.

[14] C. T. Tai, *Dyadic Green's Functions in Electromagnetic Theory*, 2nd ed. Oxford

University Press, 1996.

[15] J. E. Sipe, “New Green-function formalism for surface optics,” *J. Opt. Soc. Am. B*, vol. 4, no. 4, p. 481, 1987.

[16] R. Kubo, “The fluctuation-dissipation theorem,” *Reports Prog. Phys.*, vol. 29, pp. 255–284, 1966.

[17] S. M. Rytov, Y. A. Kravtsov, and V. I. Tatarskii, *Principals of statistical Radiophysics 3*. SpringerVerlag Berlin Heidelberg New York, 1987.

[18] G. S. Agarwal, “Quantum electrodynamics in the presence of dielectrics and conductors. I. Electromagnetic-field response functions and black-body fluctuations in finite geometries,” *Phys. Rev. A*, vol. 11, no. 1, p. 230, 1975.

[19] C. Henkel, K. Joulain, J.-P. Mulet, and J.-J. Greffet, “Radiation forces on small particles in thermal near fields,” *J. Opt. A Pure Appl. Opt*, vol. 4, pp. 109–114, 2002.

[20] P. Yeh, *Optical waves in layered media*, 2nd ed. Wiley-Interscience, 2005.

[21] C. M. Hargreaves, “Anomalous radiative transfer between closely-spaced bodies,” *Phys. Lett.*, vol. 30A, no. 9, p. 491, 1969.

[22] A. Kittel, W. Müller-Hirsch, J. Parisi, S.-A. Biehs, D. Reddig, and M. Holthaus, “Near-Field Heat Transfer in a Scanning Thermal Microscope,” *Phys. Rev. Lett.*, vol. 95, p. 224301, 2005.

[23] L. Hu, A. Narayanaswamy, X. Chen, and G. Chen, “Near-field thermal radiation between two closely spaced glass plates exceeding Planck’s blackbody radiation law,” *Appl. Phys. Lett.*, vol. 92, p. 133106, 2008.

[24] T. Kralik, P. Hanzelka, V. Musilova, A. Srnka, and M. Zobac, “Cryogenic apparatus for study of near-field heat transfer,” *Rev. Sci. Instrum.*, vol. 82, no. 5, pp. 1–6, 2011.

[25] R. St-Gelais, B. Guha, L. Zhu, S. Fan, and M. Lipson, “Demonstration of Strong Near-Field Radiative Heat Transfer between Integrated Nanostructures,” *Nano Lett.*, vol. 14, pp. 6971–6975, 2014.

[26] R. St-Gelais, L. Zhu, S. Fan, and M. Lipson, “Near-field radiative heat transfer between parallel structures in the deep subwavelength regime,” *Nat. Nanotechnol.*, vol. 11, pp. 515–519, 2016.

[27] A. Fiorino, D. Thompson, L. Zhu, B. Song, P. Reddy, and E. Meyhofer, “Giant enhancement in radiative heat transfer in sub-30 nm gaps of plane parallel surfaces,” *Nano*

*Lett.*, vol. 18, no. 6, pp. 3711–3715, 2018.

[28] D. Polder and M. Van Hove, "Theory of radiative heat transfer between closely spaced bodies," *Phys. Rev. B*, vol. 4, no. 10, p. 3303, 1971.

[29] J. Pendry, "Radiative exchange of heat between nanostructures," *J. Phys. Condens. Matter*, vol. 11, pp. 6621–6633, 1999.

[30] J.-P. Mulet, K. Joulain, R. Carminati, and J.-J. Greffet, "Enhanced radiative heat transfer at nanometric distances," *Microscale Thermophys. Eng.*, vol. 6, no. 3, pp. 209–222, Jul. 2002.

[31] S.-A. Biehs, E. Rousseau, and J.-J. Greffet, "Mesoscopic Description of Radiative Heat Transfer at the Nanoscale," *Phys. Rev. Lett.*, vol. 105, no. 23, p. 234301, Dec. 2010.

[32] Y. Guo and Z. Jacob, "Thermal hyperbolic metamaterials," *Opt. Express*, vol. 21, no. 12, pp. 15014–15019, 2013.

[33] H. Salihoglu, "Near-field radiative heat transfer between two parallel plates," Purdue University, 2015.

[34] J. Le Gall, M. Olivier, and J.-J. Greffet, "Experimental and theoretical study of reflection and coherent thermal emission by a SiC grating supporting a surface-phonon polariton," *Phys. Rev. B*, vol. 55, no. 15, p. 10105, 1997.

[35] R. Hillenbrand, T. Taubner, and F. Keilmann, "Phonon-enhanced light–matter interaction at the nanometre scale," *Nature*, vol. 418, pp. 159–161, 2002.

[36] J. D. Caldwell *et al.*, "Low-loss, infrared and terahertz nanophotonics using surface phonon polaritons," *Nanophotonics*, vol. 4, no. 1, pp. 44–68, Jan. 2015.

[37] M. Francoeur, M. P. Menguc, and R. Vaillon, "Spectral tuning of near-field radiative heat flux between two thin silicon carbide films," *J. Phys. D. Appl. Phys.*, vol. 43, 2010.

[38] S. Shen, A. Narayanaswamy, and G. Chen, "Surface phonon polaritons mediated energy transfer between nanoscale gaps," *Nano Lett.*, vol. 9, no. 8, pp. 2909–2913, 2009.

[39] J.-J. Greffet, R. Carminati, K. Joulain, J.-P. Mulet, S. Mainguy, and Y. Chen, "Coherent emission of light by thermal sources," *Nature*, vol. 416, no. 6876, pp. 61–64, Mar. 2002.

[40] S. Jahani and Z. Jacob, "All-dielectric metamaterials," *Nat. Nanotechnol.*, vol. 11, p. 23, 2016.

[41] E. D. Palik, *Handbook of optical constants of solids*. Academic Press, 1998.

[42] F. Marquier, K. Joulain, J.-P. Mulet, R. Carminati, J.-J. Greffet, and Y. Chen, "Coherent

spontaneous emission of light by thermal sources," *Phys. Rev. B*, vol. 69, no. 155412, 2004.

[43] J. Shi, B. Liu, P. Li, L. Y. Ng, and S. Shen, "Near-Field Energy Extraction with Hyperbolic Metamaterials," *Nano Lett.*, vol. 15, no. 2, pp. 1217–1221, 2015.

[44] R. Messina, P. Ben-Abdallah, B. Guizal, M. Antezza, and S.-A. Biehs, "Hyperbolic waveguide for long-distance transport of near-field heat flux," *Phys. Rev. B*, vol. 94, 2016.

[45] S.-A. Biehs, M. Tschikin, R. Messina, and P. Ben-Abdallah, "Super-Planckian near-field thermal emission with phonon-polaritonic hyperbolic metamaterials," *Appl. Phys. Lett.*, vol. 102, no. 13, p. 131106, Apr. 2013.

[46] S. Lang, M. Tschikin, S. Biehs, A. Yu Petrov, and M. Eich, "Large penetration depth of near-field heat flux in hyperbolic media," *Appl. Phys. Lett.*, vol. 104, no. 10, pp. 131106–213102, 2014.

[47] S.-A. Biehs and P. Ben-Abdallah, "Near-Field Heat Transfer between Multilayer Hyperbolic Metamaterials," *Zeitschrift für Naturforsch. A*, vol. 72, no. 2, pp. 115–127, Jan. 2017.

[48] X. L. Liu, R. Z. Zhang, and Z. M. Zhang, "Near-field thermal radiation between hyperbolic metamaterials: Graphite and carbon nanotubes," *Appl. Phys. Lett.*, vol. 1031, no. 10, 2013.

[49] X. L. Liu and Y. Xuan, "Super-Planckian thermal radiation enabled by hyperbolic surface phonon polaritons," *Sci China Tech Sci*, vol. 59, no. 11, pp. 1680–1686, 2016.

[50] P. Shekhar, J. Atkinson, and Z. Jacob, "Hyperbolic metamaterials: fundamentals and applications," *Nano Converg.*, vol. 1, 2014.

[51] D. Lu, J. J. Kan, E. E. Fullerton, and Z. Liu, "Enhancing spontaneous emission rates of molecules using nanopatterned multilayer hyperbolic metamaterials Contents," *Nat. Nanotechnol.*, vol. 9, pp. 48–53, 2014.

[52] D. Korobkin, B. N. Iii, C. Fietz, N. Jegenyes, G. Ferro, and G. Shvets, "Measurements of the negative refractive index of sub-diffraction waves propagating in an indefinite permittivity medium," *Opt. Express*, vol. 18, no. 22, p. 22734, 2010.

[53] T. Galfsky, H. N. S. Krishnamoorthy, W. Newman, E. E. Narimanov, Z. Jacob, and V. M. Menon, "Active hyperbolic metamaterials: enhanced spontaneous emission and light extraction," *Optica*, vol. 2, no. 1, pp. 62–65, 2015.

[54] Z. Liu, H. Lee, Y. Xiong, C. Sun, and X. Zhang, “Far-Field Optical Hyperlens Magnifying Sub-Diffraction-Limited Objects,” *Science (80-. ).*, vol. 315, no. 5819, p. 1686, 2007.

[55] C. L. Cortes, W. Newman, S. Molesky, and Z. Jacob, “Quantum nanophotonics using hyperbolic metamaterials Related content Roadmap on optical metamaterials,” *J. Opt.*, vol. 14, p. 063001, 2012.

[56] E. E. Narimanov and A. V. Kildishev, “Naturally hyperbolic,” *Nat. Photonics*, vol. 9, no. 4, pp. 214–216, Apr. 2015.

[57] G. Zhu *et al.*, “Evolution from Classical to Non-classical Aggregation-Based Crystal Growth of Calcite by Organic Additive Control,” *Langmuir*, vol. 32, no. 35, pp. 8999–9004, Sep. 2016.

[58] S. Riccardo Frisenda *et al.*, “Recent progress in the assembly of nanodevices and van der Waals heterostructures by deterministic placement of 2D materials,” *Chem. Soc. Rev*, vol. 47, p. 53, 2018.

[59] S. Fan, Q. An Vu, M. Dao Tran, S. Adhikari, and Y. Hee Lee, “Transfer assembly for two-dimensional van der Waals heterostructures,” 2020.

[60] S. Dai *et al.*, “Subdiffractional focusing and guiding of polaritonic rays in a natural hyperbolic material,” *Nat. Commun.*, vol. 6, p. 6963, Apr. 2015.

[61] P. Li *et al.*, “Hyperbolic phonon-polaritons in boron nitride for near-field optical imaging and focusing,” *Nat. Commun.*, vol. 6, p. 7507, Jun. 2015.

[62] G. Pettis, “Hertzian dipoles and microstrip circuits on arbitrarily oriented biaxially anisotropic media.”

[63] G. Álvarez-Pérez, K. V. Voronin, V. S. Volkov, P. Alonso-González, and A. Y. Nikitin, “Analytical approximations for the dispersion of electromagnetic modes in slabs of biaxial crystals,” *Phys. Rev. B*, vol. 100, no. 23, pp. 1–11, 2019.

[64] P. G. Cottis and G. D. Kondylis, “Properties of the Dyadic Green’s Function for an Unbounded Anisotropic Medium,” *IEEE Trans. Antennas Propag.*, vol. 43, no. 2, 1995.

[65] D. W. Thompson, M. J. DeVries, T. E. Tiwald, and J. A. Woollam, “Determination of optical anisotropy in calcite from ultraviolet to mid-infrared by generalized ellipsometry,” *Thin Solid Films*, vol. 313–314, pp. 341–346, Feb. 1998.

[66] T. SaItmrai and T. Sato, “Temperature Dependence of Vibrational Spectra in Calcite by Means of Emissivity Measurement,” *Phys. Rev. B*, vol. 4, no. 10, pp. 583–591, 1971.

[67] G. Álvarez-Pérez *et al.*, “Infrared Permittivity of the Biaxial van der Waals Semiconductor α-MoO3 from Near- and Far-Field Correlative Studies,” *Adv. Mater.*, vol. 32, no. 29, 2020.

[68] G. S. Agarwal, “Quantum electrodynamics in the presence of dielectrics and conductors. II. Theory of dispersion forces,” *Phys. Rev. A*, vol. 11, no. 1, pp. 243–252, 1975.

[69] G. S. Agarwal, “Quantum electrodynamics in the presence of dielectrics and conductors. III. Relations among one-photon transition probabilities in stationary and nonstationary fields, density of states, the field-correlation functions, and surface-dependent response func,” *Phys. Rev. A*, vol. 11, no. 1, pp. 253–264, 1975.

[70] G. S. Agarwal, “Quantum electrodynamics in the presence of dielectrics and conductors. IV. General theory for spontaneous emission in finite geometries,” *Phys. Rev. A*, vol. 12, no. 4, pp. 1475–1497, 1975.

[71] G. S. Agarwal, “Quantum electrodynamics in the presence of dielectrics and conductors. V. The extinction and moment theorems for correlation functions and relativistic aspects of blackbody fluctuations,” *Phys. Rev. A*, vol. 12, no. 5, pp. 1974–1986, 1975.

[72] G. S. Agarwal, “Quantum electrodynamics in the presence of dielectrics and conductors. VI. Theory of Lippmann fringes,” 1975.

[73] W. Eckhardt, “First And Second Fluctuation-Dissipation-Theorem In Electromagnetic Fluctuation Theory,” 1982.

[74] A. I. Volokitin and B. N. J. Persson, “Radiative heat transfer between nanostructures,” *Phys. Rev. B*, vol. 63, 2000.

[75] C. Henkel, K. Joulain, R. Carminati, and J.-J. Greffet, “Spatial coherence of thermal near fields,” *Opt. Commun.*, vol. 186, pp. 57–67, 2000.

[76] M. Francoeur, M. P. Mengüç, and R. Vaillon, “Near-field radiative heat transfer enhancement via surface phonon polaritons coupling in thin films,” *Appl. Phys. Lett.*, vol. 93, p. 43109, 2008.

[77] S.-A. Biehs, D. Reddig, and M. Holthaus, “Thermal radiation and near-field energy density of thin metallic films,” *Eur. Phys. J. B*, vol. 55, pp. 237–251, 2007.

[78] M. Francoeur, M. P. Mengüç, and R. Vaillon, “Local density of electromagnetic states within a nanometric gap formed between two thin films supporting surface phonon polaritons,” *J. Appl. Phys.*, vol. 107, 2010.

[79] P.-O. Chapuis, S. Volz, C. Henkel, K. Joulain, and J.-J. Greffet, “Effects of spatial dispersion in near-field radiative heat transfer between two parallel metallic surfaces,” *Phys. Rev. B*, vol. 77, p. 035431, 2008.

[80] M. Francoeur, M. Pinar Mengüc, and R. Vaillon, “Solution of near-field thermal radiation in one-dimensional layered media using dyadic Green’s functions and the scattering matrix method,” *J. Quant. Spectrosc. Radiat. Transf.*, vol. 110, pp. 2002–2018, 2009.

[81] A. I. Volokitin and B. N. J. Persson, “Resonant photon tunneling enhancement of the radiative heat transfer,” *Phys. Rev. B*, vol. 69, p. 045417, 2004.

[82] K. Joulain, “Near-field heat transfer: A radiative interpretation of thermal conduction,” *J. Quant. Spectrosc. Radiat. Transf.*, vol. 109, pp. 294–304, 2008.

[83] C. Henkel and K. Joulain, “Electromagnetic field correlations near a surface with a nonlocal optical response,” *Appl. Phys. B*, vol. 84, pp. 61–68, 2006.

[84] V. Chiloyan, J. Garg, K. Esfarjani, and G. Chen, “Transition from near-field thermal radiation to phonon heat conduction at sub-nanometre gaps,” *Nat. Commun.*, vol. 6, p. 6755, 2015.

[85] A. Alkurdi, C. Adessi, S. Li, K. Termentzidis, and S. Merabia, “Thermal transport across nanometre gaps: phonon transmission vs air conduction,” 2019.

[86] J. Pendry, K. Sasihithlu, and R. V Craster, “Phonon-assisted heat transfer between vacuum-separated surfaces,” *Phys. Rev. B*, vol. 94, p. 75414, 2016.

[87] K. Sasihithlu, J. Pendry, and R. V Craster, “Van der Waals Force Assisted Heat Transfer,” *Zeitschrift fur Naturforsch. - Sect. A J. Phys. Sci.*, 2017.

[88] E. Rousseau, M. Laroche, and J.-J. Greffet, “Asymptotic expressions describing radiative heat transfer between polar materials from the far-field regime to the nanoscale regime,” *J. Appl. Phys.*, vol. 111, no. 1, p. 014311, Jan. 2012.

[89] G. A. Domoto, R. F. Boehm, and C. L. Tien, “Experimental Investigation of Radiative Transfer Between Metallic Surfaces at Cryogenic Temperatures,” *J. Heat Transfer*, vol. 92, no. 3, pp. 412–416, 1970.

[90] E. Rousseau *et al.*, “Radiative heat transfer at the nanoscale,” *Nat. Photonics*, vol. 3, pp. 514–517, Sep. 2009.

[91] R. S. Ottens *et al.*, “Near-field radiative heat transfer between macroscopic planar surfaces,” *Phys. Rev. Lett.*, vol. 107, p. 014301, 2011.

[92] K. Ito, A. Miura, H. Iizuka, and H. Toshiyoshi, “Parallel-plate submicron gap formed by micromachined low-density pillars for near-field radiative heat transfer,” *Appl. Phys. Lett*, vol. 106, p. 83504, 2015.

[93] M. P. Bernardi, D. Milovich, and M. Francoeur, “Radiative heat transfer exceeding the blackbody limit between macroscale planar surfaces separated by a nanosize vacuum gap,” *Nat. Commun.*, vol. 7, p. 12900, Sep. 2016.

[94] J. I. Watjen, B. Zhao, and Z. M. Zhang, “Near-field radiative heat transfer between doped-Si parallel plates separated by a spacing down to 200 nm,” *Appl. Phys. Lett.*, vol. 109, p. 203112, 2016.

[95] B. Song, D. Thompson, A. Fiorino, Y. Ganjeh, P. Reddy, and E. Meyhofer, “Radiative heat conductances between dielectric and metallic parallel plates with nanoscale gaps,” *Nat. Nanotechnol.*, vol. 11, pp. 509–514, 2016.

[96] K. Kloppstech *et al.*, “Giant heat transfer in the crossover regime between conduction and radiation,” *Nat. Commun.*, vol. 8, Feb. 2017.

[97] L. Cui *et al.*, “Study of radiative heat transfer in Ångström- and nanometre-sized gaps,” *Nat. Commun.*, vol. 8, p. 14479, 2017.

[98] S. Sadat, E. Meyhofer, and P. Reddy, “High resolution resistive thermometry for micro/nanoscale measurements,” *Rev. Sci. Instrum.*, vol. 83, p. 84902, 2012.

[99] S. Sadat *et al.*, “Room temperature picowatt-resolution calorimetry,” *Appl. Phys. Lett.*, vol. 99, no. 4, pp. 2011–2014, 2011.

[100] M. C. Wingert, Z. C. Y. Chen, S. Kwon, J. Xiang, and R. Chen, “Ultra-sensitive thermal conductance measurement of one-dimensional nanostructures enhanced by differential bridge,” *Rev. Sci. Instrum.*, vol. 83, no. 2, 2012.

[101] S. M. V. Uppuluri, E. C. Kinzel, Y. Li, and X. Xu, “Parallel optical nanolithography using nanoscale bowtie aperture array,” *Opt. Express*, vol. 18, no. 7, p. 7369, 2010.

[102] E. E. Moon, P. N. Everett, M. W. Meinhold, M. K. Mondol, and H. I. Smith, “Novel mask-wafer gap measurement scheme with nanometer-level detectivity,” *J. Vac. Sci. Technol. B Microelectron. Nanom. Struct.*, vol. 17, no. 6, p. 2698, 1999.

[103] X. Wen, L. M. Traverso, P. Srisungsitthisunti, X. Xu, and E. E. Moon, “High precision dynamic alignment and gap control for optical near-field nanolithography,” *J. Vac. Sci. Technol. B, Nanotechnol. Microelectron. Mater. Process. Meas. Phenom.*, vol. 31, no. 4, p.

041601, 2013.

[104] P. Srisungsitthisunti, E. E. Moon, C. Tansarawiput, H. Zhang, M. Qi, and X. Xu, "Nanometer-level alignment using interferometric-spatial-phase-imaging (ISPI) during silicon nanowire growth," *Instrumentation, Metrol. Stand. Nanomanufacturing IV*, vol. 7767, p. 776707, 2010.

[105] E. E. Moon, L. Chen, P. N. Everett, M. K. Mondol, and H. I. Smith, "Interferometric-spatial-phase imaging for six-axis mask control," *Meas. Phenom.*, vol. 21, p. 2607, 2003.

[106] X. Wen, A. Datta, L. M. Traverso, L. Pan, X. Xu, and E. E. Moon, "High throughput optical lithography by scanning a massive array of bowtie aperture antennas at near-field," *Sci. Rep.*, vol. 5, p. 16192, 2015.

[107] L. Shi *et al.*, "Measuring Thermal and Thermoelectric Properties of One-Dimensional Nanostructures Using a Microfabricated Device," *J. Heat Transfer*, vol. 125, no. 5, p. 881, 2003.

[108] H. W. Ott, *Noise reduction techniques in electronic systems*, 2nd ed. 1988.

[109] M. C. Wingert, Z. C. Y. Chen, S. Kwon, J. Xiang, and R. Chen, "Ultra-sensitive thermal conductance measurement of one-dimensional nanostructures enhanced by differential bridge," *Rev. Sci. Instrum.*, vol. 83, p. 24901, 2012.

[110] Y. Ganjeh *et al.*, "A platform to parallelize planar surfaces and control their spatial separation with nanometer resolution," *Rev. Sci. Instrum*, vol. 83, p. 105101, 2012.

[111] K. Park, S. Basu, W. P. King, and Z. M. Zhang, "Performance analysis of near-field thermophotovoltaic devices considering absorption distribution," *J. Quant. Spectrosc. Radiat. Transf.*, vol. 109, no. 2, pp. 305–316, 2008.

[112] Z. Zheng and Y. Xuan, "Theory of near-field radiative heat transfer for stratified magnetic media," *Int. J. Heat Mass Transf.*, vol. 54, no. 5–6, pp. 1101–1110, 2011.

[113] M. Tschikin, S.-A. Biehs, P. Ben-Abdallah, S. Lang, A. Yu Petrov, and M. Eich, "Radiative heat flux predictions in hyperbolic metamaterials," *J. Quant. Spectrosc. Radiat. Transf.*, vol. 158, pp. 17–26, 2015.

[114] H. Salihoglu, V. Iyer, T. Taniguchi, K. Watanabe, P. D. Ye, and X. Xu, "Energy Transport by Radiation in Hyperbolic Material Comparable to Conduction," *Adv. Funct. Mater.*, vol. 30, no. 6, pp. 6–11, 2020.

[115] Y. Ezzahri and K. Joulain, "Vacuum-induced phonon transfer between two solid dielectric

materials: Illustrating the case of Casimir force coupling," *Phys. Rev. B*, vol. 90, p. 115433, 2014.

[116] A. I. Volokitin, "Contribution of the acoustic waves to near-field heat transfer," *J. Phys. Condens. Matter*, vol. 32, p. 215001, 2020.

[117] J. J. Loomis and H. J. Maris, "Theory of heat transfer by evanescent electromagnetic waves," *Phys. Rev. B*, vol. 50, no. 24, p. 18517, 1994.

[118] J. D. Caldwell *et al.*, "Sub-diffractional volume-confined polaritons in the natural hyperbolic material hexagonal boron nitride," *Nat. Commun.*, vol. 5, p. 5221, Oct. 2014.

[119] I. Latella, P. Ben-Abdallah, S.-A. Biehs, M. Antezza, and R. Messina, "Radiative heat transfer and nonequilibrium Casimir-Lifshitz force in many-body systems with planar geometry," *Phys. Rev. B*, vol. 95, p. 205404, 2017.

[120] S.-A. Biehs, S. Lang, A. Y. Petrov, M. Eich, and P. Ben-Abdallah, "Blackbody theory for hyperbolic materials," *Phys. Rev. Lett.*, vol. 115, p. 174301, 2015.

[121] R. Garrelts, A. Marconnet, and X. Xu, "Assessment of Thermal Properties via Nanosecond Thermoreflectance Method," *Nanoscale Microscale Thermophys. Eng.*, vol. 19, no. 4, pp. 245–257, Oct. 2015.

[122] P. Jiang, X. Qian, R. Yang, and L. Lindsay, "Anisotropic thermal transport in bulk hexagonal boron nitride," *Phys. Rev. Mater.*, vol. 2, p. 64005, 2018.

[123] T. G. Pedersen, "Analytic calculation of the optical properties of graphite," *Phys. Rev. B*, vol. 67, p. 113106, 2003.

[124] A. N. Poddubny, P. A. Belov, P. Ginzburg, A. V Zayats, and Y. S. Kivshar, "Microscopic model of Purcell enhancement in hyperbolic metamaterials," *Phys. Rev. B*, vol. 86, p. 035148, 2012.

[125] H. Salihoglu and X. Xu, "Near-field radiative transfer by bulk hyperbolic polaritons across vacuum gap," *Int. J. Heat Mass Transf.*, vol. 170, p. 120984, 2021.

[126] S. Puebla, R. D'Agosta, G. Sanchez-Santolino, R. Frisenda, C. Munuera, and A. Castellanos-Gomez, "In-plane anisotropic optical and mechanical properties of two-dimensional MoO3," *npj 2D Mater. Appl.*, vol. 5, no. 1, pp. 1–7, 2021.

# VITA

**Education**

Bachelor of Science, Mechanical Engineering, Dokuz Eylul University, Izmir, Turkey, 2006-2011

Master of Science, Mechanical Engineering, Purdue University, West Lafayette, IN, USA, 2013-2015

PhD student, Purdue University, West Lafayette, IN, USA, 2015-present.

**Research interest**

- Near-field radiative heat transfer
- Energy transport by thermal radiation in and across materials
- Engineering thermal radiation properties
- Thermal infrared near-field nano spectroscopy

**Technical Skills**

- Relative alignment of plates in micro and nano scale using optics
- Experimental design under vacuum environment
- Resistive thermometry, Wheatstone bridges, differential measurement
- MATLAB, Fortran, Labview, ANSYS, LAMMPS molecular dynamics simulation
- Wire bonding, optical reflection/transmission spectroscopy

# PUBLICATIONS

1. **Salihoglu**, **H.**, Xu, X. Near-field radiative transfer by bulk hyperbolic polaritons across vacuum gap, International Journal of Heat and Mass Transfer 170, 2021

2. **Salihoglu**, **H.**, Nam, W., Traverso, L., Segovia, M., Venuthurumilli, P., Liu, W., Wei, Y., Li, W., Xu, X. Near-Field Thermal Radiation between Two Plates with Sub-10 nm Vacuum Separation, Nano Letters 20, 2020

3. **Salihoglu**, **H.**, Iyer, V., Taniguchi, T., Watanabe, K., Xu, X. Energy Transport by Electromagnetic Waves Comparable to Phonon Conduction in Natural Hyperbolic Material, Advanced Functional Materials 1905830, 2020.

4. **Salihoglu**, **H.**, Xu, X. Near-field radiative heat transfer enhancement using natural hyperbolic material, Journal of Quantitative Spectroscopy and Radiative Transfer 222-223, 2019